Mathematical Methods for Design of Zone Structured Catalysts and Optimization of Inlet Trajectories in Selective Catalytic Reduction (SCR) and Three Way Catalyst (TWC)

Zur Erlangung des akademischen Grades eines

DOKTORS DER NATURWISSENSCHAFTEN

(Dr. rer. nat.)

von der KIT-Fakultät für Chemie und Biowissenschaften

des Karlsruher Institut für Technologie (KIT)

genehmigte

DISSERTATION

von

Sivaram Kannepalli

aus

Visakhapatnam, Indien

Dekan	:	Prof. Dr. Willem M. Klopper
Referent	:	Prof. Dr. Olaf Deutschmann
Korreferent	:	Prof. Dr. Jan-Dierk Grunwaldt
Tag der mündlichen Prüfung	:	17th October 2017

Let noble thoughts come to me from all directions
(Rig veda)

Acknowledgements

This thesis is based on my research work carried out at the Institute for Technical Chemistry and Polymer Chemistry, Karlsruhe Institute of Technology, from 2012 to 2016.

First of all, for his priceless and valuable suggestions during my time at ITCP, as well as for giving me this opportunity to earn PhD in his group, I would like to sincerely thank Professor Dr. Olaf Deutschmann from the bottom of my heart. I would like to thank Professor Dr. Jan-Dierk Grunwaldt for being the co-referee for my thesis.

I would like to express my immense gratitude towards Dr. Steffen Tischer, for being my supervisor throughout this time and providing valuable guidance and for constantly sharing his valuable knowledge. The numerous technical discussions with him helped me in greatly enriching my knowledge in this field.

I would like to thank Dr. Martin Votsmeier, Umicore AG, the industrial partner in the project for his valuable advice and the ideas he gave me during this course helped me in diversifying my knowledge on this subject.

I would also like to thank our project partners Prof. Dr. Herbert Vogel, Prof. Dr. Alfons Drochner, (TU Darmstadt), Prof. Dr. Ulrich Konigorski (RTM, TU Darmstadt), respective students and other members of the project for their valuable suggestions during the project meetings.

The research project was funded by BMBF (ReffKat, grant no. 03X3563B) and I would like to thank BMBF for the financial support. There are many people who have helped me to finish this work in different ways, and who deserve my sincere gratitude.

I would also like to thank all my colleagues at the ITCP, especially Henning Stotz, Dr. Karla Herrera Delgado, Dr. Vikram Menon and Dr. Hüseyin Karadeniz for the numerous discussions which led to solutions for many problems both professionally and personally and for providing a great working environment. I would also like to thank Dr. Mathias Hettel and Frau Ursula Schwald for their support.

Finally, I am infinitely grateful to my parents and my sister who have always supported me in my pursuit of my goals. No words can express my gratitude towards my gurus who showered their infinite blessings on me and finally I would like to thank Pradeep and Sandeep for constantly being by my side, motivating and encouraging me during rough times.

Abstract

Catalytic converters have become the most important automotive emission control devices to reduce the pollutants produced by combustion engines. With the imposition of stringent emission standards, the demand on the activity of these exhaust aftertreatment catalysts has been significantly increased over the years. The focus of this work is to solve optimization problems in the field of automotive exhaust gas catalysts to improve the efficiency, three problems are considered in this work: 1) The delayed light-off after cold start in oxidation catalysts, 2) Efficient ammonia dosing to reduce ammonia excursions in selective catalytic reduction (SCR) system and 3) Voltage stabilization in a three way catalyst (TWC) during fuel cut of scenario. This thesis addresses the first problem by development of a model based mathematical optimization methodology to optimize the precious metal loading profile (PGM loading) in zone-structured catalytic converters. To carry out this task, a multi zone-structured optimization formulation, where the catalyst is divided into zones axially to obtain a non uniform optimal PGM loading profile, which can be tested experimentally, is used. The effects of the PGM loading on washcoat diffusion limitations is also considered. The objective is to optimize the spatial distribution of loading for a fixed amount of precious metal to maximize the chemical conversion efficiency under transient operation. To achieve this, a transient 1D+1D model is solved with the help of implicit solver DASPKADJOINT and translated in to a non-linear optimization problem that can be solved with any derivative based nonlinear programming (NLP) solvers. The model is applied to two example cases: CO oxidation on a Pt/Al_2O_3 based Diesel Oxidation Catalyst (minimizing cold-start emissions) and CH_4 oxidation on Pd/Al_2O_3 (minimizing deactivation effects). In both the cases it was observed that the optimal solution with maximum PGM loading in the channel entrance region improved the performance of the catalysts. The methodology presented is generic and can be transferred to different systems with different chemistries, which may result in significantly different optimization results and loading patterns.

The ability to catalytically reduce NO_x efficiently with ammonia has made the SCR technology indispensable in diesel after-treatment systems. Ammonia is dosed periodically in the form of urea which decomposes to ammonia and reacts with NO_x. During the application of real world driving cycles, owing to fast transients of the emissions, it is not efficient to dose constant amount of ammonia. An efficient optimized dosing strategy is quite essential to improve the

efficiency and contain the NH_3 excursions within the permissible limits. Development of such an optimized dosing solution requires the usage of simple yet powerful mathematical models capable of simulating the process with reasonable accuracy and robust optimization schemes, which can ensure optimal solutions in spite of having high number of parameters to be optimized. Several efficient model reduction techniques presented in the literature have been used to obtain a grey-box model which can effectively simulate the process. Direct collocation method based on Orthogonal Collocation over Finite Elements (OCFE) is used to transform the DAE-constrained optimization problem into a nonlinear program. The developed model is applied to the World Harmonic Transient Driving cycle to optimize NH_3 dosing for each second of the driving cycle. The obtained optimal dosing solution not only improved the efficiency of the process but also maintained the NH_3 excursions below 10 ppm over the entire driving cycle. The developed methodology is applicable to other systems to obtain such large scale optimal solutions efficiently.

In the third problem, the optimization scheme used in the second problem is extended to obtain an optimal inlet lambda trajectory solution to quickly stabilize the downstream sensor voltage to avoid rich excursions. Firstly, an observer model is developed with simple kinetics which is validated against test bench measurements. Direct collocation method based on Orthogonal Collocation over Finite Elements (OCFE) is used to transform the DAE-constrained optimization problem into a nonlinear program. The nonlinear problem is solved to obtain the optimal solution which quickly stabilized the downstream sensor voltage without overshoot. This strategy significantly reduces the recovery time of the downstream oxygen sensor. The reduction in recovery time is important for the operation of a feedback TWC controller.

Zusammenfassung

Abgaskatalysatoren zählen zu den wichtigsten Maßnahmen, um Schadstoffemissionen von Verbrennungsmotoren zu vermindern. Mit der stetigen Verschärfung der Emissionsstandards nahm über die Jahre der Forschungsbedarf zu Abgasnachbehandlungssystemen signifikant zu. Der Fokus dieser Arbeit liegt auf der Lösung von Optimierungsproblemen im Bereich der Autoabgaskatalyse, um die Effizienz zu steigern. Dabei werden drei Problemklassen behandelt: 1) Die Light-Off-Verzögerung beim Kaltstart in Oxidationskatalysatoren, 2) Die effiziente Ammoniakdosierung bei der selektiven katalytischen Reduktion (SCR), um Ammoniakdurchbrüche zu vermeiden, 3) Die Spannungsstabilisierung der Lambda-Sonde im Drei-Wege-Katalysator (TWC) während einer Schubabschaltung.

Das erste Problem wird durch eine modellbasierte mathematische Optimierung beschrieben, bei der das Beladungsprofil von gezont-strukturierten Katalysatoren auf Basis von Platingruppen-Metallen (PGM) optimiert wird. Dazu wird ein Optimierungsproblem aufgestellt, bei dem ein katalytisch aktiver Kanal in Zonen aufgeteilt wird, die mit unterschiedlichen Mengen von PGM beladen werden. Eine solche Beladung kann auch experimentell getestet werden. Die Effekte der Beladung auf Diffusionslimitierungen im Washcoat werden ebenso berücksichtigt. Ziel ist es, die axiale Verteilung der Beladung zu optimieren, wobei die Gesamtmenge an PGM konstant gehalten wird, um den Gesamtumsatz unter transienten Bedingungen zu maximieren. Dabei wird ein transientes 1D+1D-Modell mit dem impliziten Differentialgleichungslöser DASPKADJOINT numerisch gelöst und in ein nichtlineares Optimierungsproblem übersetzt, das mit einem beliebigen ableitungsbasierten nichtlinearen Optimierungslöser (NLP) behandelt werden kann. Dieses Modell wird auf zwei Beispielfälle angewandt: die CO-Oxidation auf einem Pt/Al_2O_3 Dieseloxidationskatalysator (DOC), um die Kaltstart-Emissionen zu minimieren, sowie die CH_4-Oxidation auf Pd/Al_2O_3 unter Minimierung der Deaktivierungseffekte. In beiden Fällen wird beobachtet, dass bei der optimalen Lösung ein Beladungsmaximum am Kanaleingang zu einer Umsatzsteigerung führt. Die präsentierte Methode ist darüber hinaus allgemeingültig und kann auf andere Systeme mit unterschiedlicher Chemie angewandt werden, so dass auch signifikant andere Lösungen generiert werden können.

Die Fähigkeit, NO_x effizient durch Ammoniak zu reduzieren, ist Grundlage der SCR-Technologie für die Dieselabgasnachbehandlung. Ammoniak wird diskontinuierlich durch

Zersetzung von Harnstoff-Wasser-Lösung dem SCR-Katalysator zugeführt. Bei der Anwendung im Fahrbetrieb ist es wegen hochgradig transienter Wechsel der Emissionen nicht sinnvoll, konstante Menge Ammoniak zu dosieren. Eine effiziente optimale Dosierungsstrategie ist wichtig, um einerseits hohen Umsatz zu gewährleisten und andererseits NH_3-Schlupf zu vermeiden. Die Entwicklung einer optimalen Dosierungsstrategie erfordert die Anwendung einfacher, aber hinreichend akkurater mathematischer Modelle und robuster Optimierungsalgorithmen, um eine Lösung für eine große Anzahl zu optimierender Parameter zu erhalten. Mehrere Modellreduktionstechniken aus der Literatur wurden verwendet, um ein Grey-Box-Modell zu konstruieren. Die Methode der orthogonalen Kollokation über finiten Elementen (OCFE) wird genutzt, um die differential-algebraischen Gleichungen aus dem Optimierungsproblem in ein nichtlineares Programm zu überführen. Das Modell wird auf eine Simulation des WHTC-Testzyklus angewandt, um die NH_3-Dosierung für jede Sekunde des Zyklus zu optimieren. Die optimale Lösung verbessert die Effizienz des Reduktion unter Einhaltung eines Schlupf-Maximums von 10 ppm zu jedem Zeitpunkt. Die präsentierte Methode lässt sich auch auf ähnliche Probleme zur Optimierung transienter Eingangsbedingungen anwenden.

Im dritten Beispiel wird dieselbe Optimierungsmethode erweitert, um eine optimale Lambda-Trajektorie zu berechnen, die das Lambdasensorsignal am Katalysatorausgang stabilisiert, um Durchbrüche fetter Abgasgemische zu vermeiden. Zunächst wurde ein Beobachtermodell mit vereinfachter Kinetik entwickelt und gegen Versuchsstand-Experimente kalibriert. Direkte Kollokation auf Basis der OCFE wird genutzt, um das Optimierungsproblem in ein nichtlineares Programm zu überführen. Die optimale Lösung zeigt eine schnelle Stabilisierung der Ausgangssensor-Spannung ohne Überschwingungen. Diese Strategie verringert die Relaxationszeit der Sensorspannung signifikant, was wichtig für den Einsatz als Feedback-Controller in einem Dreiwegekatalysator wäre.

Nomenclature

a	Activity, [-]
a_s	Steady state activity, [-]
$\mathrm{Area}_{\mathrm{geo}}$	Geometric surface area, [m^2]
$\mathrm{Area}_{\mathrm{cat}}$	Catalytic surface area, [m^2]
$A_{i\mathrm{f}}$	Forward kinetic pre-exponential, [mol/m^3 s]
$A_{i\mathrm{b}}$	Backward kinetic pre-exponential, [mol/m^3 s]
c_p	Specific heat capacity of the mixture, [J/kg K]
c_{s}	Specific heat capacity of the solid phase, [J/kg K]
d_{h}	Hydraulic diameter, [m]
D	Dispersion, [-]
D_{ch}	Channel diameter, [m]
$D_{\mathrm{eff},i}$	Effective diffusivity coefficient, [m^2/s]
$D_{i,\mathrm{N_2}}$	Binary diffusivity coefficient, [m^2/s]
$D_{\mathrm{knud},i}$	Knudsen diffusivity coefficient, [m^2/s]
d_{p}	Particle diameter, [m]
E_{ads}	Activation energy,[J/mol]
E_{deac}	Deactivation Activation energy,[J/mol]
E_{oxi}	Activation energy,[J/mol]
$E_{i\mathrm{f}}$	Forward activation energy,[J/mol]
$E_{i\mathrm{b}}$	Backward activation energy,[J/mol]
$F_{\mathrm{cat/geo}}$	Catalytic activity factor, [-]
ΔG_i	Gibbs free energy, [J/mol]
ΔH_i	Enthalpy change of the reaction, [J/mol]
h	Heat transfer coefficient, [W/m^2 K]
H_{j}	Molar enthalpy of a species, [J/mol]
k_i^{f}	Forward kinetic pre-exponential, [mol/m^2 s]
k_i^{b}	Backward kinetic pre-exponential, [mol/m^2 s]
K_i	Equilibrium constant, [-]
k_{ads}	Adsorption pre-exponential, [-]
k_{deac}	Deactivation pre-exponential, [-]

$\boldsymbol{k}_{\mathbf{me}}$	Vector of external mass transfer coefficient of species, [m/s]
$\boldsymbol{k}_{\mathbf{mi}}$	Vector of internal mass transfer coefficient of species, [m/s]
$\boldsymbol{k}_{\mathbf{mo}}$	Vector of overall mass transfer coefficient of species, [m/s]
k_{oxi}	Kinetic pre-exponential, [mol/m^2 s]
$\boldsymbol{l}$	Lagrange polynomial, [-]
L	Channel length, [m]
L_{PGM}	Precious metal loading, [g/ft^3]
L_{w}	Washcoat loading, [g/ft^3]
m_{cat}	Mass of PGM, [g]
M_{cat}	Molecular weight of the precious metal, [g/mol]
n_{c}	Number of collocation points, [-]
n_{e}	Number of finite elements, [-]
Nu	Nusselt number ,[-]
P	Pressure, [Pa]
$\boldsymbol{P}$	Control parameters
$\mathrm{PGM}_{\mathrm{total}}$	Total PGM loading, [g/ft^3]
$\boldsymbol{PP}$	Vector of dimensionless constants, [-]
R	Reaction rates, [mol/m^2 s]
ΔS_i	Entropy change of the reaction, [J/mol]
$\boldsymbol{S}$	Vector of the rate of production of the species, [mol/m^2 s]
S_{cat}	Specific catalytic surface area, [m^{-1}]
Sh	Sherwood number ,[-]
Sh_{int}	Internal Sherwood number, [-]
$Sh_{\mathrm{int},\infty}$	Asymptotic Sherwood number, [-]
$\boldsymbol{SS}$	Vector of dimensionless constants, [-]
T_{f}	Gas phase temperature, [K]
$T_{\mathrm{f},0}$	Inlet gas phase temperature, [K]
T_{ref}	Reference temperature, [K]
T_{s}	Solid phase temperature, [K]
u	Velocity, [m/s]
$\boldsymbol{u}$	Time dependent control parameters, [-]
X	Conversion, [-]

$\boldsymbol{X_f}$	Vector of species mole fraction in gas phase, [-]
$\boldsymbol{X_s}$	Vector of species mole fraction in solid phase, [-]
$X_{\mathrm{NO_x}}$	$\mathrm{NO_x}$ Conversion, [-]
$\boldsymbol{y}$	Vector of algebraic variables, [-]
$\boldsymbol{z}$	Vector of state variables, [-]
$\boldsymbol{\beta}$	Vector of independent variables, [-]
δ_{w}	Washcoat thickness, [m]
ε_{g}	Volume fraction of the channel, [-]
$\varepsilon_{\mathrm{wc}}$	Washcoat porosity, [-]
θ_{NH_3}	Surface coverage of adsorbed ammonia,[-]
$\theta_{\mathrm{Ce_3O_3}}$	Relative surface loading of $\mathrm{Ce_3O_3}$, [-]
λ	Solid heat conductivity, [W/m K]
λ	Air to fuel ratio, [-]
Λ	Geometric constant, [-]
ρ_{g}	Gas mixture density, [kg/m^3]
ρ_{s}	Solid density, [kg/m^3]
ρ_{wc}	Washcoat density, [kg/m^3]
Γ_{cat}	Surface site density, [mol/m^2]
τ	Tortuosity factor, [-]
τ	Normalized time, [-]
$\Omega_{\mathrm{NH_3}}$	Adsorption capacity of ammonia, [mol/m^3]

Contents

1. Introduction

The global efforts to combat motor vehicle emissions date back to the mid-1960s, when vehicular emissions were identified as a major source of the precursor pollutants (NOx and VOCs) of photochemical smog in Los Angeles, California, USA. The first emission controls prevented crankcase emissions from escaping from the car [1]. In the early 1970s, CO and HC standards were set, followed by standards to control NOx. More and more countries followed the U.S.A. in establishing their own emission standards and regulations to control motor vehicle emissions in the 1970s and 1980s. These led to more regulations in most of the industrial and developing countries with varying degree of stringency from country to country. Ever since, these emission control technologies for motor vehicles have experienced dramatic improvements to meet the stringent requirements. The common emission control technologies include catalytic converters and particulate filters. As these developments spread and the adverse effects of motor vehicle pollution were recognized, worldwide demand for emission control systems increased [1, 2].

With the advent of Hybrid electric vehicles (HEVs), plug-in hybrid electric vehicles (PHEVs), and all-electric vehicles (EVs) which can be generalized as zero tailpipe emission vehicles, the burden on internal combustion engine vehicles to keep up with stringent ever increasing emission standards. EVs produce zero direct emissions. PHEVs produce zero tailpipe emissions when they are in all-electric mode, but they can produce evaporative emissions. And when using the internal combustion engine, PHEVs also produce tailpipe emissions. However, their direct emissions are typically lower than those of comparable conventional internal combustion vehicles [3].

1.1. Internal Combustion Engines

Internal combustion engines are most commonly used for propulsion in automobiles, equipment, and other portable machinery. In mobile scenarios, internal combustion is advantageous, since it can provide high power-to-weight ratios together with excellent fuel energy-density. These engines are used in almost all automobiles, motorcycles, boats, and in a wide variety of aircraft and locomotives. They are also used as electricity generators for household and commercial applications.

In a typical IC engine the fuel, which is commonly made up of hydrocarbons derived from petroleum, combusts with air and emits mainly harmless and nontoxic CO_2, H_2O and N_2. Typical fuels used can be diesel, gasoline, and petroleum gas, and propane gas in some cases. Most of the internal combustion engines designed for gasoline can also run on natural gas or liquefied petroleum gases without major modifications except for the fuel delivery components. Liquid and gaseous bio-fuels, such as ethanol and biodiesel, a form of diesel fuel that is produced from crops is also used. Some can also run on hydrogen gas.

Besides the tremendous dependability on non-renewable energy sources (fossil fuels), another drawback which is a major concern is the excursion of toxic byproducts like CO, H_2, C_xH_y (hydrocarbons), NO_x, SO_x and particulate matter (like soot) due to incomplete combustion of the fuels. These emissions contribute to deterioration of the environment, which has been a topic of major discussion in the present times. Automobile emissions have become a major source of urban pollution leading to global warming and health risks. CO is highly toxic and can affect blood's ability to carry oxygen. NO_x is a precursor to smog and acid rain. It is a mixture of NO and NO_2. Prolonged exposure to NO_2 can result in respiratory problems. Particulate matter poses serious threat to health and can penetrate deep into the lungs.

Internal combustion engines can be broadly divided in to two types 1) Spark ignition gasoline engines and 2) compression ignition diesel engines depending on the fuel and the method used to achieve ignition in the cylinders to create combustion. The after-treatment systems used for each of these engines depend on their respective exhaust compositions emitted from them and the legislations imposed on them [4–6]. The Environmental Protection Agency (EPA) in the United States and the European Emissions Standards in European Union established regulations to curb the emissions. Standards were established based on the engine, i.e., gasoline or diesel, and on the weight of the vehicle, i.e., passenger car, light-duty vehicle or heavy-duty vehicle. The different engines used and their exhaust control technologies along with the desired emission levels are described in **Sections 1.3 and 1.4.**

1.2. Catalytic converters and Particulate filters

Generally the two main components of exhaust aftertreatment systems used for gasoline or diesel engines are catalytic converters and particulate filters. The former and the latter differ in the flow pattern. A typical converter design, illustrated in **Figure 1.1**, consists of monoliths coated with catalytic material. These monoliths have a number of parallel channels to facilitate

the gas flow in the axial direction, and are made up of either ceramic or metal substrates. The substrates provide a high geometric surface area for gas contact. This substrate is coated with highly porous inorganic oxides such as γ-Al_2O_3, SiO_2 or ZrO_2 that can retain the noble metal. Noble metals such as Pt, Pd, Rh etc., are then deposited on the washcoat. Exhaust gas flowing through the catalytic converter diffuses to the catalyst surface where heterogeneous reaction takes place.

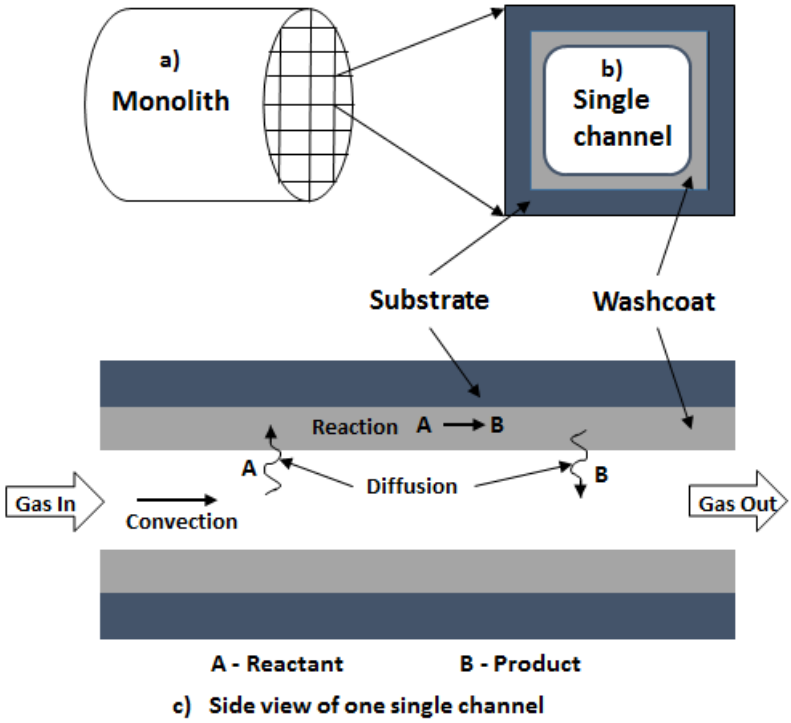

Figure 1.1. Illustration of a) Catalytic converter monolith, b) One single channel and c) Side view of one single channel.

The porous wall particulate filters consist of a honeycomb of long channels similar to catalytic converters. However in the particulate filters, only alternate channels of the honeycomb are open, so that all of the flow entering the device will pass through a porous wall, as illustrated in **Figure 1.2**. The pores in the wall capture the soot by interception. During operation the soot builds up on the porous wall and clogs the wall increasing the flow resistance and pressure drop. Necessitating a regeneration event to remove the clogged soot and reduce the pressure drop.

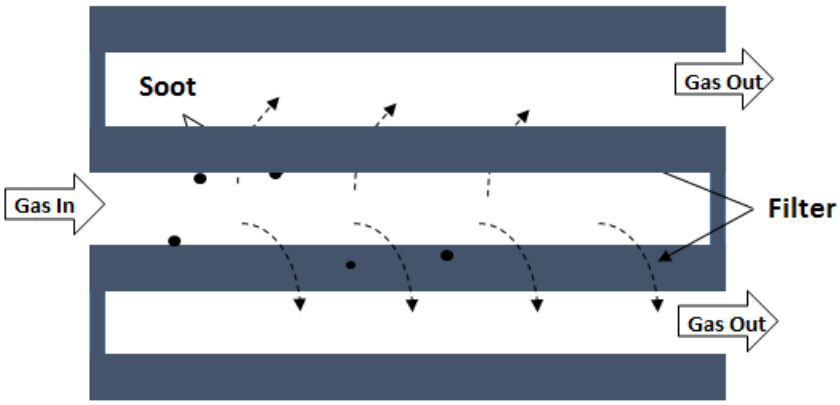

Figure 1.2. Illustration of Side view of a particulate filter.

1.3. Diesel: Emissions and Aftertreatment systems

In a diesel engine, only air is inducted into the engine and then compressed. Diesel engines then spray the fuel into the hot compressed air at a suitable, measured rate, causing it to ignite. The main pollutants produced in a diesel setup are NOx and particulate matter (PM). Varied levels of HC and CO are also produced depending on the different modes of combustion operation. **Table 1.1** shows the most important regulations as introduced by the European Union from the first Euro 1 legislation in 1992 to the latest Euro 6 legislation in 2014 for diesel powered passenger cars [7].

To treat these toxic pollutants and to meet the emission legislations for each of these pollutants, a complicated aftertreatment system is adopted for diesel vehicles. The aftertreatment system is typically a combination of different catalysts like DOC (Diesel oxidation catalyst), DPF (Diesel particulate filter), SCR (Selective catalytic reduction) or LNT (lean NO_x trap) and ASC (Ammonia slip catalyst) (if SCR is used). The main pollutants resulting from a diesel engine and the components use to control them are presented below.

Table 1.1. EU emission standards for diesel passenger cars.

	Year	CO	HC	HC+NOx	NOx	PM	PN
		g/km					*/km
Euro 1	1992	2.72	-	0.97	-	0.14	-
Euro 2	1996	1	-	0.9	-	0.1	-
Euro 3	2000	0.64	-	0.56	0.5	0.05	-
Euro 4	2005	0.5	-	0.3	0.25	0.025	-
Euro 5	2009	0.5	-	0.23	0.18	0.005	6×10^{11}
Euro 6	2014	0.5	-	0.17	0.08	0.005	6×10^{11}

1.3.1. CO, HC and NO oxidation

DOC

The Diesel oxidation catalyst (DOC) has evolved to be an important standard equipment for Diesel vehicles. Its main function is the oxidation of hydrocarbons and CO via reactions (R1.1) and (R1.2) and also NO Oxidation via reaction (R1.3) [8]. With the introduction of particulate filters and NOx aftertreatment (particularly SCR), the role of the Diesel oxidation catalyst become more diverse and indispensable. Its ability to oxidize NO to NO_2 has become vital in efficiently reducing NO_x to N_2. NO oxidation was an undesired side reaction since NO_2 is an unwanted pollutant. However, the SCR catalysts are found to operate more efficiently at an NO/NO_2 ratio of 1. So it has become evident that the DOC plays a very important role in producing the right amount of NO_2 [9]. A high NO_2 content is also beneficial for the continuous soot removal from the particulate trap. For these applications, special DOCs with high NO oxidation performance have been developed.

$$2\,CO + O_2 \rightarrow 2\,CO_2 \qquad \text{(R1.1)}$$

$$C_xH_{2y} + \left(x + \frac{y}{2}\right) O_2 \rightarrow x\,CO_2 + y\,H_2O \qquad \text{(R1.2)}$$

$$2\,NO_x \rightarrow N_2 + x\,O_2 \qquad \text{(R1.3)}$$

1.3.2. NOx reduction

The Diesel vehicles are typically equipped with Exhaust Gas Recirculation (EGR) units to reduce the NO_x emissions. However using an EGR results in increase of PM emissions. So there is a tradeoff between NO_x and PM when using this system. Lean NO_x trap and selective catalytic reduction are the two popular technologies used to catalytically reduce the NO_x to N_2 at low temperatures.

Selective catalytic reduction (SCR)

The selective catalytic reduction (SCR) catalysts are used in diesel exhaust aftertreatment systems to reduce the nitrogen oxides (NO_x) with the aid of ammonia (NH_3) to nitrogen (N_2) and water (H_2O). The reductant is usually stored as AdBlue™, an aqueous solution with 32.5% urea, which is injected into the tailpipe upstream of the SCR catalyst. The water evaporates and the urea ($CO\text{-}(NH_2)_2$) decomposes into isocyanic acid (HNCO) and NH_3 via (R1.4). The HNCO decomposes further by hydrolysis to additional molecules of NH_3 and CO_2 via (R1.5) [10, 11].

$$NH_2 - CO - NH_2 \rightarrow NH_3 + HNCO \quad \text{(R1.4)}$$

$$HNCO + H_2O \rightarrow NH_3 + CO_2 \quad \text{(R1.5)}$$

Ammonia (obtained from urea hydrolysis) reacts with NO and NO_2 in the presence of O_2 in three different reaction pathways, namely Standard SCR (R1.6), Fast SCR (R1.7) and Slow SCR (R1.8) as given below

$$4\,NH_3 + 4\,NO + O_2 \rightarrow 4\,N_2 + 6\,H_2O \quad \text{(R1.6)}$$

$$2\,NH_3 + NO + NO_2 \rightarrow 2\,N_2 + 3\,H_2O \quad \text{(R1.7)}$$

$$4\,NH_3 + 3\,NO_2 \rightarrow 3.5\,N_2 + 6\,H_2O \quad \text{(R1.8)}$$

In addition to these reactions, there are other side reactions: namely NH_3 oxidation to N_2 or N_2O and NO oxidation to NO_2. These side reactions have an influence on the selectivity for N_2 [6, 12–20].

$$2\,NH_3 + 1.5\,O_2 \rightarrow N_2 + 3\,H_2O \quad \text{(R1.9)}$$

$$2\,NH_3 + 2\,O_2 \rightarrow N_2O + 3\,H_2O \quad \text{(R1.10)}$$

$$NO + 0.5\,O_2 \leftrightarrow NO_2 \quad \text{(R1.11)}$$

The vanadium catalyst has insufficient activity at lower temperature and inadequate durability at higher temperatures for mobile applications (>400 ◦C). Both, Cu- and Fe-exchanged ZSM-5 have attracted recent interest given their higher activity and lower cost. Cu-ZSM-5 has the higher of the two low temperature activities [13].

Lean NO_X trap (LNT)

The ability to store nitrogen oxides on barium sites to form nitrates during lean phase and reduce to nitrogen in rich atmosphere made Lean NOx Trap or NOx Storage and Reduction Catalyst (NSR) a promising technology to reduce NOx to N_2 in diesel engines [21–24].

In this system, firstly NO is oxidized to NO_2, which then reacts with the basic oxides to form a nitrate. The conventional LNT catalyst comprises of precious metals (Pt, Rh, etc.) and oxides of alkaline earth metal (Ba, K) supported on Al_2O_3, MgO, etc. The typical reactions during the storage phase are listed from R1.12-R1.15.

$$NO + 0.5\,O_2 \leftrightarrow NO_2 \quad \text{(R1.12)}$$

$$2\,NO_2 + 0.5\,O_2 + BaO \rightarrow Ba(NO_3)_2 \quad \text{(R1.13)}$$

$$3\,NO_2 + BaO \rightarrow Ba(NO_3)_2 + NO \quad \text{(R1.14)}$$

$$Ba(NO_3)_2 \rightarrow BaO + 2\,NO + 1.5\,O_2 \quad \text{(R1.15)}$$

Once the storage capacity of the oxide is saturated the catalyst must be regenerated. For this purpose the engine is switched to rich operation for a few seconds. The precious metal component on the adsorber catalyst promotes the reduction of nitrate by CO, hydrocarbon, or H_2 to form N_2. The typical reactions occurring during the regeneration phase are

$$Ba(NO_3)_2 + 5\ CO \rightarrow BaO + 5\ CO_2 + N_2 \quad \text{(R1.16)}$$

$$Ba(NO_3)_2 + 5\ N_2 \rightarrow BaO + 5\ H_2O + N_2 \quad \text{(R1.17)}$$

In this way, the oxide is recovered and can serve as NOx adsorber during the following cycle of lean operation. The regeneration cycle is triggered by the engine management that monitors the NOx level of the adsorber catalyst either by model-based computation of the total NOx fed into the adsorber during each cycle or by applying a sensor downstream of the adsorber [6].

1.3.3. Particulate matter

The particulate matter emitted from the engine are generally made up of tiny solid and liquid particles. The exhaust from the diesel engines consist of particles of sizes from 0.01–1 mm and consist of carbon-rich particles (soot), hydrocarbons, and sulfates. Within the engine, due to incomplete mixing, zones of air deficiency arise and lead to soot formation. Simultaneously, in zones with excess air, soot is partially burned. Soot emissions are strongly dependent on the air–fuel mixture and are generally high near stoichiometry. [6].

Diesel Particulate Filter (DPF)

The particulate filter described in the **Section 1.2** is the most popular equipment used to control the particulate matters from the diesel engines[25]. The particulate matter collected on the filter will clog the pores and can cause significant pressure drop resulting in efficiency of the engines. In order to avoid this scenario the soot trapped in the pores of the filter can be purged by two ways, namely 1) Active regeneration and 2) passive regeneration. Firstly during active regeneration, the soot trapped can be oxidized by oxygen according to the following reactions R1.18 and R1.19.

$$C(s) + 0.5\ O_2 \rightarrow CO \quad \text{(R1.18)}$$

$$C(s) + O_2 \rightarrow CO_2 \quad \text{(R1.19)}$$

Oxidation of soot by oxygen requires temperatures above 600 °C. Such temperatures are not regularly reached in all applications. For this reason, most vehicles are equipped with a

sophisticated engine control strategy that tracks the soot load over time either by an internal model and/or a pressure drop sensor and triggers the regeneration event. The regeneration event takes about 10 min and has to be executed about every 1000 km in a typical passenger-car application [6, 26].

Another possible way to burn the soot trapped in the filters is by passive regeneration by using NO_2 as oxidizing agent to oxidize the soot [27] according to the following reactions presented in table

$$C(s) + 2\,NO_2 \rightarrow 2NO + CO_2 \qquad (R1.20)$$

$$C(s) + NO_2 \rightarrow 2\,NO + CO_2 \qquad (R1.21)$$

The oxidation of soot by NO_2 takes place continuously and does not require a separate regeneration event. Because of this reason, this form of regeneration is called continuous or passive regeneration. These reactions are active at temperatures as low as 250 – 300 °C. However, in most vehicles the exhaust temperature and/or NO concentration are not sufficient to guaranty a secure passive regeneration under all driving conditions. For this reason, in most vehicles passive regeneration needs to be supplemented by occasional active regeneration. On the other hand, passive regeneration also helps to prolong the interval between regeneration events, even for vehicles that mainly rely on active regeneration [6].

c-DPF

In the catalyzed diesel particulate filter (c-DPF), a catalyst is applied onto the filter media to facilitate chemical reactions between components of the gas phase and the soot (carbon) collected in the filter. A typical illustration of a catalyzed particulate filter is presented in **Figure 1.3.** This catalyst plays a major role in facilitating passive regeneration of the filter by enabling the oxidation of the collected soot at temperatures in the range of in the 300-400 °C. In these filter systems, the catalyst in addition to lowering the soot ignition temperature also accelerates the soot oxidation rate to minimize the fuel economy penalty. Additionally, it also minimizes the high CO emissions that could otherwise occur during active regeneration, when large amounts of soot are burned during a short time period [28, 29].

s-DPF

The integration of particle filtration (diesel particle filter, DPF) and the most efficient deNOx technology (selective catalytic reduction, SCR) into one system is the most efficient solution, up to date, to minimize the emissions of diesel engines. Besides very efficient elimination of solid particles (particle counts filtration efficiency (PCFE) up to 99.99 %) with the filter functionality and a simultaneous substantial reduction of NOx (over 90 %) with the SCR coating are possible [6]. A typical illustration of a s-DPF is presented in **Figure 1.3.** This integrated system moves closer to the engine and the heat-up time of the unified SCR diesel particulate filter (s-DPF) component is additionally shortened proportional to the reduction of the overall thermal inertia.

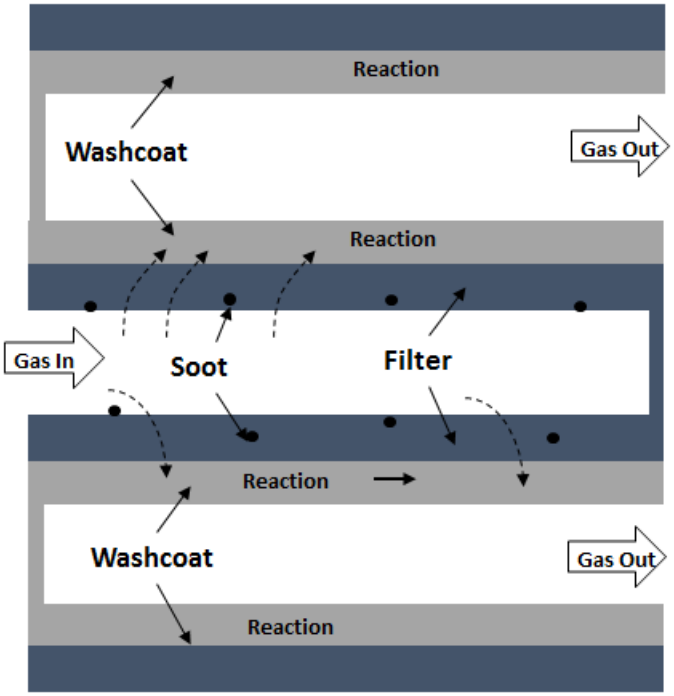

Figure 1.3. Illustration of Side view of a catalyzed particulate filter.

The main reactions occurring in a s-DPF are presented below:

$$C(s) + 0.5\ O_2 \rightarrow CO \qquad (R1.22)$$

$$C(s) + O_2 \rightarrow CO_2 \quad \text{(R1.23)}$$

$$C(s) + NO_2 \rightarrow CO + NO \quad \text{(R1.24)}$$

$$C(s) + 2\,NO_2 \rightarrow CO_2 + 2\,NO \quad \text{(R1.25)}$$

$$NH_3 + S \leftrightarrow NH_3S \quad \text{(R1.26)}$$

$$4\,NH_3S + 4\,NO + O_2 \rightarrow 4\,N_2 + 6\,H_2O + 4\,S \quad \text{(R1.27)}$$

$$2\,NH_3S + NO + NO_2 \rightarrow 2\,N_2 + 3\,H_2O + 2\,S \quad \text{(R1.28)}$$

$$4\,NH_3S + 3\,NO_2 \rightarrow 3.5\,N_2 + 6\,H_2O + 4\,S \quad \text{(R1.29)}$$

$$NO + 0.5\,O_2 \leftrightarrow NO_2 \quad \text{(R1.30)}$$

where the first four reactions describe the reduction of soot (represented in the notation by C(s)) by oxygen and nitrogen dioxide. In s-DPFs, nitrogen dioxide (NO_2), provided by the diesel oxidation catalyst, does no longer exclusively support the favorable fast SCR reaction, but it is also consumed in a competitive way in the passive oxidation of soot.

1.4. Gasoline: Emissions and Aftertreatment systems

In a spark ignition engine, the fuel is mixed with air and then inducted into the cylinder during the intake process. After the piston compresses the fuel-air mixture, the spark ignites it, causing combustion. The spark is provided by a combination of lead acid battery and an induction coil. The expansion of the combustion gases pushes the piston during the power stroke. The spark-ignited gasoline engine works with a stoichiometric gas composition. The main pollutants after the combustion are nitrogen monoxide (NO), carbon monoxide (CO), and unburned hydrocarbons (HC). Table 1.2 shows the most important regulations as introduced by the European Union for gasoline powered passenger cars [7].

Table 1.2. EU emission standards for gasoline cars.

	Year	CO	HC	HC+NOx	NOx	PM	PN
		g/km					*/km
Euro 1	1992	2.72	-	0.97	-	-	-
Euro 2	1996	2.2	-	0.5	-	-	-
Euro 3	2000	2.3	0.2	-	0.15	-	-
Euro 4	2005	1	0.1	-	0.08	-	-
Euro 5	2009	1	0.1	-	0.06	0.005	-
Euro 6	2014	1	0.1	-	0.06	0.005	6×10^{11}

Three way catalyst

Three way catalysts (TWC) are the most popular exhaust gas after-treatment system for gasoline engines. They are an effective pollutant conversion system widely used in current production vehicles to satisfy emissions regulations. In a TWC, carbon monoxide (CO), and unburned hydrocarbons (HC) are oxidized to CO_2 and H_2O and NO_x is reduced to N_2 simultaneously. The typical reactions in a TWC are presented from R31 - R35. TWC are found to be more efficient when the air-to-fuel ratio (A/F ratio) entering the TWC is at stoichiometric conditions. In general the air-to-fuel equivalence ratio (λ) given by (1.1) which is a normalized unit is used often to quantify the composition of the entering fuel.

$$\lambda = \frac{(A/F)_{actual}}{(A/F)_{stoichiometry}} \tag{1.1}$$

However the inlet gases entering the TWC deviates from stoichiometry leading to uncontrolled excursions. In order to pacify these excursions, three-way catalysts contain Ce that tries to maintain the λ value closer to 1. Ce transits between Ce^{III} and Ce^{IV} and acts as an oxygen buffer [30–32]. During lean operation, Ce_2O_3 is oxidized by excess O_2 and NO_x, resulting in the correction of λ towards stoichiometry. In the following rich operation, the stored oxygen in turn is used to oxidize the excess CO and hydrocarbons, again shifting the gas-phase composition towards stoichiometry. Typical modern vehicles with petrol or gas engines include one or more 'close-coupled' catalysts near to the exhaust manifold and often an additional catalyst further down the exhaust, under the floor of the car. The exhaust system will include an oxygen sensor or air: fuel ratio sensor that monitors the oxygen content of the exhaust and

continuously adjusts the fueling to match the conditions. This also ensures that the system alternates rapidly between very slightly fuel-lean and very slightly fuel-rich conditions. In this way both the oxidation functions (conversion of CO and HC to CO_2 and water) and the chemical reduction function (NOx to nitrogen) can operate simultaneously [30, 33, 34].

$$2\,CO + O_2 \rightarrow 2\,CO_2 \qquad \text{(R1.31)}$$

$$C_xH_{2y} + \left(x + \frac{y}{2}\right) O_2 \rightarrow x\,CO_2 + y\,H_2O \qquad \text{(R1.32)}$$

$$2\,NO_x \rightarrow N_2 + x\,O_2 \qquad \text{(R1.33)}$$

$$O_2 + 2\,Ce_2O_3 \leftrightarrow 2\,Ce_2O_4 \qquad \text{(R1.34)}$$

$$CO + Ce_2O_4 \leftrightarrow CO_2 + Ce_2O_3 \qquad \text{(R1.35)}$$

GPF

Even though Gasoline direct injection (GDI) engines help improve fuel economy and reduce CO_2 emissions, they can have higher particulate emissions due to shorter fuel/air mixing times in the cylinder. Additionally the upcoming Euro 6c emissions regulation for spark ignition engines to regulate the particulate emissions will make the Gasoline particulate filters compulsory to meet these challenging targets [35]. Gasoline particulate filters use the same type of wall-flow substrates as diesel particulate filters and can be included in the exhaust system in addition to the series three-way catalyst. However, the particulate emissions from a gasoline engine are roughly 10-30 times lower than that exhaust from a diesel engine. Additionally the three way catalyst coating can be directly applied to the filter substrate to form a four-way catalyst. Also the higher exhaust gas temperatures prevalent in the gasoline systems mean that GPFs should be able to regenerate passively most of the time, which greatly simplifies the task of managing them.

1.5. Outcome and thesis structure

The main outcome of this thesis is the development of mathematical methodologies to solve distinct problems in the field of exhaust aftertreatment systems. The primary outcome of this work is the development and application of various models ranging from the most complex 1D+1D model to relatively simple grey box models to simulate the respective after-treatment models depending on the application. The secondary and the most novel outcome of the work is the usage of these reactor models to obtain optimal solutions to different problems. State-of-the-art optimization schemes and optimization softwares are used with different reactor models and unique optimal results are obtained. The mathematical methodologies developed are not trivial. The thesis is organized as follows: Firstly, chapter 2 gives an overview of the general reactor models (1D+1D & 1D) which are used in the subsequent chapters. Also this chapter presents the different optimization methodologies and optimization problem formulations in detail and also provides details about the DAE (Differential Algebraic Equations) solver and also discusses in detail the different ways to obtain sensitivity information to be provided to the optimization software. Chapter 3 is dedicated to obtain the optimum axial precious metal loading profile to improve the conversion and decrease the cumulative emissions. In this chapter, the 1D+1D model presented in Chapter 2 is used along with the DAE solver and the single shooting method is employed to optimize the system. The methodology is applied to two applications in order to demonstrate the efficiency of the model. In both the cases the optimum solutions showed improvement in performance. In Chapter 4, the problem of obtaining an optimum inlet NH_3 dosing profile which would not only increase the conversion but also limits the NH_3 breakthrough below 10 ppm at any instant of time for a transient driving cycle is presented. Firstly, the 1D+1D model is validated with experimental results taken from the literature. The model is then dimensionally reduced to a 1D model and then to simpler grey-box model, which has less number of equations and computationally less expensive to solve without sacrificing the quality. This reduced model is then used for optimization by employing the technique of Direct collocation which is well suited to obtain optimum inlet trajectory solutions. The grey-box model enables the optimization scheme to obtain the solution over the entire driving cycle. The solution obtained not only increased the overall conversion but also kept the NH_3 breakthrough below 10 ppm at any time instant. Finally chapter 5 deals with the problem of finding an optimal inlet lambda trajectory solution for a three-way catalyst during the fuel cut-off scenario which would stabilize the sensor voltage as quickly as possible without overshooting. In this application an isothermal 1D model is used and again the technique of

Direct collocation is used to obtain the solution. The main difference between the methodology used in this chapter and in the previous chapter is that the model is solved for a smaller time horizon and the model is also framed as DAE model which is flexible and also facilitates usage of reaction schemes with inhibition factors. The solution obtained from the optimization is quick and stable and stabilizes the voltage quickly without any overshoot.

2. Modeling

This chapter presents the governing equations to model the transport of mass, species and energy in channels and catalytic layers of the catalytic converter. Different models can be used to model the channel and the catalytic walls in principle. Here in **Section 2.1,** firstly the general 3D and 2D modeling approaches are briefly presented followed by 1D+1D model used in chapters 3 and 4 and then the 1D model used in chapters 4 & 5. The diffusion model used to evaluate internal diffusion within the pores of the catalytic layer used in chapters 3 & 4 and the PGM loading to washcoat thickness correlation used in chapter 3 are presented in **Sections 2.1.3 & 2.1.4**.

Section 2.2 describes the general concepts about the formulation of optimal control problem for a given DAE problem. Followed by a brief introduction about the NLP (non-linear program) solver used in the present study. **Section 2.1.3** describes in detail the direct methods which include the sequential strategy and simultaneous strategy. The different shooting approaches, like single shooting, multiple shooting and collocation methods and their formulations are also discussed in detail. Followed by a discussion about the implicit DAE solver used and the different approaches for the sensitivity information evaluation are also presented in **Section 2.1.5.**

Dynamic optimization methods presented in this thesis are based on a direct approach. These approximate the infinite dimensional optimal control problem by a finite dimensional NLP that is suited for numerical algorithms. Shooting methods rely on embedded integrators with sensitivity capabilities for obtaining variable profiles and derivative information. The Direct collocation method is based on orthogonal collocation over finite elements with Gauss-Radau interpolation points and Lagrange polynomials. To improve performance of large-scale optimization algorithms, efficient derivative computations are necessary, where automatic differentiation is presented in this section. This technique provides partial derivatives of system equations and constraints with accuracy up to machine precision by applying the chain rule.

2.1. Modeling of Catalytic converter

A typical catalytic converter has a large number of parallel channels in a honeycomb monolith structure with catalyst washcoated walls. To simulate the behavior of the catalytic converter one representative channel is selected. The model accounts for the convective mass transfer

through the channel, the diffusive mass transfer and the chemical reactions within the catalytic layer coupled together via the mass transfer boundary conditions at the wall [36, 37].

The transient species balance equation inside the channel is described in terms of the concentration of the *i*-th species by eq. (2.1) in 3D Cartesian coordinates.

$$\frac{\partial C_i}{\partial t} = -u\frac{\partial C_i}{\partial x} + D_{g,i}\left(\frac{\partial^2 C_i}{\partial z^2} + \frac{\partial^2 C_i}{\partial y^2}\right) \tag{2.1}$$

where $D_{g,i}$ represents the diffusivity of the species in the channel (direction and units).

In case of cylinder geometry, equation (2.1) can be transformed to equation (2.2)

$$\frac{\partial C_i}{\partial t} = -u\frac{\partial C_i}{\partial x} + D_{g,i}\frac{1}{r}\frac{\partial}{\partial r}\left(r\frac{\partial C_i}{\partial r}\right) \tag{2.2}$$

In these models species diffusion in radial direction (r), is considered while axial diffusion is neglected along the channel [36]. The axial molecular diffusion effects are important only at low values of Peclet number signifying the ratio of the convective mass transfer rate to the rate of the diffusive mass transfer, $Pe = \left(u\, D_h / D_g\right)$ but in most of the automotive application it is found to be greater than 50 [38, 39].

2.1.1. 1D + 1D model

In the 1D+1D model, the average value for velocity and concentration over the channel cross-section in the gas phase are considered and the interaction between the gas and the solid phase is ensured via mass transfer coefficients concept [40–42]. Since the flow in a monolith channel for typical automotive applications is generally laminar (Re < 2000), the flow can be assumed dynamically incompressible, allowing the chemical species and energy equations to be solved independently [40]. The effects of boundary layers are lumped into the source term. Assuming uniform velocity in the open channel and neglecting axial diffusion, the bulk gas species equation is given by eq. (2.3)

$$\frac{\partial \boldsymbol{C}_{\mathrm{f}}}{\partial t} = -u\frac{\partial \boldsymbol{C}_{\mathrm{f}}}{\partial z} - \frac{4\boldsymbol{k}_{\mathbf{me}}(\boldsymbol{C}_{\mathrm{s}} - \boldsymbol{C}_{\mathrm{f}})}{D_{\mathrm{h}}} \tag{2.3}$$

where u denotes the average velocity, $\boldsymbol{C}_{\mathrm{f}}$ is the average species concentrations over the cross section of the channel and $\boldsymbol{C}_{\mathrm{s}}$ is the species concentrations in the pores of the washcoat. Transforming eqn (2.3) in to mole fraction yields eqn (2.4) given by

$$\frac{\partial \boldsymbol{X}_{\mathbf{f}}}{\partial t} = -u\frac{\partial \boldsymbol{X}_{\mathbf{f}}}{\partial z} - \frac{4\boldsymbol{k}_{\mathbf{me}}(\boldsymbol{X}_{\mathbf{s}} - \boldsymbol{X}_{\mathbf{f}})}{D_{\mathrm{h}}} \tag{2.4}$$

The term on the left hand side denotes the species accumulation term in the gas phase, where X_{f} is the mole fraction of species in the channel. The first term on the right hand side of equation (2.4) signifies the transport of species in the channel by convection, while the second term is the source term which signifies the interphase mass transfer between the gas and solid phase. u denotes the velocity, A_{geo} signifies the specific geometric area ($\mathrm{m}^2/\mathrm{m}^3$) and $\boldsymbol{k}_{\mathbf{me}}$ is the external mass transfer coefficient.

Similarly the transient thermal balance equation inside the channel is represented in 1D as eq. (2.5).

$$c_p\rho_{\mathrm{g}}\frac{\partial T_{\mathrm{f}}}{\partial t} = -c_p\rho_{\mathrm{g}}u\frac{\partial T_{\mathrm{f}}}{\partial z} - \frac{4h(T_{\mathrm{s}} - T_{\mathrm{f}})}{D_{\mathrm{h}}} \tag{2.5}$$

The term on the left hand side denotes the accumulation while the first and second term on the right hand side denote the heat advection in the channel and the heat convection term between the gas and solid phase respectively.

The physical and chemical processes within the catalytic layer comprise several steps including diffusion and surface reactions. The gaseous species diffuse into the washcoat layer and adsorb strongly on the catalytic surface and react with other surface species followed by desorption.

The diffusion within the catalytic layer is described by the following equation:

$$\varepsilon_{\mathrm{wc}} \frac{\partial \boldsymbol{X_s}}{\partial t} = \boldsymbol{D_{eff}} \frac{\partial^2 \boldsymbol{X_s}}{\partial r^2} + \frac{S_{\mathrm{cat}} \boldsymbol{S}}{c_{\mathrm{T}}} \tag{2.6}$$

where X_s denotes the concentration of the species inside the pores and $\boldsymbol{S}$ shows the formation rate of species i due to the surface reactions. Where $c_{\mathrm{T}} = P/RT_{\mathrm{f,0}}$ is the total concentration. $\varepsilon_{\mathrm{wc}}$ denotes the porosity of the washcoat. Distribution of species is considered perpendicular to the wall and diffusion in the directions parallel to the wall is neglected.

Heat transfer in the wall comprises the conduction along the channel balanced by heat transfer boundary condition at the wall and heat of the reactions within the catalytic layer, eq. (2.7). T_s represents the wall temperature distribution in longitudinal direction of the channel. There is no temperature gradient in normal direction of the wall since the thermal conductivity is sufficiently high and the washcoat layer is very thin.

$$c_s \rho_s \left(1 - \varepsilon_{\mathrm{g}}\right) \frac{\partial T_s}{\partial t} = \lambda \left(1 - \varepsilon_{\mathrm{g}}\right) \frac{\partial^2 T_{\mathrm{s}}}{\partial z^2} - \frac{4h(T_{\mathrm{s}} - T_{\mathrm{f}})}{D_{\mathrm{h}}} - \frac{4\, S_{\mathrm{cat}}}{D_{\mathrm{h}}} \sum_{j=1}^{\text{species}} \int_{r=0}^{\delta} H_j(T_{\mathrm{s}}) \cdot S_j dr \tag{2.7}$$

The term on the left hand side denotes the accumulation while the first and second term on the right hand side denote the heat conduction in the solid and the heat convection term between the gas and solid phase respectively. The third term represents the heat release due to the reactions. ε_{g} denotes the volume fraction of the channel.

The following boundary conditions were assumed

At the inlet at$z = 0$, at every time instance the following boundary conditions were applied.

$$\boldsymbol{X_f}(t, 0) = \boldsymbol{X_{f0}}, \quad T_{\mathrm{f}}(t, 0) = T_{\mathrm{f0}} \tag{2.8}$$

At the gas solid interface i.e., at $r = 0$, the following boundary conditions were applied

$$\boldsymbol{k_{me}}(\boldsymbol{X_s} - \boldsymbol{X_f}) = -\boldsymbol{D_{eff}} \frac{\partial \boldsymbol{X_s}}{\partial r} \tag{2.9}$$

At r = R, Neumann boundary condition is applied

$$\frac{\partial \boldsymbol{X_s}}{\partial r} = 0 \tag{2.10}$$

2.1.2. 1D Model

Beside the 1D + 1D model for simulation of the channel, lumped parameter model (1D model) is a promising tool to analyze and design the automotive catalytic reactors [31, 43], as mentioned in **Section 2.1.1**. The lumped parameter model considers the average value for velocity and concentration over the channel cross-section in the gas phase and a peripheral average of the concentration over the catalytic wall. The gas phase species balance and thermal balance are usually the same equation (2.4 & 2.5) described in **Section 2.1.1**. Meanwhile the species balance equation in the solid phase is given by

$$\varepsilon_{\mathrm{wc}} \frac{\partial \boldsymbol{X_s}}{\partial t} = \frac{\boldsymbol{k_{mo}}(\boldsymbol{X_s} - \boldsymbol{X_f})}{\delta_{\mathrm{wc}}} + \frac{S_{\mathrm{cat}} \boldsymbol{S}}{c_{\mathrm{T}}} \tag{2.11}$$

Where the reaction are considered to take place on the surface of the washcoat and all the washcoat diffusion effects are normally lumped in to the reaction kinetics. Similarly the thermal balance equation for the washcoat is described as follows

$$c_s \rho_s (1 - \varepsilon_{\mathrm{g}}) \frac{\partial T_s}{\partial t} = -\lambda (1 - \varepsilon_{\mathrm{g}}) \frac{\partial^2 T_{\mathrm{g}}}{\partial z^2} - h A_{\mathrm{geo}} (T_{\mathrm{s}} - T_{\mathrm{f}}) + \frac{4\, S_{\mathrm{cat}}}{D_{\mathrm{h}}} \sum_{j=1}^{\text{species}} H_j(T_{\mathrm{s}}) \cdot S_j \tag{2.12}$$

The mass and heat transfer coefficients to be used in both the models are evaluated from the position dependent Sherwood and Nusselt numbers [36, 37, 40] which are expressed empirically as

$$Sh = 3.095 + 8.933 \left(\frac{1000}{\boldsymbol{Gz_m}}\right)^{-0.5386} \exp\left(-\frac{6.7275}{\boldsymbol{Gz_m}}\right) \tag{2.13}$$

$$Nu = 2.977 + 6.854 \left(\frac{1000}{Gz_t}\right)^{-0.5174} \exp\left(-\frac{42.49}{Gz_t}\right) \tag{2.14}$$

$$\boldsymbol{Gz_m} = \frac{D_\mathrm{h} Re \boldsymbol{Sc}}{z} \tag{2.15}$$

$$Gz_t = \frac{D_\mathrm{h} RePr}{z} \tag{2.16}$$

where D_h is the hydraulic diameter, $\boldsymbol{z}$ the axial position, $\boldsymbol{Re}$ the Reynolds number, $\boldsymbol{Pr}$ is the Prandtl number, $\boldsymbol{Gz_m}$ and Gz_t are mass and thermal graetz numbers.

2.1.3. Diffusion model

The effective diffusivity coefficient of the species in the washcoat is calculated from bulk and Knudsen diffusivities using the series pore model [40, 44]. The bulk diffusivity coefficient is calculated based on binary diffusion with respect N_2 according to the Fuller-Schettler-Giddings correlation [45].

$$D_{i,N_2} = \frac{1.013 \cdot 10^{-2}\, T^{1.75} \sqrt{\frac{1}{M_i} + \frac{1}{M_{N_2}}}}{P \left(\sqrt[3]{\vartheta_A} + \sqrt[3]{\vartheta_B}\right)^2} \tag{2.17}$$

Here M_i is the Molecular weight of the species in kg/kmol, ϑ_A is the diffusion volume of the species in cm^3/mol and P is the pressure in N/m^2. Since the potential for the gas molecules to collide frequently with the flow boundaries is high in a washcoat. The Knudsen flow describes such a situation and the diffusivity coefficient of the species is given by

$$D_{\mathrm{knud},i} = \frac{d_\mathrm{p}}{3} \sqrt{\frac{8RT}{\pi M_i}} \tag{2.18}$$

where d_p is the particle diameter in m. The effective diffusion coefficient is evaluated as

$$D_{\mathrm{eff},i} = \frac{\varepsilon_\mathrm{wc}}{\tau} \frac{D_{i,N_2} D_{\mathrm{knud},i}}{\left(D_{i,N_2} + D_{\mathrm{knud},i}\right)} \tag{2.19}$$

2.1.4. Correlation between PGM loading and washcoat thickness

Typically, the exhaust gases coming from the internal combustion engine are passed through the catalytic converter where the gases react with the active catalytic material coated on the surface of the channel walls which help in converting harmful pollutants to non-harmful products. The catalysts used in the process are mainly platinum group metals (PGM, i.e. Pt, Pd, Rh), iron (Fe) and Cu-zeolites depending on the type of application. The precious metals typically amount to less than 2-3 weight-% of the total weight of the material with the rest of it comprising of γ-Alumina and various other additives to enhance the chemical activity and stability of the catalysts at higher temperatures. The coating process involves sucking of this slurry on to the substrate, which results in highly non-uniform distribution of the washcoat around the perimeter of the channels within the converters. In a typical washcoated channel the washcoat thickness is observed to vary from around 200 μm near the corners to around 10 μm near the edges. As it is difficult to exactly measure the washcoat thickness distribution in the channels, it is typically assumed to be constant. Proper approximation of average washcoat thickness in relation with PGM or washcoat loading is essential for evaluating major modeling parameters like the geometric surface area and specific catalytic surface area of the channel. One such approximation which correlates washcoat thickness to washcoat loading [46, 47] is given by equation (2.20).

$$\delta_w = \frac{28.3168\, L_{\mathrm{w}} {D_{\mathrm{ch}}}^2}{4\rho_{\mathrm{wc}}(D_{\mathrm{ch}} - \delta_{\mathrm{s}})} \tag{2.20}$$

where $\delta_{\mathrm{s}}$is the substrate thickness in m, and $L_{\mathrm{w}}$is the washcoat loading in g/ft^3, and $\rho_{\mathrm{wc}}$is the density of washcoat in g/ft^3.

The washcoat loading and PGM loading can be correlated as

$$L_{\mathrm{PGM}} = L_{\mathrm{wc}}.\gamma \tag{2.21}$$

where L_{PGM} and L_{wc} are the PGM and washcoat loadings in g/ft^3 and γ is the ratio of weight-percent of PGM to washcoat.

Here the model parameter $F_{\mathrm{cat/geo}}$ denotes the ratio of the catalytic surface area to the geometrical surface area of the catalyst, i.e., the ratio of noble metal area available for catalytic reactions to the geometrical area of the cylindrical walls of the monolith channel and is evaluated according to

$$F_{\mathrm{cat/geo}} = \frac{\mathrm{Area_{cat}}}{\mathrm{Area_{geo}}} = D\,\frac{m_{\mathrm{cat}}}{M_{\mathrm{cat}}\Gamma_{\mathrm{cat}}\mathrm{Area_{geo}}} \tag{2.22}$$

which can also be expressed as

$$F_{\mathrm{cat/geo}} = D\,\frac{L_{\mathrm{PGM}}\,V_{\mathrm{c}}}{M_{\mathrm{cat}}\Gamma_{\mathrm{cat}}\mathrm{Area_{geo}}} \tag{2.23}$$

V_{c} is the volume of the channel, D is the dispersion. M_{cat} is the molecular weight of precious metal and Γ_{cat} is the surface site density in mol/m^2. Knowing washcoat thickness from equation (2.20), $\mathrm{Area_{geo}}$ can be easily evaluated from the geometry of the channel [48]. Finally the specific catalytic surface area S_{cat} used in equations 2.6, 2.7., 2.11 and 2.12 is evaluated according to

$$S_{\mathrm{cat}} = \frac{F_{\mathrm{cat/geo}}}{\delta_{\mathrm{w}}} \tag{2.24}$$

2.2. Dynamic Optimization

2.1.1. Formulation of Optimal control problem

Dynamic optimization problem is concerned with the solution of constrained differential-algebraic equations (DAE). A Dynamic optimization problem can be further categorized into parameter estimation and optimal control problems (OCP) [49]. A DAE constrained optimization problem with linear and nonlinear constraints is represented as follows.

$$\min \Phi(z,y,u,\beta) = \int_{t_0}^{t_f} L(z,y,u,\beta)dt \; + \; E(z(t_f),y(t_f),u(t_f),\beta) \tag{2.25a}$$

$$\text{s.t.} \quad \dot{z} = f(z(t), y(t), u(t), \beta),\ z(t_0) = z_0 \tag{2.25b}$$

$$g(z(t), y(t), u(t), \beta) = 0 \tag{2.25c}$$

$$u_{\mathrm{L}} \le u(t) \le u_{\mathrm{U}} \qquad y_{\mathrm{L}} \le y(t) \le y_{\mathrm{U}} \quad z_{\mathrm{L}} \le z(t) \le z_{\mathrm{U}} \quad \beta_{\mathrm{L}} \le \beta \le \beta_{\mathrm{U}} \tag{2.25d}$$

The "unknowns" in this optimization problem are the differential state variables *z(t)*, algebraic variables *y(t)*, control variables *u(t)*, all functions of the scalar "time" parameter $t \in [t_0, t_{\mathrm{f}}]$, as well as time-independent parameters β. Additional point or end time constraints may also be added. The objective function (2.25a) consists of two parts, an integral term accounting for the cost throughout the horizon $[t_0, t_{\mathrm{f}}]$, and a terminal cost at the final time.

An objective function with only the first part of eqn (2.25a), results in a Lagrange problem where $L(z, y, u, \beta)$ is called a Lagrange integrand.

$$\int_{t_0}^{t_f} L(z, y, u, \beta) dt \tag{2.26}$$

while on the other hand the Mayer problem consists only the terminal cost given by (2.25a)

$$E(z(t_f), y(t_f), u(t_f), \beta) \tag{2.27}$$

An OCP problem with the combination of these two yields a Bolza functional, and is known as the Bolza problem. It should be noted that these formulations are equivalent, and they can be interchanged [49, 50].

As the OCP includes a dynamic constraint in the form of a continuous-time differential equation, it contains an infinite number of decision variables: $z(t), y(t), u(t)$ for $t \in [t_0, t_{\mathrm{f}}]$. To solve it using a numerical optimization algorithm, it has to be approximated by a finite dimensional non-linear program (NLP). An approximation procedure discretizes the continuous-time formulation, into a discrete formulation making it suited for numerical algorithms. Direct solution methods are often used to solve such finite dimensional optimization

problems. The resulting NLP can be provided to a non-linear programming solver to obtain an optimal solution.

2.1.2. NLP solver

The resulting NLP from the discretization of the infinitesimal optimization problem to a finite dimensional problem can be solved using the Sequential Quadratic programming (SQP) or methods based on Interior point algorithms (LOQO [51], KNITRO [52], IPOPT [53]). In this thesis, IPOPT is used to carry out the optimization. IPOPT is designed to find local solutions of large scale non-linear optimization problems of the form.

$$\min\ f(z) \tag{2.28a}$$

$$\text{s.t.}\quad h_{\mathrm{L}} \leq h(t) \leq h_{\mathrm{U}} \tag{2.28b}$$

$$z_{\mathrm{L}} \leq x(t) \leq z_{\mathrm{U}} \tag{2.28c}$$

where $f: \mathbb{R}^n \to \mathbb{R}$ and $g: \mathbb{R}^n \to \mathbb{R}$ are objective and constraint functions, respectively, with z being the decision variable. In addition to the objective function and constraint values, IPOPT requires that user provide the first derivatives (jacobians) and second derivatives (hessians) of both the objective function and the constraints with respect to the control parameters. These values are necessary to formulate the Karush-Kuhn-Tucker (KKT) matrix. For more on IPOPT the readers are directed to Wächter et al [53]

2.1.3. Direct Methods

The direct solution methods for Differential Algebraic Equations (DAE)-constrained optimization problems are generally separated into two classes, known as the sequential and simultaneous approaches. In both methods, the decision variable (control policy) is represented by using an appropriate function approximation (e.g., piecewise constant parameterization) and determined from solving Non-linear Programming (NLP) problems. The difference between these approaches lies in the treatment of embedding the DAE. The single shooting method is a typical example of sequential approaches and the Direct multiple shooting and Direct collocation can be classified as typical simultaneous approaches.

2.1.3a. Sequential approach

Single shooting

The sequential approach can also be termed as the single shooting method. In the single shooting method, the NLP problem size is considerably small with the NLP optimization variable vector consisting of only the control parameters from the optimal control problem [54]. Given the initial conditions and a set of control parameters, the DAE model is solved within an inner loop controlled by an NLP solver, parameters representing the control variables are updated by the NLP solver itself. The obtained solution of the DAE system is used for the evaluation of the objective function, the constraints and the sensitivities treating the DAE system as an extrinsic black box. With the NLP solver updating the control parameters, the DAE system is subject to repetitive calls. The single shooting method is convenient due to its simplicity and reduced size of the NLP. The main drawback of this methodology is that the optimization is prone to failure for unstable systems when integrators fail to converge.

2.1.3b. Simultaneous approaches

The simultaneous approach can be broadly divided into two methods, namely the Direct multiple shooting method and the Direct collocation method.

Multiple shooting

The multiple shooting method is first presented by Bock et al [55], where the time horizon is divided into several sub time intervals and the initial value problem is transformed into a boundary value problem with the addition of continuity constraints to ensure continuity between two time intervals [56, 57]. Contrary to the sequential approach, not only the controls but also the initial conditions of the states in each subinterval are parameterized and are optimized. The parameterized values of the states at the beginning of each subinterval are used as initial conditions to solve an initial boundary value problem and evaluate the states at the end of each subinterval with the help of a DAE solver. The objective function, its sensitivities and the constraints (continuity constraints and path constraints) and their sensitivities (Jacobian of the continuity constraints and path constraints) are used to formulate the NLP problem.

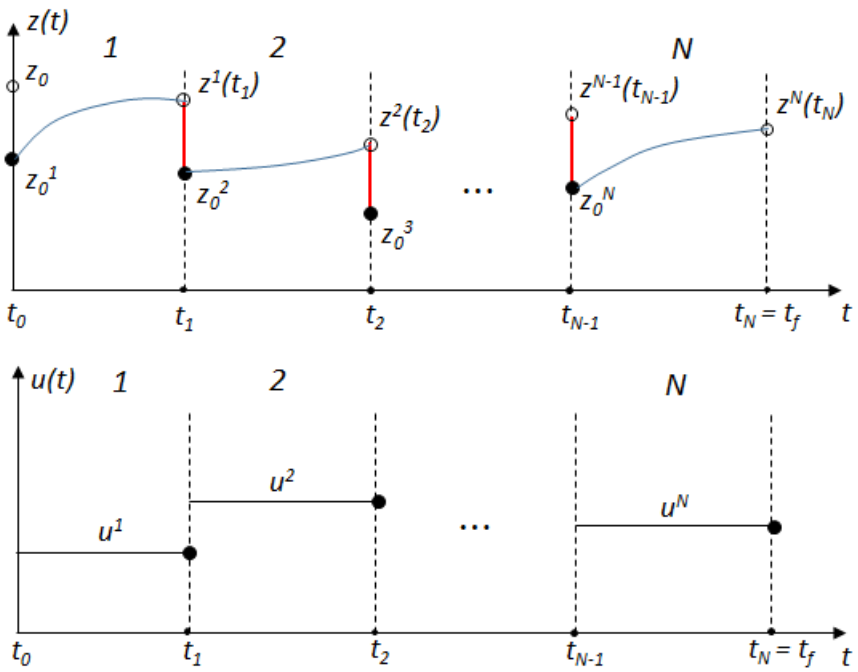

Figure 2.1. Multiple shooting description where the time horizon is divided in to segments and where each of the segments are integrated separately.

Here, the time horizon is divided into $l = 1, \dots N$ number of segments, as illustrated in **Figure 2.1**. In each of these segments, the DAE system is solved independently. At each shooting interval the DAE solution $z^{l-1}(t_{l-1})$ of the previous interval should be equal to the initial condition of the current interval z_0^l. This requirement is enforced by using continuity constraints. In addition, states at the beginning of each segment appear as decision variables. As integration is performed over shorter time intervals, numerical stability properties of the algorithm are improved. Additional inequality constraints for the state variables at the grid points $t_l, l = 1, \dots, N$ are also easier to include, as these are now decision variables. Even though multiple shooting offers numerical advantages over a single shooting approach, it should be emphasized that the resulting NLP becomes larger and more sensitivity information is required. To improve performance, exploitation of structure and parallelization should be applied. A multiple shooting approach leads to a NLP with DAE integration solved in an outer loop, and can be formulated as:

$$\min \ \Phi(z_N) \tag{2.29a}$$

or

$$\min \int_{t_0}^{t_f} \Phi(t)dt \tag{2.29b}$$

$$\dot{z}^l = f(z^l(t), y^l(t), u^l(t), \beta) \tag{2.29c}$$

$$z^l(t_{l-1}) = z_0^l \tag{2.29d}$$

$$g(z^l(t), y^l(t), u^l(t), \beta) = 0, \tag{2.29e}$$

$$t \in [t_{l-1}, t_l\,], \qquad l = 1, \dots, N$$

$$z^{l-1}(t_{l-1}) - z_0^l = 0, \qquad l = 2, \dots, N \tag{2.29f}$$

$$z_0 - z_0^l = 0 \tag{2.29g}$$

$$g_I(z^l(t_l), y^l(t_l), u^l(t_l), \beta) \leq 0, \tag{2.29h}$$

$$z_{\mathrm{L}} \leq z^l(t_l) \leq z_{\mathrm{U}} \tag{2.29i}$$

$$y_{\mathrm{L}} \leq y^l(t_l) \leq y_{\mathrm{U}} \tag{2.29j}$$

$$u_{\mathrm{L}} \leq u^l \leq u_{\mathrm{U}} \tag{2.29k}$$

In addition, the DAE system (2.29c)-(2.29e) is solved independently for each segment in an outer loop, thus obtaining state and variable profiles. Eqn (2.29f) enforces continuity of state profiles between segments. Initial conditions are defined in (2.29e), where z_0 are given values. Inequality constraints (2.29h) and variable bounds (2.29i)-(2.29k) are posed directly at grid points. For an equal segment and control input discretization, this leads to a total number of $n_v = N(n_z + n_u)$ decision variables and Nn_z additional equality constraints from the continuity enforcement and initial condition. For more information about this methodology readers are diverted to the following works [55–57].

Direct Collocation

Within the simultaneous approach, and in particular in the Direct collocation approach the states are approximated by polynomials whose coefficients are determined together with the control trajectory in the NLP solver [58, 59]. In the NLP formulation, the method of Orthogonal Collocation over Finite Elements (OCFE) is applied where the DAEs are discretized with an implicit Runge−Kutta scheme and the resulting nonlinear equations are solved only at optimal solutions. Therefore, intermediate solutions that may not exist or may require excessive computational cost can be avoided [49, 58]. An early overview of these approaches can be found in [49, 58–60].

The method of Direct collocation to discretize the dynamic optimization problem (2.25) and to solve with an appropriate NLP solver is described below using the approach presented in [60]. Here both the states and the controls are parameterized by using the method of Orthogonal Collocation on Finite Elements.

According to OCFE, the time horizon is discretized into n_e finite elements, and within each element i, n_c collocation points are chosen to represent the state and control variables as piecewise polynomial approximation of degree *K* as illustrated in **Figure 2.2**. These collocation polynomials are often formed using Lagrange interpolation polynomials, using the collocation points as interpolation points. In element i, the time at each collocation point τ_j is given by

$$t_i(\tau_j) = h_i(t_{i-1} + \tau_j) \quad , \quad \tau \in [0,1], \ \forall\, i \in [1..n_e], \tag{2.30}$$

where t_i is the time at the end of element i, which is called the mesh point of element i, and h_i is the length of element i. The element lengths are normalized so that the sum of all lengths equals 1. This normalization facilitates the optimization of t_f and t_0 by keeping element lengths constant.

The state in a given element i is expressed as

$$z_i(\tau) = \sum_{j=0}^{n_c} z_{i,j} \cdot l_j(\tau), \tag{2.31}$$

Where the Lagrange interpolation polynomial is

$$l_k(\tau) = \prod_{k=0,k\neq j}^{K} \frac{(\tau - \tau_k)}{(\tau_j - \tau_k)} \tag{2.32}$$

Similarly the control and algebraic variables are expressed as

$$u(\tau) = \sum_{j=1}^{K} u_{i,j} \cdot \overline{l_j}(\tau), \tag{2.33}$$

$$y(\tau) = \sum_{j=1}^{K} y_{i,j} \cdot \overline{l_j}(\tau), \tag{2.34}$$

And their respective Lagrange interpolation polynomials are given by

$$\overline{l_j}(\tau) = \prod_{k=1,k\neq j}^{K} \frac{(\tau - \tau_k)}{(\tau_j - \tau_k)} \tag{2.35}$$

Note that the basis polynomials are the same for all elements, due to the normalized time. In order to obtain the polynomial approximation of the state derivative $\dot{z}$ in element i, the collocation polynomial z_i is differentiated with respect to time. Using (2.31), (2.32) and applying the chain rule for differentiation, one can obtain

$$\dot{z}_i(\tau) = \frac{dz_i}{dt_i}(\tau_j) = \frac{d\tau_j}{dt_i} \cdot \frac{dz_i}{d\tau_j}(\tau_j)$$

$$\dot{z}_i(\tau) = \frac{1}{h_i} \cdot \sum_{j=0}^{n_c} z_{i,j} \cdot \frac{dl_j}{dt_i}(\tau_j) \tag{2.36}$$

Which can be written as

$$h_i f\left(z_{i,j}, u_{i,j}, y_{i,j}, \beta\right) - \sum_{j=0}^{n_c} z_{i,j} \cdot \dot{l}_j(\tau_j) = 0 \tag{2.37}$$

$$i = 1,2,\dots,n_e\,, \quad j = 1,2,\dots,K$$

The differential variables need to be continuous along the time horizon, while the control and algebraic variables are allowed to be discontinuous at the boundaries of the elements. There are different schemes for choosing the collocation points τ_j, with different numerical properties, in particular regarding stability and order of convergence. The most common ones are called Gauss, Radau and Lobatto collocation [49, 61]. In this paper we use Radau collocation, which always places a collocation point at the end of each element, and the rest are chosen in a manner that maximizes accuracy.

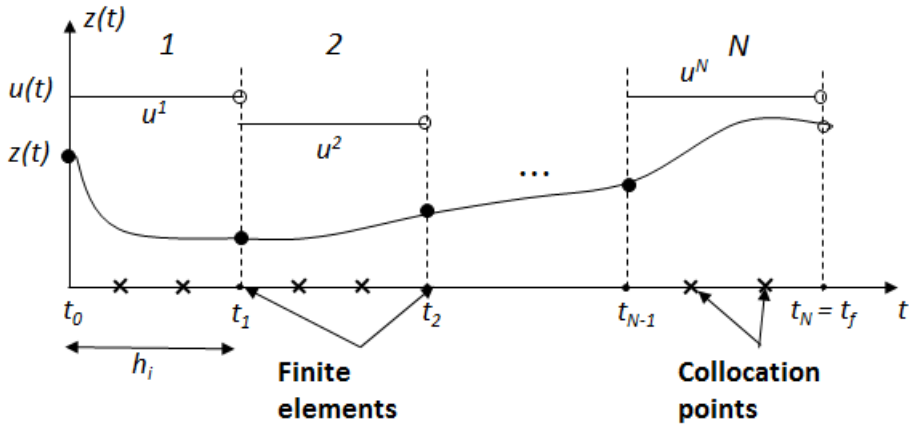

Figure 2.2. Direct collocation schematic representation.

2.1.4. Transcription of the dynamic optimization problem

The transcription of the infinite-dimensional dynamic optimization problem (2.25) into a finite dimensional NLP, using the collocation polynomials constructed in the previous section is presented in this section. The infinite-dimensional time-dependent variable *z* is approximated using polynomials, which can be represented using a finite number of values: the collocation point values.

As decision variables in the NLP we choose all the collocation point values $z_{i,k}$ of the states, the control variables $u_{i,k}$, the algebraic variables $y_{i,k}$ and the free parameters β. The vector containing all the NLP variables is given as:

$$Z_i = \left(z_{i,j}, y_{i,j}, u_{i,j}, \beta\right) \quad i = 1,2,\dots,n_{\mathrm{e}}, \quad j = 1,2,\dots,K, \tag{2.38}$$

Therefore if there are n_z states, n_y algebraic equations and n_u controls and n_β free parameters, the total number of optimization variables if n_{e} number of finite elements and n_{c} collocation points are chosen is given by

$$n_Z = n_z n_{\mathrm{c}} n_{\mathrm{e}} + n_{\mathrm{c}} n_y n_{\mathrm{e}} + n_{\mathrm{c}} n_u n_{\mathrm{e}} + n_z + n_\beta \tag{2.39}$$

With Radau collocation and the above choice, the transcription of (2.25) results in the following NLP:

$$\min \Phi(z_N) \tag{2.40a}$$

or

$$\min \int_{t_0}^{t_f} \Phi(t)dt \tag{2.40b}$$

$$h_i f\left(z_{i,j}, u_{i,j}, y_{i,j}, \beta\right) - \sum_{j=0}^{n_{\mathrm{c}}} z_{i,j} \cdot \dot{l}_J(\tau_j) = 0 \tag{2.40c}$$

$$g\left(z_{i,j}, u_{i,j}, y_{i,j}, \beta\right) = 0, \quad i = 1,2,\dots,n_{\mathrm{e}}, \quad j = 1,2,\dots,n_{\mathrm{c}}, \tag{2.40d}$$

$$z_{i+1,0} = z_{i,n_{\mathrm{c}}}, \quad i = 1,2,\dots,n_{\mathrm{e}} \tag{2.40e}$$

$$u_{\mathrm{L}} \le u_{i,j} \le u_{\mathrm{U}} \qquad y_{\mathrm{L}} \le y_{i,j} \le y_{\mathrm{U}} \qquad z_{\mathrm{L}} \le z_{i,j} \le z_{\mathrm{U}} \tag{2.40f}$$

The initial values for the states and algebraic variables are determined by the dynamic and initial constraints. The initial value for the control variables are however not governed by the dynamic

or initial equations, but is instead given by the collocation polynomial u_i. The bounds and path constraints (2.25d) are straightforward to transcribe into (2.40f), by only enforcing them at the collocation points. In order to determine the state derivative values at the collocation points, we enforce equation (2.25b) at all the collocation points, giving us the collocation equations (2.40c). These are not enforced at the start time, where the state derivative values instead are determined by the initial conditions. Finally, we add the continuity constraints (2.40e), to ensure continuity for the state. By solving the NLP (2.40), we may obtain an approximate solution to the dynamic optimization problem (2.25).

2.1.5 DASPKADJOINT

In this section, details about the solver used for solving the DAEs and gradient generation which are required for the optimization process used in chapter 3 are discussed. In this study, the implicit solver based on BDF method called DASPKADJOINT [62], is used for the computation of the sensitivities of differential-algebraic equations (DAE) by the adjoint method. Given a DAE depending on parameters,

$$\begin{cases} F(y, \dot{y}, t, p) = 0 \\ y(0) = y_o(p) \end{cases} \tag{2.41}$$

a vector of objective functions $G(y, p)$. Here n_y is the number of time dependent variables y as well as the dimension of the DAE system, and n_p is the number of parameters in the DAE system and let n_G be the dimension of the derived functions (objective and constraints). The Lagrange objective function can be represented as (2.42), where Φ can be either algebraic or diferential varaible.

$$G(y, p) = \int_{t_0}^{t_f} \Phi(t, y, p) dt \tag{2.42}$$

The sensitivity problem usually requires the evaluation of $\frac{dG}{dp}$, where p is a vector of parameters. In general, there are three methods available for computing gradients;

1) Finite difference method
2) Forward sensitivities
3) Adjoint method.

Finite Difference method

The finite difference method is the most commonly used method for quick and easy evaluation of the first derivatives. For few decision variables or control parameters usage of finite difference is feasible with low computational cost while presence of many control parameters add substantial computational cost and make them infeasible. If there are n_p decision variables, applying finite differences require $n_p + 1$ simulation runs when forward difference are used and $2n_p$ simulation runs when the central difference are used for only one gradient calculation.

An estimate of the first derivative of the cost function G using a first order forward difference approximation is as follows:

$$\frac{dG}{dp_i} = \frac{G(p_i + \epsilon_i) - G(p_i)}{\epsilon_i} + O(\epsilon_i) \tag{2.43}$$

Similarly an estimate of the first derivative of the cost function G using a central difference approximation is as follows:

$$\frac{dG}{dp_i} = \frac{G(p_i + \epsilon_i) - G(p_i - \epsilon_i)}{2\epsilon_i} + O(\epsilon_i^2) \tag{2.44}$$

A smaller step size is desired to reduce the truncation error $O(\epsilon_i)$ or $O(\epsilon_i^2)$ however a smaller step has the opposite effect on the cancellation error. Selecting the optimal step size for a certain problem is computationally expensive [63]. For this reason, the sizing of the finite difference step is not attempted and a constant increment size is used in evaluating the gradient. Although finite difference methods are problematic they are trivial to code, easy to understand and is a standard tool to check gradient calculations from other methods.

Forward Sensitivities

Given a DAE system (2.41) and an objective function given by (2.42). The sensitivity of the objective function with respect to the control parameters is given by $\frac{dG}{dp}$. Applying the chain rule yields the following sensitivity equations given by (2.45)

$$\frac{dG}{dp} = \frac{\partial G}{\partial y}\frac{dy}{dp} + \frac{\partial G}{\partial p} \tag{2.45}$$

In the above equation, $\frac{\partial G}{\partial y}$ and $\frac{\partial G}{\partial p}$ can be determined directly by taking their derivatives in the objective function. Meanwhile computation of $\frac{dy}{dp}$ requires the simultaneous solution of the original DAE with respect to each parameter and can be evaluated efficiently as presented in DASPK 3.0 [62]. Given the DAE system (2.41), sensitivity analysis produces an additional $n_s = n_p n_y$ sensitivity equations which are to be solved along with the original DAE system, which are presented below

$$F(y, \dot{y}, t, p) = 0 \tag{2.46}$$

$$\frac{dF}{dy} s_i + \frac{dF}{dy'} s_i' + \frac{dF}{dp} = 0, i = 1, \ldots., n_p$$

Where $s_i = dy/dp_i$ leading to

$$Y = \begin{bmatrix} y \\ s_i \\ \vdots \\ s_{np} \end{bmatrix}, \quad F = \begin{bmatrix} F(y, \dot{y}, t, p) \\ \frac{dF}{dy} s_1 + \frac{dF}{dy'} s_1' + \frac{dF}{dp_1} \\ \vdots \\ \frac{dF}{dy} s_{np} + \frac{dF}{dy'} s_{np}' + \frac{dF}{dp_{np}} \end{bmatrix} \tag{2.47}$$

And the obtained combined system can be written as

$$F(y, \dot{y}, t, p) = 0, \qquad Y(0) = \begin{bmatrix} y_0 \\ \frac{dy_0}{dp_1} \\ \vdots \\ \frac{dy_0}{dp_{np}} \end{bmatrix} \tag{2.48}$$

This system is transformed in to a non-linear system using the kth order BDF formula. This nonlinear system can be solved using different techniques which are described in detail in DASPK 3 [64] and the readers are directed to this document for detailed description.

Adjoint Sensitivities

While forward sensitivity computation is best suited to the situation characterized by a large number of derived functions and a small number of parameters, the reverse (adjoint) method is much more efficient when it is necessary to find the sensitivities of few derived functions with

respect to a large number of parameters. Given a DAE system (2.41) and an objective function given by (2.42), Main interest is in applying the adjoint method to compute the sensitivity of a derived function of the form (2.49)

$$G(y,p) = \int_{t_0}^{T} \Phi(t,y,p)dt \tag{2.49}$$

or, alternatively, the sensitivity of a function $\Phi(T,y,p)$defined only at time T. Assume that Φ is smooth enough so that Φ_p and Φ_y exist and are bounded, the adjoint system for the DAE system (2.41) with respect to the derived function $G(y,p)$ is given by

$$\frac{d}{dt}\left(\lambda^* F_{y'}\right) - \lambda^* F_y = -\Phi_y \tag{2.50}$$

For a scalar derived function $\Phi(T,y,p)$, the corresponding adjoint DAE system is given by

$$\frac{d}{dt}\left(\frac{\partial \lambda^*}{\partial T} F_{y'}\right) - \frac{\partial \lambda^*}{\partial T} F_y = -\Phi_y \tag{2.51}$$

The adjoint system is solved backwards in time. The initial conditions for the adjoint variables are taken to be (2.52), for the adjoint system (2.50)

$$\left(\lambda^* F_{y'}\right)\Big|_{t=T} = 0 \tag{2.52}$$

for the adjoint system (2.53) , for the adjoint system (2.51)

$$\left(\frac{\partial \lambda^*}{\partial T} F_{y'}\right)\Big|_{t=T} = \left(\Phi_y - \lambda^* F_y\right)\Big|_{t=T} \tag{2.53}$$

The sensitivities of the objective function with respect to the parameters *p* are given by

$$\frac{dG}{dp} = \int_{t_0}^{T} \left(\Phi_p - \lambda^* F_p\right)dt + \left(\lambda^* F_{y'}\right)\Big|_{t=t_0} (y_0)_p \tag{2.54}$$

Evaluating the integral in (2.54) amounts to solving the quadrature equations.

$$\dot{w} = F_p^T \lambda - \Phi_p^T \, , t^F \geq t \geq t^0 \tag{2.55}$$

$$w(t^F) = 0,$$

And when solved backward in time we get,

$$\frac{dG}{dp} = \left(w^T + \lambda^T y_p\right)\Big|_{t=t_0} \tag{2.56}$$

To avoid storing intermediate values for λ, it is generally advisable to integrate (2.53) and (2.56) simultaneously.

These expressions are valid for index-0 and index-1 DAE systems. For more information on this topic the reader is referred to DASPKADJOINT [62]. From the equations that describe the first order adjoint models (2.54), it becomes clear that one needs an efficient way to compute Jacobian-vector. Assuming the right hand side $F(t, y, p)$ of the original model (2.41) is continuously differentiable twice in both y and p, we can obtain first order derivative information via automatic differentiation. Automatic differentiation (AD) exploits the fact that every computer represented function can be given as a sequence of elementary arithmetic operations such as addition, subtraction and multiplication. By breaking the problem down to these operations, it is trivial to differentiate each of these elementary functions applying the chain rule. There are two main approaches available for AD, they are the forward and reverse mode [65]. The forward mode of automatic differentiation can be used to yield $\frac{dy}{dp}\frac{\partial G}{\partial y}$ in (2.45). Likewise, applying the reverse mode of AD is an efficient method to generate code for the computation of $F^T\lambda$. In both cases the products are evaluated directly, without accumulation of the full Jacobian matrices. The "cheap gradient theorem" estimates that both the matrix-vector products are evaluated at a cost not exceeding five evaluations of $F(t, y, p)$. Moreover, AD yields derivative information that has machine precision accuracy: the result is not affected by the truncation errors present in any finite-difference approximation [65].

The costs of adjoint method and forward method as represented roughly as

adjoint $$C_{adj} = 2C_f + C_{bs}^* + (N_f - 1)C_{bs} \tag{2.57}$$

forward $$C_{fw} = C_f + N_p C_{fs} \tag{2.58}$$

where C_f is the cost of forward integration for N state variables, C_{bs}^* denotes the cost for the first derived function, N_f is the number of derived functions, N_p is the number of parameters, C_{bs} is the cost of the backward integration for N adjoint variables, and C_{fs} is the cost of the forward integration for N sensitivity variables. Note that the cost of adjoint method (2.57) is roughly proportional to the number of derived functions (N_f), but insensitive to the number of parameters N_p, and that the cost of forward method (2.58) is roughly proportional to N_p, but insensitive to the N_f .

3. PGM loading Optimization

Design and optimization of catalytic converters is crucial for the automotive catalyst industry to meet the ever increasing stringent emission standards and efficient use of precious metals to reduce costs. Cold-start emissions constitute a large fraction of the total tailpipe emissions over a driving cycle and has been a topic of investigation for a long time [66–68]. The exhaust gas systems are not completely effective for the first few minutes during the cold start, where the catalyst is inactive due to low temperatures, resulting in pollutants passing unconverted till the catalyst heats up. Many methods have been investigated in the literature to control this problem. Preheating the catalytic converter electrically is a possible solution to this problem which is extensively studied [67, 69–72]. The other alternative can be the utilization of high-voltage batteries especially used in hybrid cars to draw enough power to heat up the converter very quickly so as to reduce cold start emissions [72]. Another possible solution to curb this problem is by placing the converter in close proximity to the engine manifold. But this leads to pressure drop and in turn reduces the engine efficiency due to continuous transient pulsations [73]. Non-uniform catalyst distributions in the catalytic converters present an alternative viable option to tackle this problem efficiently. The problem of reducing the cost of the precious metals and improving the ignition conditions of the catalytic monolith can be addressed simultaneously by creating optimal distribution of the active component of the catalyst along the length of the monolith.

Various studies investigating the effect of non-uniform axial distribution of precious metals along the length of the reactor with simple global reaction kinetics and different operating conditions on the performance of the catalytic converter are available in the literature [66, 74–80]. Firstly, Oh and Cavendish [80] examined the light-off behavior of three Pt distribution profiles along the reactor length and concluded that the light-off performance of the linear decreasing Pt distribution with more noble metal concentrated in the upstream section of the monolith is much better than the other cases. Psyllos and Philippopoulos [79] pre-assumed a parabolic function and showed that the performance of catalysts with parabolic axial catalyst distribution for CO oxidation is better than monoliths with uniform axial catalyst distribution. Khanaev et al. [77] formulated an optimization problem to determine the optimal axially non-uniform catalyst activity distribution along the fixed catalyst bed under isothermal conditions and proposed that uniform distribution profile performed better than a non-uniform profile. Khanaev et al. [76] showed that the non-uniform active component distribution is in many cases

more effective than the uniform distribution for CO oxidation over a Pt-containing monolith catalyst. The aforementioned studies indicated that non-uniform catalyst distribution can improve the performance of catalytic converters. However, an optimal catalyst distribution has not been identified. Khanaev et al. [75] also showed that in an adiabatic reactor the optimal profile is the one that monotonically decreases along the bed length in the case of an exothermic reaction and monotonically increases in the case of an endothermic reaction, while the uniform active component distribution profile is found to be optimal for a first-order reaction in an isothermal reactor. The optimization of the loading pattern for improving warm-up catalyst performance using an optimization algorithm has been performed by Tronci et al. [68], Kim and Kim [81] and Kim et al. [66]. A zone-structured catalyst by dividing the channel length in to 2 zones is studied by Tronci et al. [68], showing that a high noble metal surface area in the upstream section of the monolith significantly minimizes the cold start pollutant emissions. Tronci et al. [68] also studied the effects of aging due to sintering and reported that presence of inert material at the inlet improves the performance of the catalysts especially when the catalyst suffers from sintering. Recently, Al-Adwani et al. [74] evaluated the effect of different precious metal distributions in a monolith for CO oxidation and showed that front loaded design performs better than other designs. Abedi et al. [82] experimentally compared the difference in performance between a two-zone non-uniformly loaded catalyst and uniformly loaded catalyst of equivalent total loading of Pt for CO, NO and hydrocarbon oxidation at different conditions for a Diesel Oxidation Catalyst (DOC). They concluded that the zone-structured catalyst with high loading in the upstream section of the catalyst performed better than the uniformly loaded catalyst at the respective conditions. In most of the aforementioned studies, global reactions with two phase heterogeneous one-dimensional models were used to model the system and the optimization is performed with pre-assumed decay or parabolic functions. 1D two phase models [32, 38, 39, 80, 83–86] are used as the reliable modeling tool to model automotive catalytic converters because of their simple formulation and associated minimum computation costs when compared with 2D [30, 87–89] models. In a typical 1D model the diffusion effects are lumped in to the kinetic parameters and radial variations are neglected. Also the kinetic parameters obtained by fitting the model to experiments, have limited range of applicability and are subjected to tuning. One of the major limitations of the 1D model is its inapplicability to multi-layered washcoat applications like SCR (Selective catalytic reduction)/PGM (Platinum group metals) dual layered catalysts [14, 90]. 1D +1D models have evolved to be more detailed and accurate predictive tool to model catalytic converters [14, 15, 40, 42]. Even though the

computational effort involved is more than typical 1D model because of the addition of reaction-diffusion in radial direction, the model is more accurate and can be used with detailed micro-kinetic mechanisms as well as to model dual-layered catalysts. In addition most of the studies in the literature assumed that the washcoat thickness does not change with change in PGM loading which depends on the type of wash coating strategy adopted. Also in most of the out optimization studies. Gradient based optimization schemes even though are associated with derivative overhead costs always have been known to converge faster to a more reliable optimal solution. Von Schwerin et al. [91], Raja et al. [92] and Minh et al. [54] have successfully applied gradient based optimization schemes like sequential quadratic programming to one-dimensional and two-dimensional reactive flows with detailed chemistry.

The objective of this current study is to develop a methodology to optimize the precious metal loading profile (PGM loading) in zone-structured catalytic converters. The 1D + 1D reactor model used in the following study with all the respective governing equations are described in detail in **Section 2.1.1**. Also the PGM loading and washcoat thickness correlation and the method used in the present study to evaluate the volume averaged specific catalytic surface area is described in detail in **Section 2.1.4**. The chapter is organized as follows. The optimization problem formulation and optimization algorithm adopted in this study along with third party software [53, 93] are described in detail in **Section 3.1** and **3.2**. In order to demonstrate the efficacy of the method, two application cases in **Section 3.3** and **3.4** are considered, CO oxidation on platinum (Pt) based DOC catalyst and total CH_4 oxidation on palladium (Pd). For both the cases, the model is used to predict the optimum loading profile with constant amount of PGM which would improve the performance of the catalyst under transient operation. For the first case light-off experiments of Chan et al. [94] are used along with the 1D+1D model to formulate the kinetics. Similarly, for the second case, aging experiments for methane oxidation on Pd/Al_2O_3 are performed at different conditions which are used to formulate the kinetics. Later the developed kinetics and the model are used to formulate an optimization problem to optimize catalytic activity profile in terms of PGM loading axially along the channel length for constant amount of PGM loading (Pt or Pd), to reduce light-off temperature in the first case and to improve steady state conversion in the second case. The main advantage of using adaptive global kinetics over detailed kinetics in simulating the system is its simple formulation with the absence of surface species which reduces the number of governing equations to be solved thereby reducing the computational effort and saving the total time of simulation. Particularly while solving an optimization problem, the model is evaluated numerically over a wide range

of the control parameters that are to be optimized. This results in repeated evaluation of the model which is computationally expensive.

Here in the present study, a zone-structured optimal PGM loading profile, where the catalyst is divided into *N* zones axially which can be experimentally prepared is suggested. The optimal loading and length of each of these zones are evaluated by the model. Most of the studies reported in the literature have ignored the influence of varying washcoat thickness on diffusion limitations with changes in PGM loading [68, 74]. This plays an important role because at higher loadings the washcoat thickness is high resulting in the appearance of severe diffusion limitations affecting the performance [95]. The present study takes this important effect into consideration and demonstrates the difference in the results. Finally, the optimized loading profile is analyzed for performance in comparison with the uniform loading in both the cases. Besides using the 1D+1D model, derivative based optimization schemes which require the derivative of the objective function with respect to the control parameters is used for optimization which greatly enhances the complexity in obtaining the numerical optimal solution. The numerical solvers and the software used along with the solution methodology adopted to solve such a numerical problem are described in detail in **Section 3.1** and **3.2**. The results of the optimization applied to 2 application cases are presented in **Section 3.3** and **3.4**. The main advantages of using such a methodology apart from obtaining a quick convergence is the independency of the model from the number of control parameters to be optimized. The methodology outlined in this work is robust and can be effectively employed to other applications.

3.1. Optimization Formulation & Solution methodology

The primary objective of the present study is to demonstrate that this tool developed can be used to obtain a zone-structured non-uniform loading profile which would improve the overall conversion or decrease the overall cumulative emissions over a given period of time. Further this model can also be extended to obtain the maximum amount of PGM that can be reduced in order to achieve better than or equal performance as a uniform loading catalyst by setting up an upper iteration loop. In order to obtain an optimal non-uniform loading distribution axially along the length of the channel, the channel is divided into *N* zones. Zone-structured solution is preferred over typical polynomial based solution because of its relative simplicity in fabrication and experimental testing when compared over polynomial solution. The most important decision variables that are to be optimized are chosen to be the PGM loading in each

zone and length of each corresponding zone. The objective is to maximize the conversion and reduce the overall cumulative emissions. Two important constraints are considered which control the directions of the solution. The first states that the sum of the product of the PGM loading in each zone and its corresponding length should be equal to the product of total PGM loading and the total length of the channel. These constraints ensure that the optimal solution is always comparable to a chosen standard uniform PGM loading solution or in other words the total catalytic surface area available always remains equivalent to that of uniform loading and is given by equation (3.5). The second constraint is a linear constraint which restricts the sum of the lengths of all the zones to the total length of the channel and is given by equation (3.6).

In the present study, *sequential methods*, also known as *control vector parameterization*, where only the control variables are discretized is employed. The parameterization of controls and states transform the dynamic optimization problem into a finite dimensional optimization problem. The nonlinear problem (NLP) size is considerably small with the NLP optimization variable vector consisting of only the control parameters from the optimal control problem. Given initial conditions and a set of control parameters, the differential-algebraic equations (DAE) model is solved within an inner loop controlled by an NLP solver, parameters representing the control variables are updated by the NLP solver itself. The obtained solution of the DAE system is used for the evaluation of the objective function and the constraints. The DAE system obtained by discretizing the PDE by method of lines approach is usually stiff, especially due to the presence of nonlinear kinetics. Therefore the adjoint DAE solver DASPKADJOINT [62], based on backward differentiation formulas (BDF) is used for the solution of the initial value problem. The derivative vector which comprises of the gradient of the objective function with respect to the sensitivity parameters is computed using a DAE sensitivity algorithm that is incorporated within DASPKADJOINT software. The adjoint system to be solved is generated via server-based automatic differentiation software TAPENADE [93] for forward and reverse mode. The partial differential equations (PDE) used to describe the system are first transformed in to ordinary differential equations (ODE) by discretizing the system in space by method of lines. The residual ODE's dependent on time are then differentiated with respect to the states and sensitivity parameters in the reverse mode. The main advantage of the reverse mode is that the calculation of derivatives is dependent only on the number of scalar functions (objective and constraints) as opposed to the number of input variables as is the case with the conventional forward mode. This allows the evaluation of sensitivity of a function with respect to large number of independent parameters. The constraint

Jacobian matrix is evaluated analytically. The objective function and its derivatives along with the constraints and their derivatives form an NLP problem. The following NLP can be solved quite efficiently using the IPOPT algorithm [53] best suited for large-scale non-linear programming. This algorithm adapts a barrier approach, where the bound constraints are replaced by logarithmic barrier terms which are added to the objective function.

The PDEs associated with the 1D+1D model (chapter 2 Equations 1-4) are transformed into ODEs by discretizing them in space using the finite difference approach. The residual ODEs can be generally solved by two approaches. The first approach is the coupled approach and the second is the decoupled approach. In the coupled approach all the ODEs are solved at once in time which leads to the formation of a large scale ODE system with a large Jacobian bandwidth which is prone to instabilities. On the other hand, in the decoupled approach the ODEs are solved at each axial position in time with forward marching in space, this approach leads to smaller scale ODE system with low Jacobian bandwidth and this approach is more stable. It is observed that the decoupled approach gives similar solution as the coupled approach when smaller time steps are chosen for integration and deviates from the coupled approach solution when large time steps are chosen.

In the present study, apart from solving the 1D+1D model and evaluating the objective function, the aim is also to obtain the derivatives of the objective function with respect to the control parameters. Therefore, the coupled approach is chosen over the decoupled approach which leads to a straightforward evaluation of the derivatives in time. A flowchart illustrating the optimization methodology is presented in **Figure 3.1**.

The general optimization problem formulation employed for both the cases is as follows.

$$\max(X_{\mathrm{CO}}\ or\ X_{\mathrm{CH_4}}) \tag{3.1}$$

$$F(t, x, x', p) = 0,\ \ x(t_0) = x_0 \tag{3.2}$$

$$P_{\min} \ \leq \mathrm{P}_i \ \leq P_{\max} \tag{3.3}$$

$$L_{\min} \ \leq \mathrm{P}_{N+i} \ \leq \ L_{\max} \tag{3.4}$$

$$\sum_{i=1}^{N} P_i \cdot P_{N+i} = L \cdot (\mathrm{PGM_{total}}) \tag{3.5}$$

$$\sum_{i=1}^{N} P_{N+i} = L \tag{3.6}$$

where $\mathrm{PGM_{total}}$ is the total uniform loading. L is the total length of the channel. $\boldsymbol{P}$ represents the control parameters while $P_{\min}$, $P_{\max}$, $L_{\min}$ and $L_{\max}$ denote the lower and upper bounds on the control parameters. N denotes the number of zones.

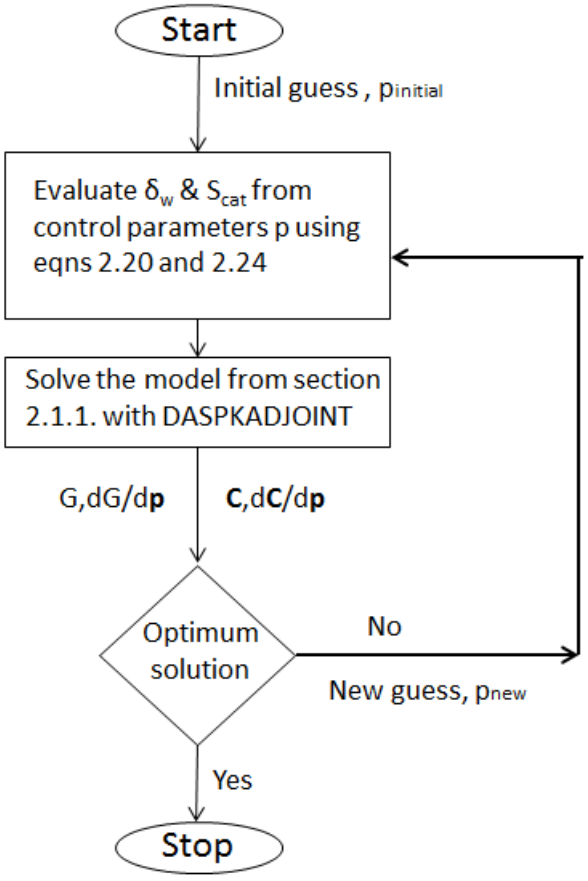

Figure 3.1. Flowchart of the methodology to solve the problem

3.2. Numerical Implementation

A new Fortran code has been developed to implement the described 1D+1D model. It is coupled with a Fortran version of the implicit DAE solver DASPKADJOINT [62], which was

chosen due to the large number of differential equations (up to 1280 for the case in **Section 4**). The optimization package IPOPT [53] is also available in Fortran.

The functions that compute the derivatives for the adjoint system of differential-algebraic equations are generated by the automatic differentiation tool TAPENADE [93]. It is a server-based tool, i.e., the original DAE functions of the Fortran code need to be uploaded to the TAPENADE server in order to generate source code for their derivatives.

3.3. Application 1: CO oxidation on Pt/Al_2O_3

3.3.1. Background

One of the key components of a diesel exhaust emissions control system is the diesel oxidation catalyst (DOC). The DOC catalyst is typically platinum (Pt) based with Al_2O_3 support. It promotes catalytic oxidation of several exhaust gas components by oxygen, which is present in ample amounts in a diesel exhaust. The main oxidation reactions occurring on a DOC are CO oxidation, H_2 oxidation and HC oxidation to CO_2 and water. Oxidation of NO to NO_2 is another important reaction that occurs on a DOC, which provides a sufficiently high NO_2/NO_x-ratio for a subsequent SCR catalyst which is placed after the DOC in diesel exhaust emission control systems [74, 76, 82, 94]. Therefore, the activity of the DOC has a strong influence on the whole after-treatment system. Since hydrocarbons exhibit similar characteristics as CO and are all closely related, in the present case only CO oxidation reaction is considered to optimize the precious metal loading profile in a DOC.

3.3.2. Kinetic modeling

First the CO oxidation light-off experiments over Pt based DOC [94] are used to formulate the global adaptive kinetics with the 1D +1D model.

The experiments were conducted over a DOC catalyst which was aged by subjecting the catalyst to different aging methods spanning over different time scales and conditions. This resulted in change of dispersion which is evaluated experimentally and an aging to temperature correlation is reported in the study. Five different light-off curves with different dispersion values respectively corresponding to different specific $F_{cat/geo}$ (48.4, 20, 11.4, 4 & 1) values are chosen. The global rate expression incorporating the inhibition effect of CO based on Langmuir-

Hinshelwood kinetics is considered to model the kinetics of CO oxidation [96]. The pre-exponential factor k_{oxi}, activation energy E_{oxi}, CO adsorption constant k_{ads} and heat of adsorption E_{ads} are calibrated by using the Levenberg-Marquardt algorithm to minimize the least squares residual between experimental and simulations.

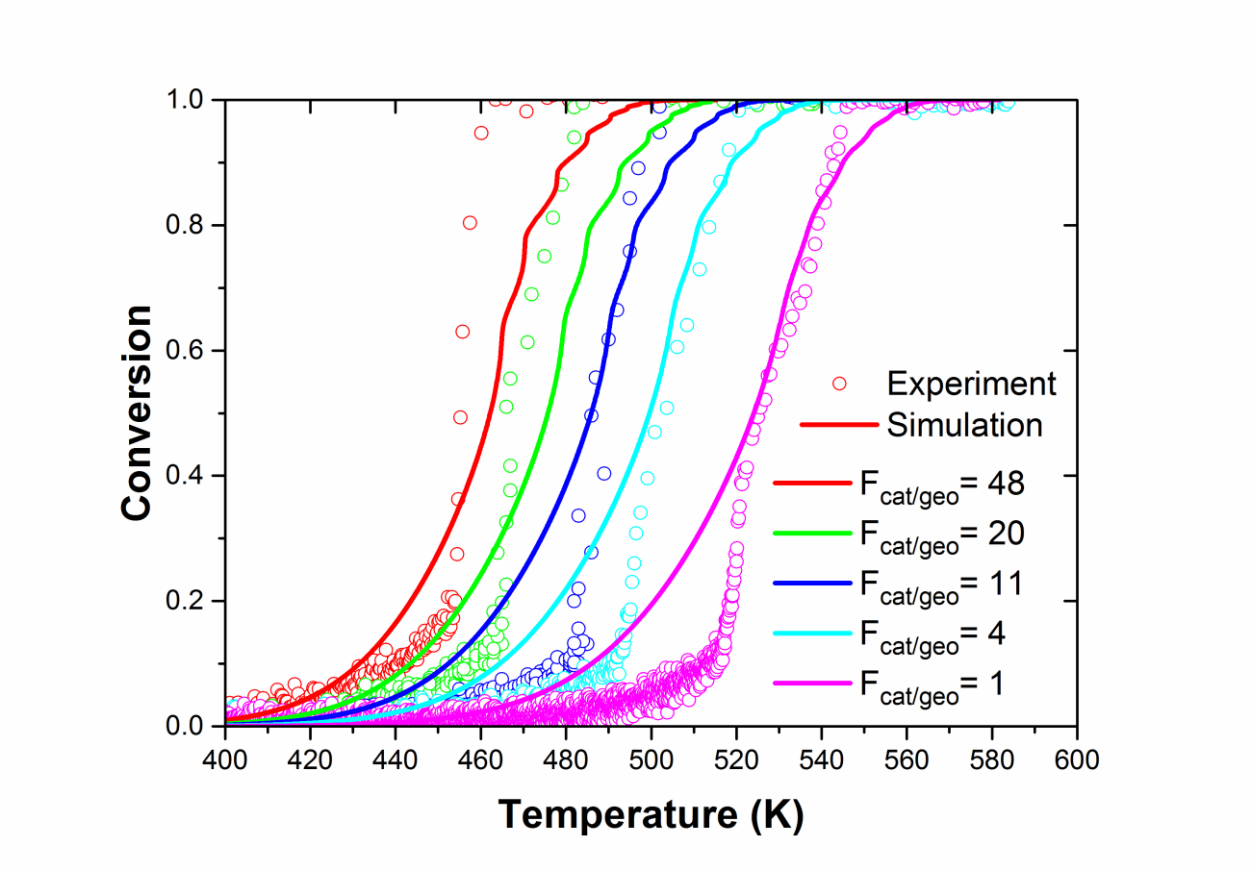

Figure 3.2. Comparison between experimental and simulation of different aged light off curves for CO oxidation on Pt.

Table 3.1. Rate parameters for CO oxidation on Pt/Al_2O_3

Parameter	value	unit
k_{oxi}	3.14794·1010	mol/m2 s
E_{oxi}	87200	J/mol
k_{ads}	70.019	[-]
E_{ads}	11500	J/mol

The rate kinetics for different catalytic loading are obtained by multiplying the rate with the corresponding specific catalyst surface area evaluated by equation (2.24). The derived values of the kinetic parameters are listed in **Table 3.1** and the model parameters used for the simulation are tabulated in **Table 3.2**.

$$r_{\mathrm{CO}} = \frac{k_{\mathrm{oxi}} e^{\frac{-E_{\mathrm{oxi}}}{RT}} x_{\mathrm{CO}} x_{\mathrm{O_2}}}{(1 + k_{\mathrm{ads}} e^{\frac{-E_{\mathrm{ads}}}{RT}} x_{\mathrm{CO}})^2} \tag{3.7}$$

It can be seen from **Figure 3.2.** that the 1D + 1D model with the evaluated parameters is able to simulate the light-off behavior satisfactorily for different $F_{\mathrm{cat/geo}}$ values demonstrating the effectiveness of the adaptive kinetics.

Table 3.2. Model parameters used for the simulation of CO on Pt/Al_2O_3

Parameter	value	unit
$\mathbf{PGM_{Tot}}$	147	g/ft^3
GHSV	40000	h^{-1}
CPSI	400	[-]
$\boldsymbol{\tau}$	3	[-]
$\boldsymbol{D_{ch}}$	0.0013	m
$\boldsymbol{\varepsilon_{wc}}$	0.41	[-]
$\boldsymbol{d_p}$	100	nm
L	0.027	m
$\boldsymbol{\delta_s}$	$1.016 \cdot 10^{-4}$	m
$\boldsymbol{\rho_{wc}}$	1500	kg/m^3
$\boldsymbol{\lambda}$	1.5	$W\ m^{-1}\ K^{-1}$
$\boldsymbol{c_w}$	1300	$J\ kg^{-1}\ K^{-1}$

3.3.3. Effect of washcoat thickness

Washcoat thickness plays an important role in modeling and understanding the limitations of diffusion especially in porous structures. Change in the washcoat thickness varies the washcoat volume which will result in change in the total washcoat loading and in turn PGM loading but the specific catalytic surface area remains the same. In order to study the effect of change in washcoat thickness, the kinetics obtained from the previous **Section 3.2** is used with the 1D + 1D model. The model parameters used for the simulations are tabulated in Table 3. Simulations are performed with five different wash coat thicknesses 30 µm, 40 µm, 50 µm, 51 µm and 60 µm, which correspond to 126 g/ft^3, 168 g/ft^3, 210 g/ft^3, 214 g/ft^3 and 252 g/ft^3 PGM loading, respectively.

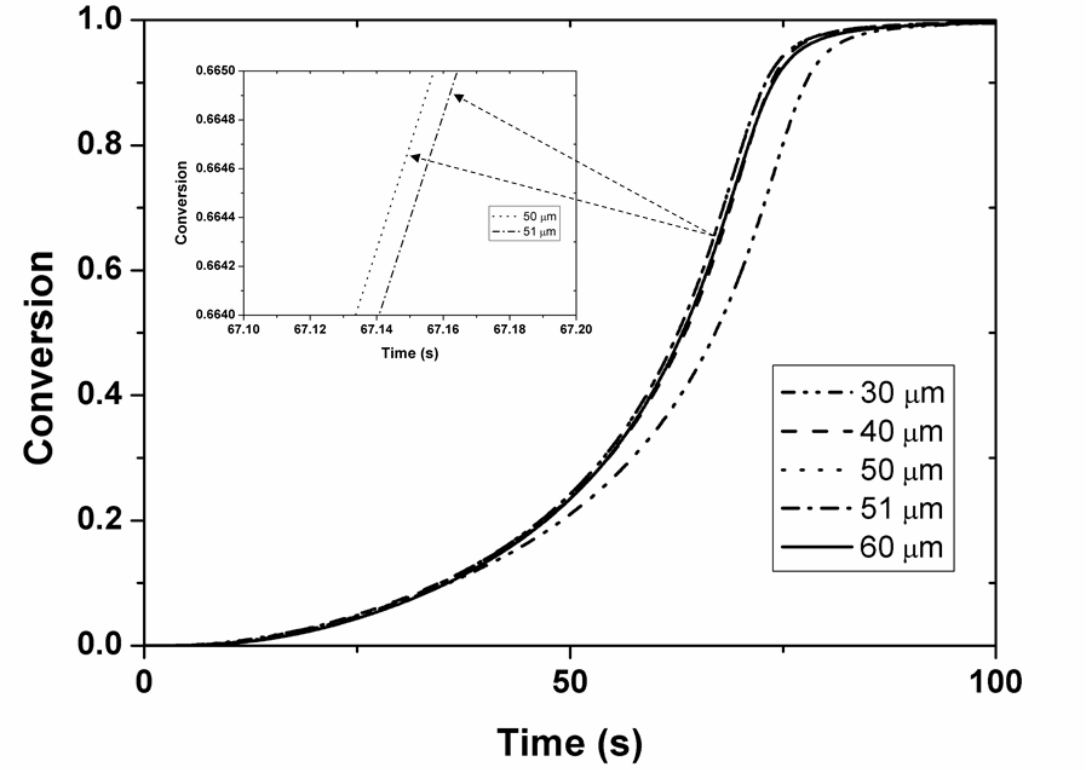

Figure 3.3. Effect of washcoat thickness on the conversion for CO oxidation on Pt.

Figure 3.3 describes the effect of change in the washcoat thickness over conversion for uniform catalyst loading. It can be inferred that starting from 30 μm with increase in washcoat thickness the light off temperature decreases. But this trend reverses and the light off temperature starts to increase beyond 50 μm (reversal effect can be clearly observed at 51μm when compared to 50μm from the **Figure 3.3**) due to severe diffusion limitations. At higher washcoat thickness the reactor operating in internal diffusion limited regime fails from the total utilization of the washcoat resulting in the reduction of performance. This re-emphasizes the importance of washcoat thickness in the design of catalytic converters. The other major inference from this study is that the improvement in performance is directly proportional to PGM loading up to a certain value beyond which the relationship reverses, resulting in decline in the performance due to increase in washcoat thickness, which impose severe diffusion limitations.

3.3.4. Optimization problem formulation

In this case, the optimization methodology described in **Section 2.4** is utilized to obtain the optimum zone-structured non-uniform loading profile for 3 subcases, where the catalyst is divided into 2, 3, and 4 zones, respectively. The optimum loading and length of each of these zones, which will reduce cumulative emissions of CO at the exit and improve steady state conversion, are evaluated by optimization. The number of control parameters to be optimized in each of these sub cases would be 2*N* respectively, where *N* denotes the number of zones the catalyst is divided. One nonlinear equality constraint which will hold the total amount of loading equivalent to fixed loading is incorporated. The optimization solution in each of these sub cases is compared with the uniform loading case of 100 g/ft^3. The upper and lower bounds on the first *N* control parameters ($\boldsymbol{P}_{\mathbf{max}}$ & $\boldsymbol{P}_{\mathbf{min}}$) were chosen to be 1000 g/ft^3 and 10 g/ft^3 which corresponds to an $F_{cat/geo}$ value of 217.2 and 1.29 and washcoat thickness of about 237 μm and 2.37 μm. The reason for choosing the minimum value of PGM loading to be 10 g/ft^3 ($F_{cat/geo}$ value of 1.29) rather than 1 g/ft^3 ($F_{cat/geo}$ value of 0.128) is to avoid inert zones particularly at the end of the channel. Presence of inert or zones with low PGM loading will lower the reaction rates affecting steady state conversion as that part of channel can operate far from mass transfer controlled regime[97]. Similarly the upper and lower bounds on the next *N* control parameters, i.e., the zone lengths ($\boldsymbol{L}_{\mathbf{max}}$ & $\boldsymbol{L}_{\mathbf{min}}$) are chosen to be *L-(N-1)* mm and 1 mm, so that the minimum length of any of the *N* zones would be at least 1 mm. The optimization problem is formulated for a typical fast light-off case for cold start emissions in a monolith, i.e., the catalyst is at 300 K at the start of the operation with CO and other exhaust gases entering the monolith at 523 K. In all the 3 subcases, the channel is divided into 28 grid points in the axial direction and 10 grid points in the radial direction. The number of control parameters are 4, 6 and 8 for each of the 3 subcases respectively. A typical illustration of zone-structured architecture used in the present study is presented in **Figure 3.4.** As shown in **Figure 3.4**, equal zone lengths are taken as initial guesses to start the optimization. As mentioned in **Section 2.4**, the system is solved in a coupled approach leading to 980 ODE equations, which are solved at once in time.

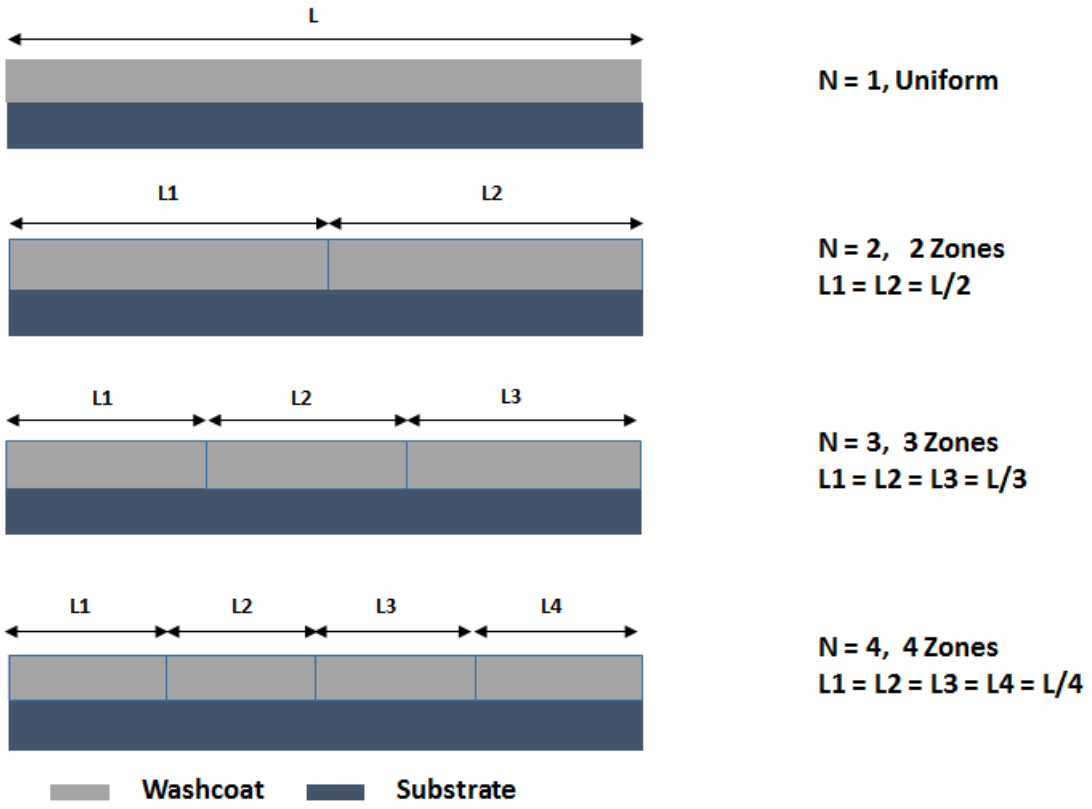

Figure 3.4. Zone structured (Uniform, 2, 3, 4 zones) catalyst architecture.

3.3.5. Comparison between uniform loading and optimum loading profile

The results from the optimization of zone-structured non-uniform PGM loading profile are presented in **Figure 3.5**. It can be observed from **Figure 3.5** that the optimum loading profile has more active catalytic substance at the entrance, i.e. in zone 1, than at the rear part of the channel for all the three cases having different number of zones. This result is in agreement with the findings of other researchers, who have proposed that for an exothermic reaction

having more active substance at the inlet would improve the performance of the catalyst.

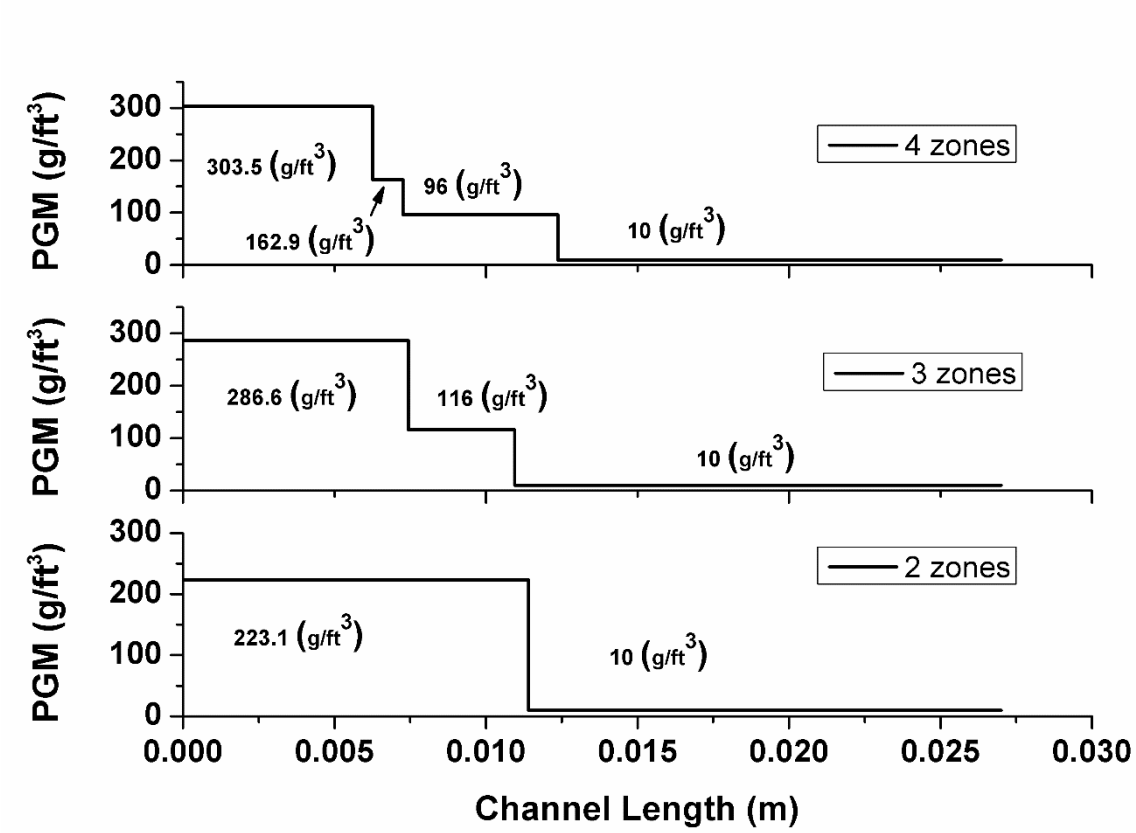

Figure 3.5. Optimum loading distribution for different number of zones.

Possibility of appearance of severe diffusion limitations at higher PGM loadings has restricted the optimizer to limit the PGM loadings in the zone 1 to loading value of 303.5 g/ft^3 which corresponds to washcoat thickness of about 72.2 μm in case 1, to 286.6 g/ft^3 which corresponds to washcoat thickness of about 68.2 μm in case 2 and 223.12 g/ft^3 which corresponds to washcoat thickness of about 53 μm in case 3.

Even though not reported in the present study, it was observed that if the correlation between PGM loading and washcoat thickness is not employed, i.e., if washcoat thickness used is held constant irrespective of the loading, the magnitude of PGM loading in the first zone reached the upper limit of the loading used for the simulation which is 1000 g/ft^3 in all the four cases. In all the cases, it can be observed that in the last zone, the loading is equivalent to the minimum permissible value of 10 g/ft^3. This ensures that the rear part of the channel operates in the mass transfer controlled regime and also avoids reduction of the steady-state conversion.

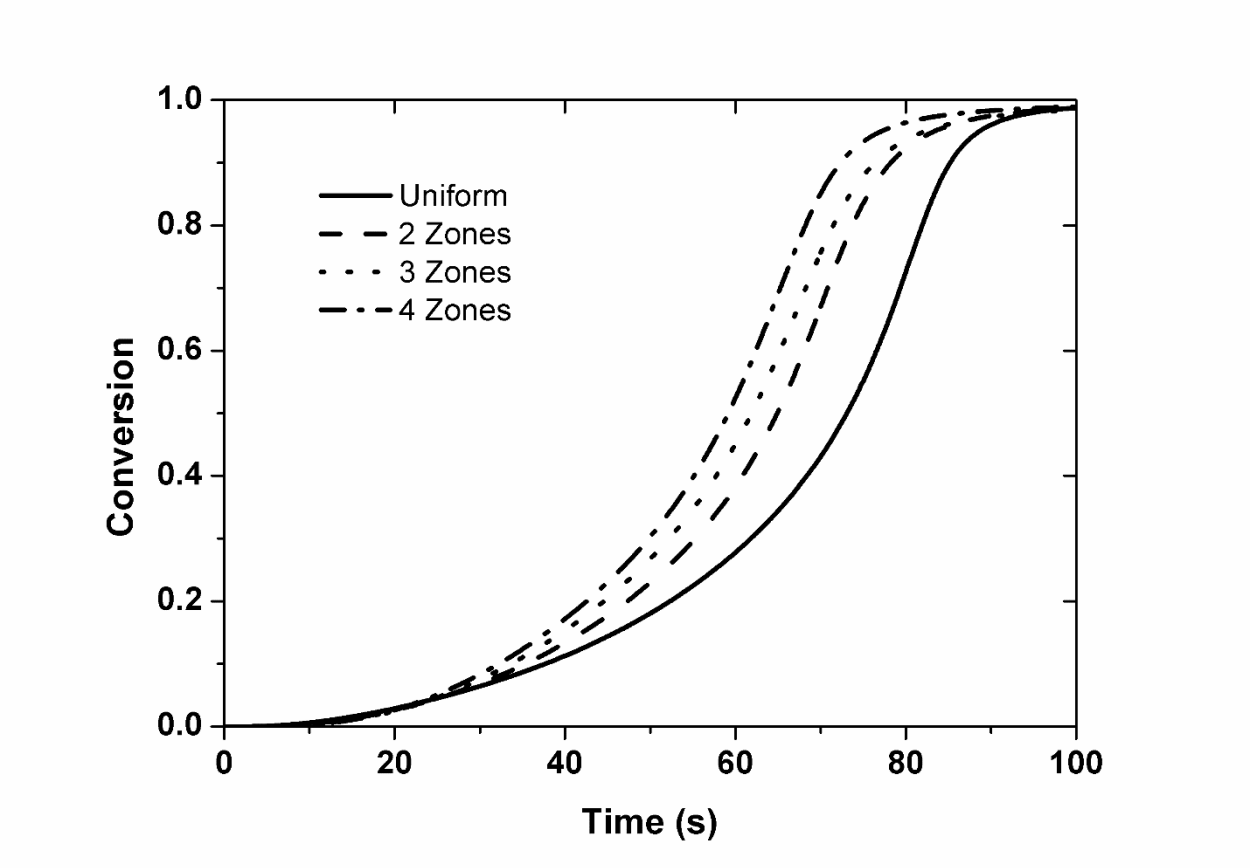

Figure 3.6. Comparison between Uniform and optimum loading profile performance for CO oxidation on Pt for different number of zones.

Figure 3.6 describes the comparison of CO conversion versus time between the uniform loading and optimum loading profile for all the 3 cases. It can be inferred that with the optimum loading profile the light off temperature decreased and hence resulting in lesser cumulative emissions than the uniform case. In case of the optimum loading profile, the decrease in light-off temperature can be attributed to the presence of more active substance at the inlet resulting in higher rates and higher exothermic temperatures which propagate fast throughout the catalyst improving the performance. From **Figure 3.6**, it can be also derived that the result improved with increase in the number of zones.

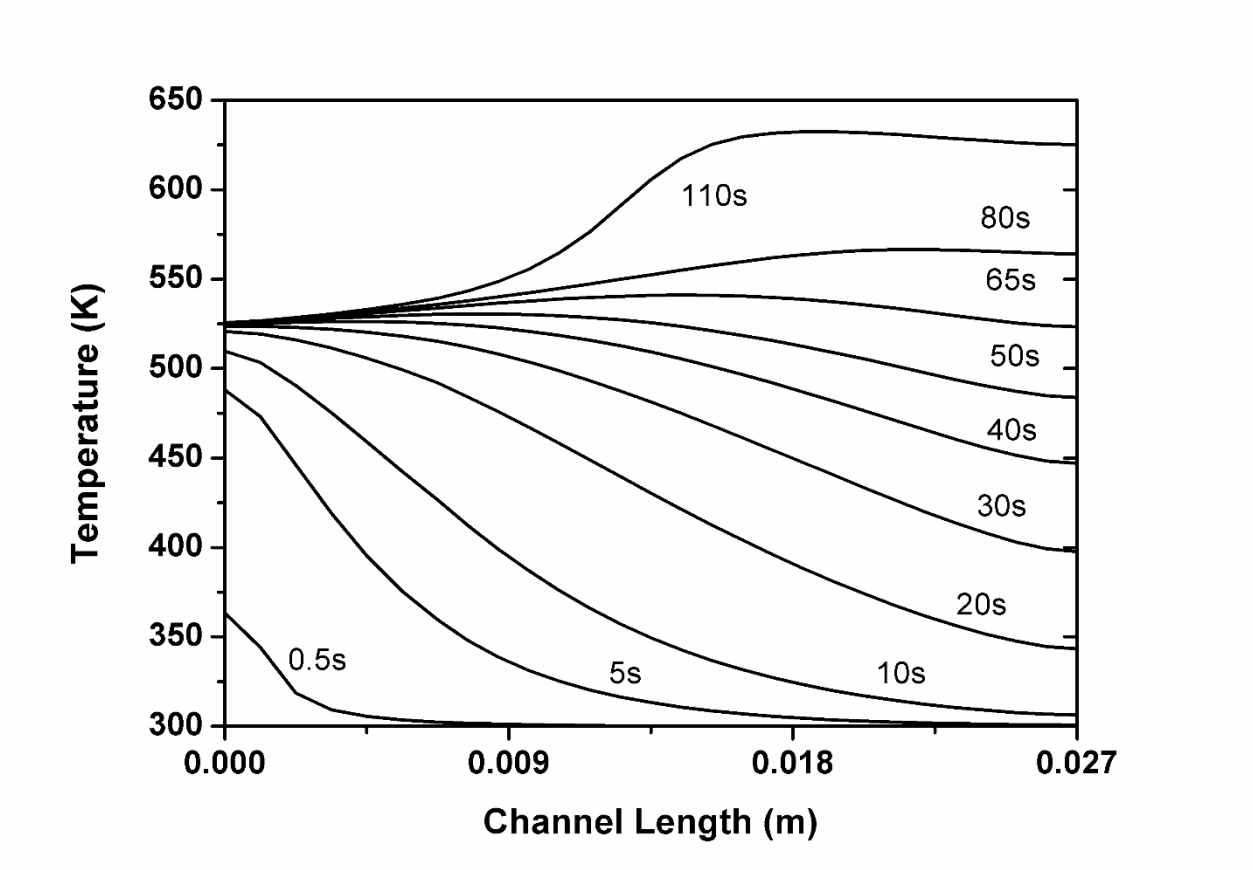

Figure 3.7. Evolution of uniform loading solid temperature profile for CO oxidation on Pt.

The better performance of the optimum loading profile compared to the uniform loading can be explained by analyzing the evolution of the solid temperature profiles of the former and the later with time for the sub case with 4 zones. Firstly, the solid temperature profiles along the length of the catalyst at different time instants for the uniform loading distribution case are shown in **Figure 3.7**. In general four distinct phases of operation can be identified occurring in series along the length of the channel for the case of uniform loading distribution [68, 97] from **Figure 3.7.** Firstly, the cold monolith is heated by the incoming hot fluid and heat transfer within the channel during this phase heat transport is only by convection and this can be termed as the first phase. During this phase the reactor typically operates in kinetically controlled regime where the reaction rates are extremely low resulting in no generation of heat.

Also the fluid-to-solid mass transfer rates are much faster compared to the reaction rates maintaining almost similar fluid and solid phase concentrations. In the second phase the heat generated from the exothermic reactions at the entrance is propagated forward by convection and solid phase conduction. In the third phase, the heat generated from the exothermic reactions propagate backwards in the direction opposite to the gas flow via solid phase by conduction.

The reactor operates in internal mass transfer controlled regime during this phase. This phase lasts for a longer time because of the formation of the hotspot near the outlet of the channel. Finally, in the last phase, the heat generated is transferred downstream by convection. Here the solid phase temperature rises very quickly with high conversions and the heat transfer mechanism in this phase is governed by convection. It is difficult to quantitatively identify where these phases occur exactly, and hence it is conceded that these phases may overlap into each other during certain time instants. The solid temperature evolution profile along the length of the catalyst at different time instants for the optimum loading case is presented in **Figure 3.8**. It is clear from **Figure 3.8** that the evolution of the solid temperature along the length of the channel for the optimum loading case is different from that of the uniform case. Here only 3 distinct phases of operation can be identified, where in the first phase of operation the cold monolith is heated by the incoming hot fluid and heat transfer within the channel during this phase is only by convection. This is observed for a brief amount of time and the reactor shifts to the second phase with large concentration gradients within the washcoat in the radial directions, this is more distinct in the first zone of the channel where the thickness of the washcoat is high. It can be observed from **Figure 3.7** and **Figure 3.8** that in this phase at around 40 seconds, the solid phase temperature along the length of the channel in case of the optimum case is less than the uniform case even though the steady state conversion in the case of the optimum loading case is higher than that of the uniform case. The reason for this anomaly can be attributed to the fact that the evaluated solid phase temperature is a radially averaged quantity (look at the heat release due to exothermicity of the reaction (term 3) in equation 4). Due to washcoat diffusion limitation in the first zone of the channel because of high washcoat thickness, large concentration gradients are observed in the washcoat in the radial direction which lead to decrease in the reactant concentration in the radial direction towards the substrate leading to low rates which eventually lower the heat release term and hence the solid phase temperature.

In this phase the heat transfer occurs both by convection and solid phase conduction. This phase continues till the channel attains uniform temperature beyond which the reactor moves to the final phase where the presence of more catalytically active material at the inlet increases the heat produced by the exothermic reactions which results in the formation of the hot spot at the catalyst inlet. This heat released from the exothermic reactions propagate forward by both convection and conduction and this results in fast ignition of the entire catalyst and leads to higher conversions than the uniform distribution case.

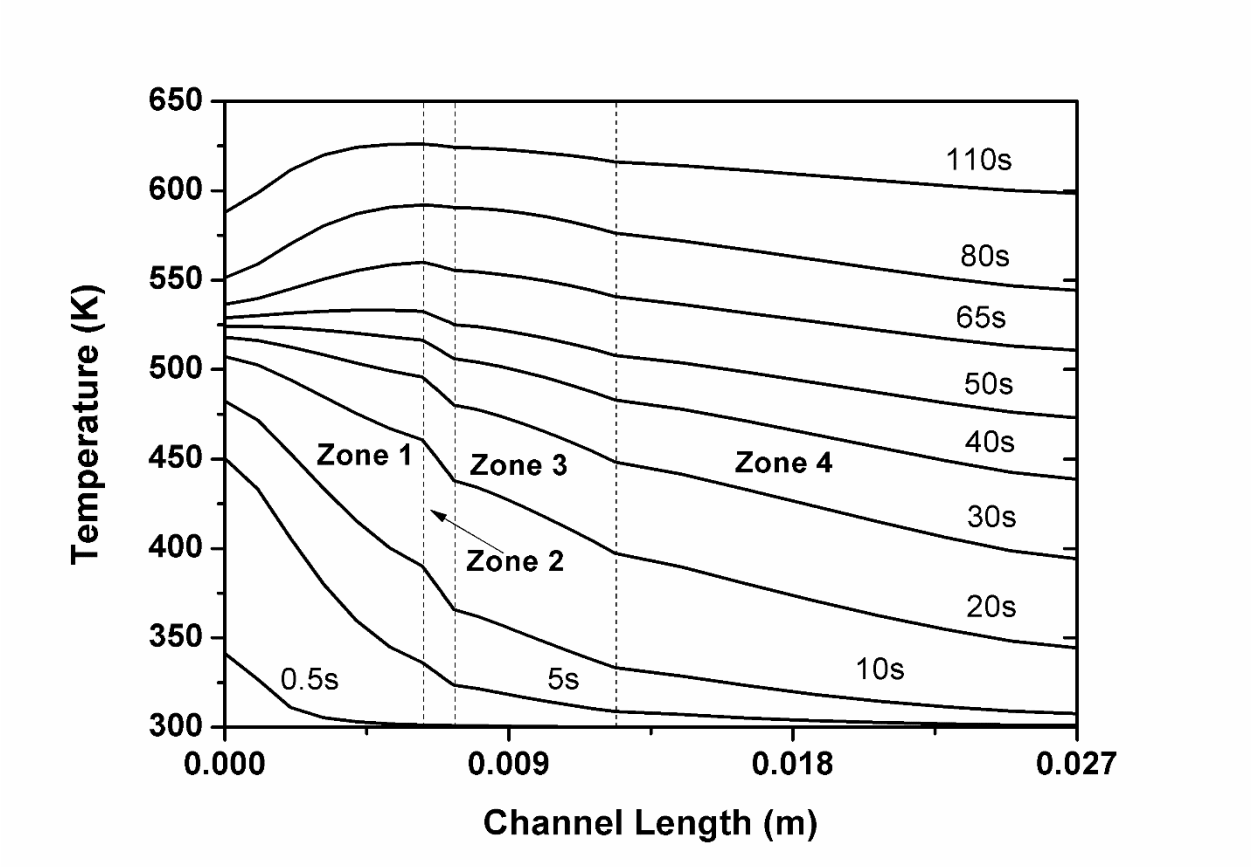

Figure 3.8. Evolution of optimum loading solid temperature profile for CO oxidation on Pt with 4 zones.

The better performance of the optimum loading profile compared to the uniform loading can also be explained by analyzing the CO self-inhibition near the channel entrance for the sub case with 4 zones. CO has been known to inhibit O_2 adsorption more effectively than surface oxygen inhibits the adsorption of CO. Especially, at low temperatures, CO_2 production is inhibited by adsorbed CO, with the CO2 production rate increasing at higher temperatures as the CO desorption rate increases. [96, 98]

The radial profile of the inhibition term (denominator in the rate expression (26)) along the washcoat thickness in the first zone is presented in **Figure 3.9** at 40, 50 & 60 s. Even though both the profiles yield similar performance for the first 30 seconds, the optimum profile shows better performance after this time. From the **Figure 3.9** it is clear that that the magnitude of inhibition is lesser in the optimum case than the uniform case resulting in higher rates ensuring higher CO desorption rate. This behavior can be attributed to the presence of thicker washcoat

in the first zone in the optimum profile (72.2 μm) when compared to the uniform profile (23.7 μm). The washcoat diffusion resistance leads to decreasing CO concentrations with increasing washcoat layer depth. This results in a decreasing CO inhibition of the CO rate as shown in **Figure 3.9**. Consequently, the CO conversion rate increases with increasing washcoat depth in this temperature range.

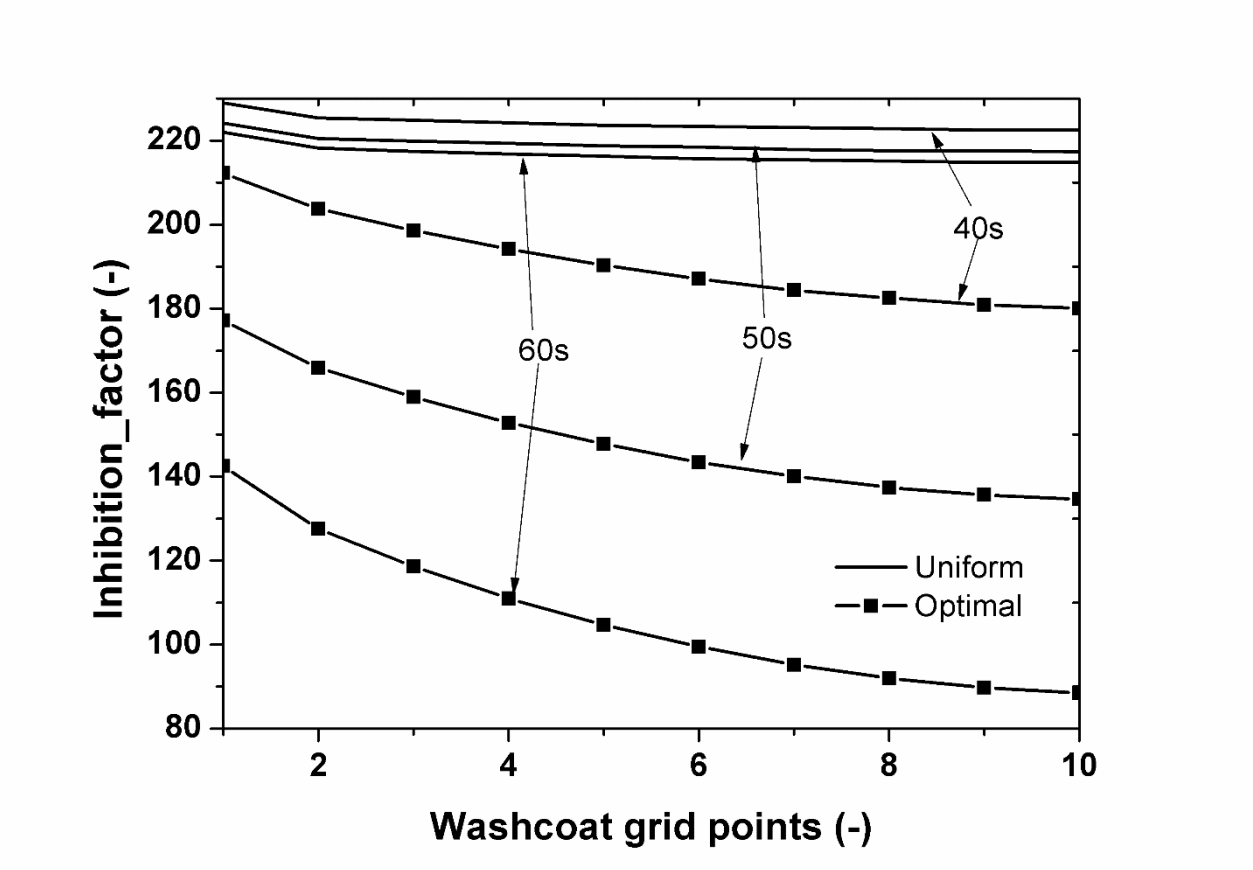

Figure 3.9. Inhibition factor evolution along the washcoat depth in zone 1.

3.4. Application 2: CH_4 oxidation on Pd/Al_2O_3

3.4.1. Background

The ability to use gases from various sources such as natural gas, biogas and synthetic methane (power–to–gas) promote lean burn gas engines among combustion engines. Further, these gas engines provide high efficiency while emitting little particulate matter (PM) and NO_x. This advantage can be attributed to a high H/C ratio in the gaseous fuel, homogeneous combustion, and low combustion temperature. However, these gas engines suffer from methane slip, i.e. the release of a small amount of unburned methane into the exhaust. Methane, the main component

of the gaseous fuel with high heat value is a strong greenhouse gas. Therefore, the emission regulations of methane are becoming more stringent making the removal of unburned methane crucial for future operation of gas engines in both transport (natural gas vehicles (NGV), trucks and ships) and stationary applications (power plants) [46, 99]. Among alkanes, methane is the kinetically least reactive molecule. In this respect, Pd based catalysts are generally considered to be most active catalysts for total oxidation of methane under lean conditions [99]. However several studies revealed that methane oxidation on Pd catalysts suffer from deactivation due to blocking of active sites by OH surface species during long term exposure of the catalyst to methane gas at low temperatures [99–101]. Taking into consideration the above facts, in the present case optimization of precious metal loading profile along the length of the channel is carried out to simultaneously maximize the steady state conversion of CH_4 and minimize the deactivation effects on CH_4 oxidation on Pd/Al_2O_3.

3.4.2. Kinetic modeling

Long term steady-state experiments were conducted over a fresh Pd catalyst of PGM loading 75 g/ft^3 over different constant inlet temperatures 475, 500 and 525 ℃ each for 11 h. In all the three cases first the temperature of the inlet gas is increased at a rate of 3 K/min from 200 ℃ until the temperature reaches 475, 500 and 525 ℃ after which it is held constant for the remaining time. The inlet gas mixture consists of only CH_4, H_2O, O_2, CO_2 and N_2. The time evolution of methane conversion for the three sub cases is presented in **Figure 3.10.** It can be seen that the conversion of methane reached a peak of about 95% in all the three sub cases. After which due to deactivation of the catalyst the CH_4 conversion drops to a steady value of 10%, 20% and 40%, respectively.

This deactivation is observed to be more predominant in the case of lower temperature. This strong deactivation observed can be attributed to the blocking of active sites by OH surface species [99]. First, the above experimental results are used to formulate the global adaptive kinetics with the 1D +1D model. The global rate expression incorporating the inhibition effect of H_2O based on Mars-van-Krevelen kinetics is considered to model the kinetics of CH_4 oxidation [101].

$$r_{\mathrm{CH_4}} = \frac{k_{\mathrm{oxi}} e^{\frac{-E_{\mathrm{oxi}}}{RT}} x_{\mathrm{CH_4}}}{\left(1 + k_{\mathrm{ads}} e^{\frac{-E_{\mathrm{ads}}}{RT}} x_{\mathrm{H_2O}}\right)} \tag{3.8}$$

In addition to the kinetic model, a deactivation model to account for the state of deactivation of the catalyst has been considered in the present case. The deactivation model used in the present studies is given below.

$$\frac{da}{dt} = -(a - a_s) k_{\mathrm{deac}} e^{\left(\frac{-E_{\mathrm{deac}}}{R}\left(\frac{1}{T_{\mathrm{ref}}} - \frac{1}{T}\right)\right)} \tag{3.9}$$

Table 3.3. Rate parameters for CH_4 oxidation on Pd/Al_2O_3

Parameter	value	unit
k_{oxi}	$2.9 \cdot 10^7$	mol/m² s
E_{oxi}	63892	J/mol
k_{ads}	50	[-]
E_{ads}	70917	J/mol
k_{deac}	$8 \cdot 10^{-5}$	[-]
E_{deac}	-18000	J/mol
a_s	0.05	[-]

The kinetic rate parameters like the pre-exponential factor k_{oxi}, activation energy E_{oxi}, CH_4 adsorption constant k_{ads} and heat of adsorption E_{ads} and the parameters in the deactivation model, the pre-exponential factor k_{deac} and the activation energy E_{deac} are calibrated by using the Levenberg-Marquardt algorithm to minimize the least squares residual between experimental data and simulations.

The derived values of the kinetic parameters are listed in **Table 3.3** and the model parameters used for the simulation are tabulated in **Table 3.4**. It can be seen from **Figure 3.10** that the 1D + 1D model with the evaluated parameters is able to predict the conversion behavior of CH_4

satisfactorily for all the three temperatures.

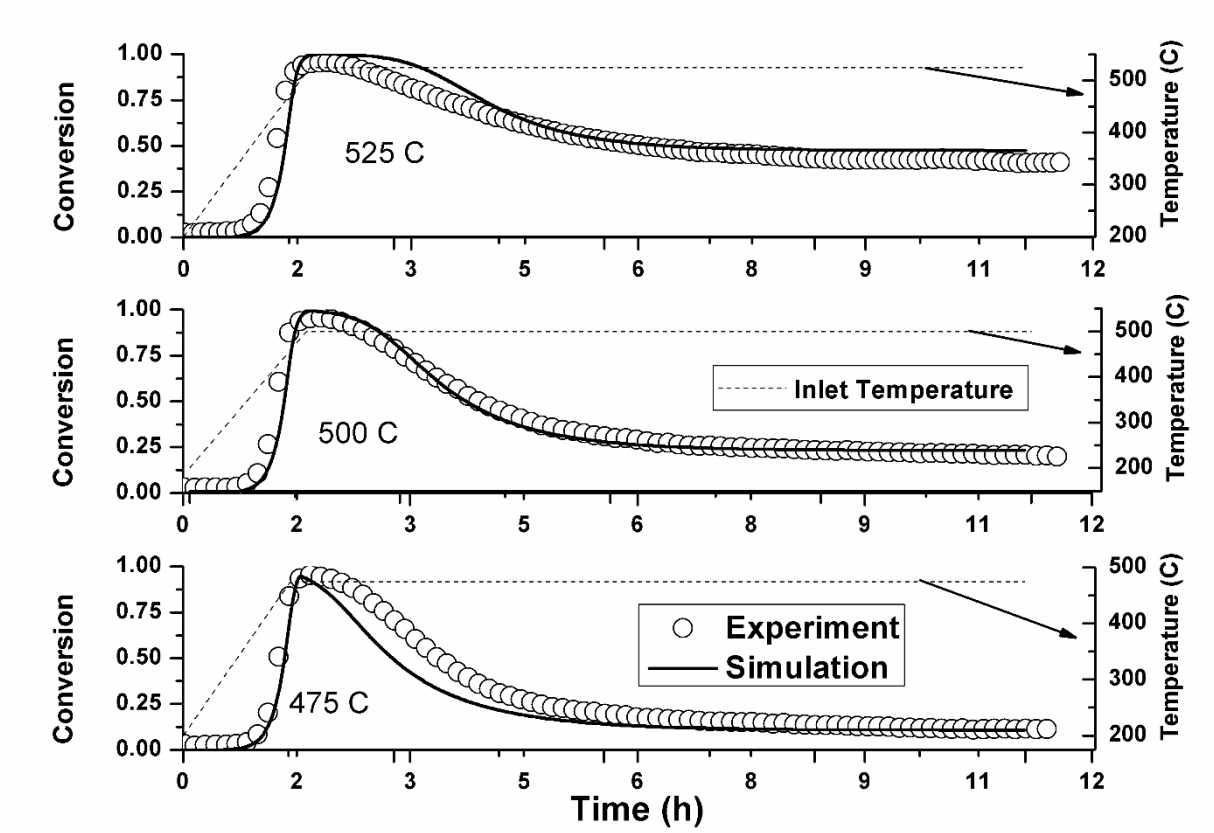

Figure 3.10. Comparison between experimental and simulations for CH_4 oxidation on Pd at different temperatures (Right axis for temperature).

Table 3.4. Model parameters used for the simulation of CH_4 on Pd/Al_2O_3

Parameter	value	unit
$\mathbf{PGM_{Tot}}$	75	g/ft^3
GHSV	30000	h^{-1}
CPSI	400	[-]
$\boldsymbol{\tau}$	3	[-]
$\boldsymbol{D_{ch}}$	0.0013	m
$\boldsymbol{\varepsilon_{wc}}$	0.41	[-]
$\boldsymbol{d_p}$	100	nm
L	0.03	m
$\boldsymbol{\delta_s}$	$1.016 \cdot 10^{-4}$	m
$\boldsymbol{\rho_{wc}}$	1200	kg/m^3
$\boldsymbol{\lambda}$	1.5	$W\ m^{-1}K^{-1}$
$\boldsymbol{c_w}$	1000	$J\ kg^{-1}K^{-1}$

3.4.3. Optimization problem formulation

Similar to the previous case, the optimization methodology described in **Section 2.4** is utilized to obtain the optimum zone-structured non-uniform loading profile for 3 sub cases where the catalyst is divided in to 2, 3 and 4 zones respectively. The optimum loading and length of each of these zones which will improve the steady state conversion of CH_4 are evaluated by optimization. The number of control parameters to be optimized in each of these sub cases would be 2*N* respectively, where *N* denotes the number of zones the catalyst is divided. One non-linear equality constraint which will hold the total amount of loading equivalent to fixed loading is incorporated. The optimization solution in each of these sub cases is compared with the uniform PGM loading case of 75 g/ft^3. The upper and lower bounds on the first *N* control parameters ($\boldsymbol{P}_{\mathbf{max}}$ & $\boldsymbol{P}_{\mathbf{min}}$) were chosen to be 1000 g/ft^3 and 10 g/ft^3 which corresponds to an $F_{cat/geo}$ value of 2260.1 and 0.64 and washcoat thickness of about 416.4 μm and 0.4 μm. The upper and lower bounds on the next *N* control parameters, i.e. the zone lengths ($\boldsymbol{L}_{\mathbf{max}}$ & $\boldsymbol{L}_{\mathbf{min}}$), are chosen to be *L-(N*-1*)* mm and 1 mm, so that the minimum length of any of the *N* zones would be at least 1 mm. The optimization problem is formulated for a typical fast light-off case for cold start emissions in a monolith, i.e., the catalyst is at 300 K at the start of the operation with CH_4 and other exhaust gases entering the monolith at 475, 500 & 525 °C respectively. Here in the first subcase with 2 zones the channel is divided in to 24 grid points in the axial direction, 27 grid points in the second subcase with 3 zones and 32 grid points in the third subcase with 4 zones. In all the subcases the washcoat is discretized in to 10 grid points radially. Similar to the previous case, the system is solved in a coupled approach leading to 960, 1080 and 1280 ode equations with 4, 6 and 8 control parameters respectively for each of the subcases, which are solved at once in time using the coupled approach.

3.4.4. Comparison between uniform loading and optimum loading profile

The results from the optimization of zone-structured non-uniform PGM loading profile are presented in **Figure 3.11**. It can be observed from **Figure 3.11** that for all the three sub cases with different number of zones the optimum loading profile has more active catalytic substance in zone 1 near the inlet of the channel than the other zones.

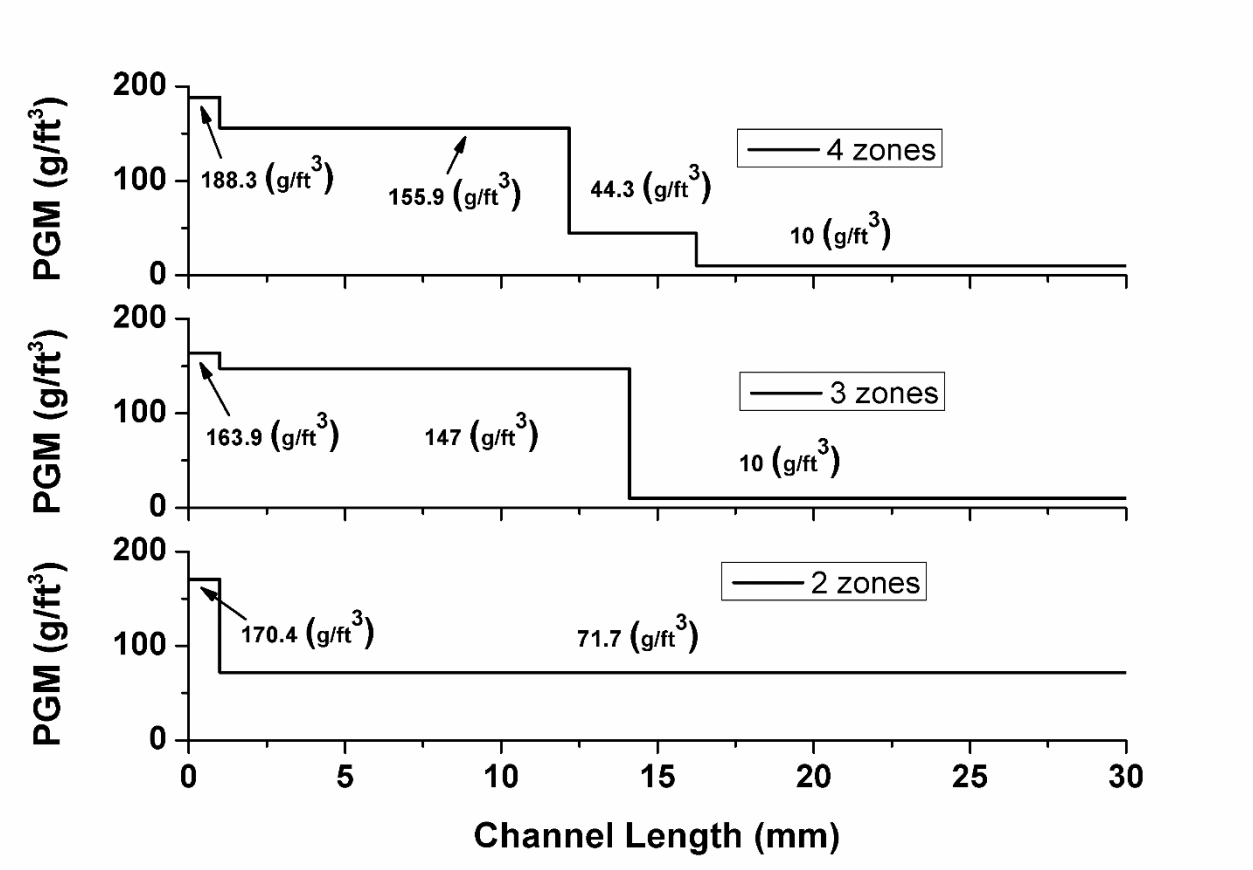

Figure 3.11. Optimum loading profile for CH_4 oxidation on Pd.

Here the length of the first zone is much shorter in all the 3 subcases when compared with the previous case result.

Figure 3.12 describes the comparison of CH_4 conversion versus time between the uniform loading and optimum loading profile for all the 3 sub cases. It can be inferred that with the optimum loading profile not only the light-off temperature decreased but also improved the steady conversion of CH_4. In case of the optimum loading profile, the decrease in light-off temperature can be attributed to the presence of more active substance at the inlet resulting in higher heat release due to the exothermicity of the reaction. Also the effect of deactivation is not observed with the optimal loading profile. The better performance exhibited by the optimal loading profile over uniform loading profile can explained by comparing the solid temperature profile evolution in both the cases.

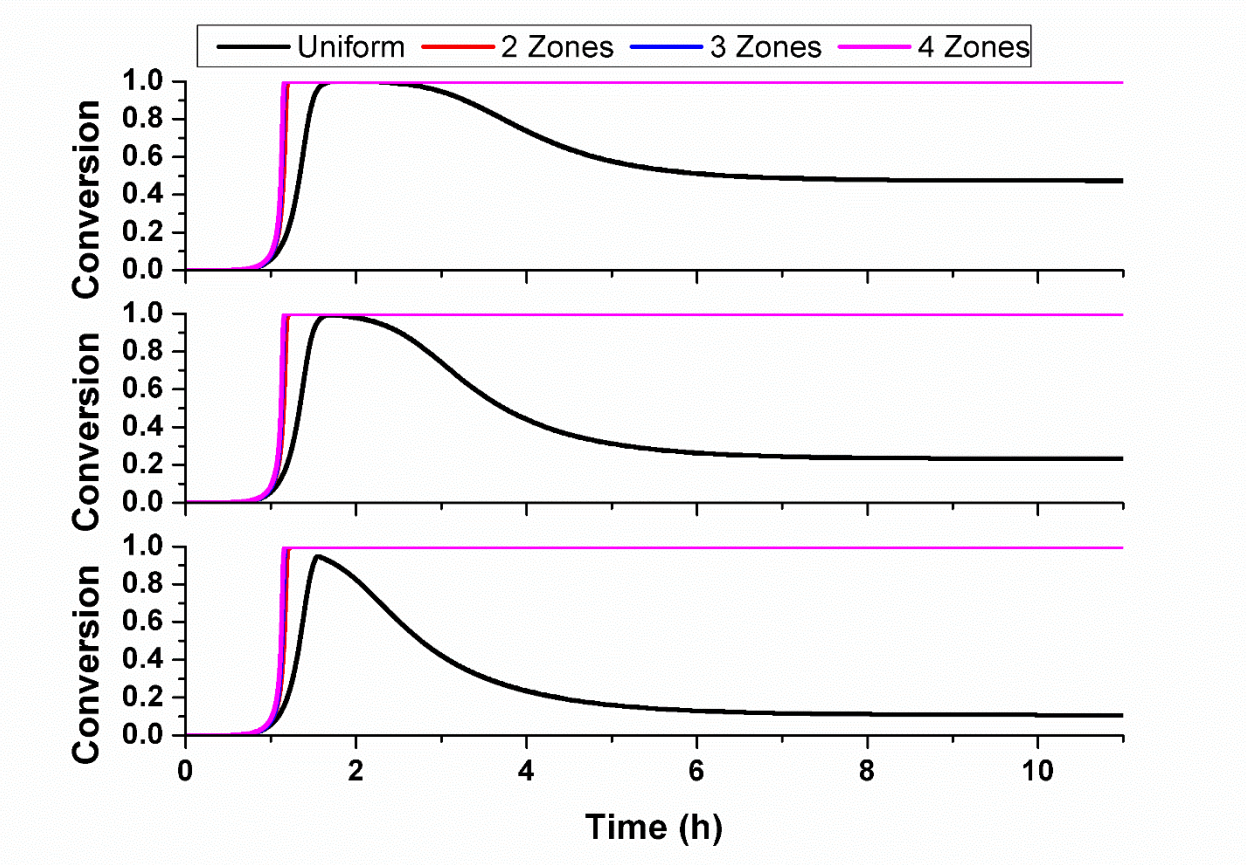

Figure 3.12. Comparison between uniform and optimum loading profile performance for CH_4 oxidation on Pd.

Figure 3.13 depicts the time evolution of solid temperature for the sub case 1 with uniform PGM loading where the inlet temperature is increased at 3K/min to 475 °C and thereafter held constant.

The analogy used in the **Section 3.5** can be employed here directly in this case to understand the temperature evolution and its impact on performance even though a slight difference in the operating conditions exists. In the previous application case the catalyst is at ambient temperature initially and inlet gas temperature was fixed at 523 K resulting in faster ignition of the catalyst.

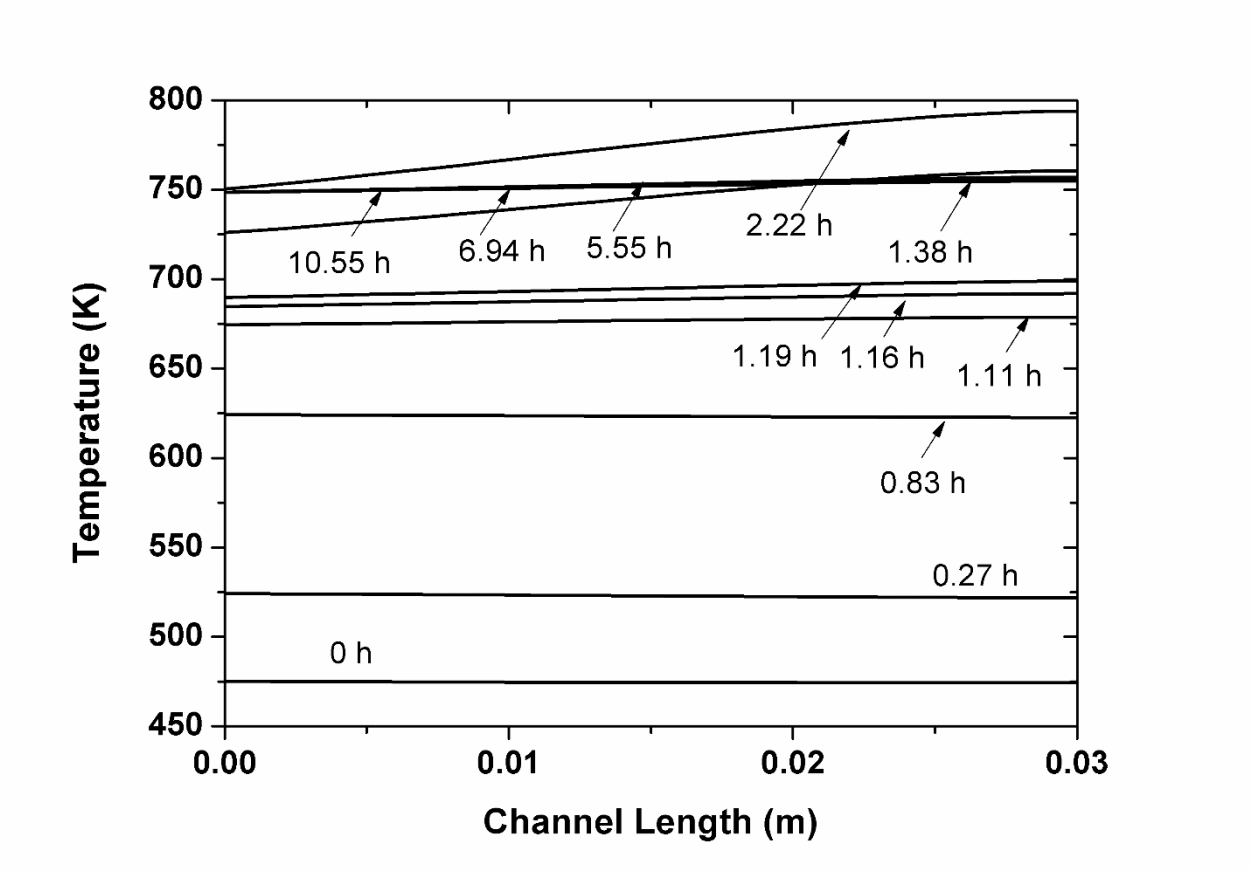

Figure 3.13. Solid temperature evolution for CH_4 oxidation on Pd with uniform loading for the case with 475 °C.

In the present application case the inlet temperature is increased with a heat ramp 3K/min resulting in slower ignition of the catalyst and much slower temperature time scale leading to better uniform temperature distribution along the length of the channel. This is corroborated in **Figure 3.13** that the channel operates at constant temperature along the length till the light off. Here the reactor operates in the second phase. Following that, the reactor transits to phase three where a hot spot is formed towards the end of the channel. This leads to the propagation of the heat front backwards against the direction of the flow due to solid phase conduction similar to the case presented in **Section 3.5**. Following this due to deactivation the temperature starts to decrease from the end of the channel affecting the conversion.

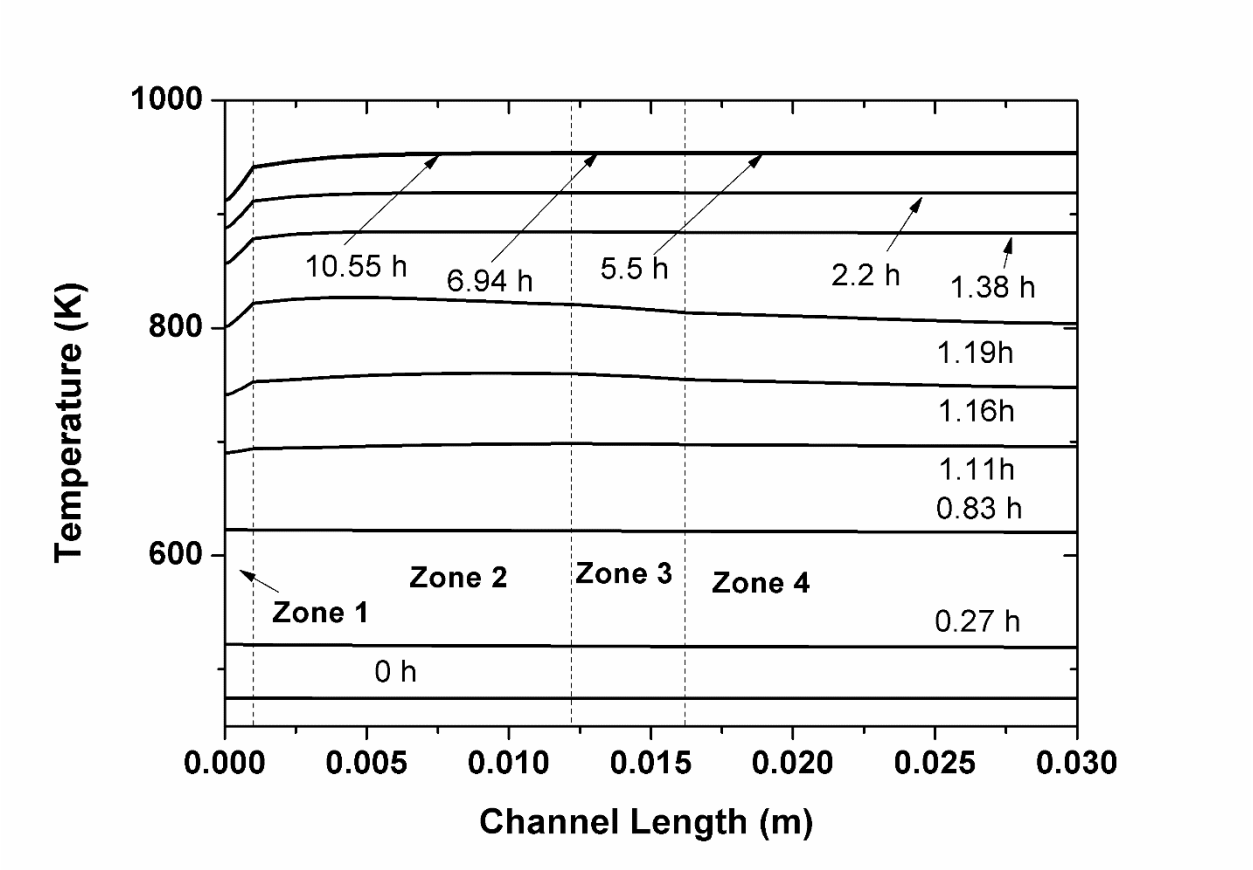

Figure 3.14. Solid temperature evolution for CH_4 oxidation on Pd with optimum loading for the case with 475 °C with 4 zones.

The solid temperature evolution with time along the length of the channel for the optimum loading case is presented in **Figure 3.14**. In this case it can be seen that the evolution of the temperature profile is similar to the case of uniform loading until the end of the second phase after which due to the presence of high active amount of PGM at the inlet results in rapid increase of temperature leading to the formation of a hot spot near the inlet. This produced heat propagates forward due to both convection and conduction quickly igniting the channel and transit quickly to the third phase. Here it can be observed that the temperature in zone 2 is much higher than that in zone 1 even though the PGM amount in zone 1 is higher than in zone 2. This is because of high diffusion limitations in the zone 1 which would again reduce the thickness averaged solid temperature leading to lower temperature. But one can observe that not only did the overall conversion improve but also the effect of deactivation is not observed due to prevalence high temperatures throughout the channel when compared to the uniform loading case. The reason for the disappearance of deactivation effects can be attributed to the prevailing high temperatures in the channel which effectively avoided the OH ions from blocking the active sites hence diminishing the effect.

4. NH_3 dosing Optimization

Evolution of fuel efficient diesel engines as the popular choice for transport applications (heavy-duty and passenger cars) inevitably puts the inherent challenging issue of emissions to the forefront. Particularly because of the lean environment in diesel engine, the focus is mainly on NO_x (NO and NO_2) and exhaust gas Particulate Matters (PM). One of the major species detected in the diesel exhaust gas is nitrogen oxide (NO), which is proved to be harmful for human health. Consequently, the global emission standards for diesel engines have become much more stringent in the past few years, resulting in the development of an efficient after-treatment technology to meet the emission requirements. Selective catalytic reduction (SCR) of NO_x with NH_3 has evolved to be promising technology in the recent years to address the NO_x emission [102]. In this process, NH_3 which is the reducing agent is generated onboard through the decomposition of urea, which is stored in form of urea-water solution with urea concentration of 32.5% by weight [10, 11, 103, 104]. The urea decomposition can be summarized by the reactions R1.4 and R1.5.

Extensive experimental and kinetic studies of NH_3 - SCR with wide range of catalysts have been carried out and are reported in the literature [13–17, 105, 106]. Among several catalytic formulations vanadia-based, Cu and Fe zeolite based catalysts have gained prominence owing to their superior low temperature performance and thermal durability [104]. In addition to the rigorous steady-state and transient experimental investigations on these catalysts, a wide range of global and detailed mechanisms have been reported [12, 13, 15–19, 105, 107, 108]. Most of the kinetic models have taken into consideration all the important reaction steps like NH_3 adsorption, desorption, standard SCR, fast SCR and NO oxidation [17, 20]. The majority of the global mechanisms are normally formulated by taking into consideration one surface species, i.e. adsorbed NH_3. The intrinsic kinetic model for Fe zeolite catalysts presented by [108] considered N_2O reactivity in addition to the other reactions. Olsson and coworkers also reported models with multiple surface sites on zeolite-based catalysts [18, 19].

The reported mechanisms have been developed and validated over a wide range of operating conditions especially over varying NH_3/NO_x ratios. Most of these developed mechanisms are employed to simulate real-world driving cycles and to optimize the other components of the exhaust gas system. In a typical transient driving cycle the inputs to the system vary rapidly over a wide range of temperatures and NH_3/NO_x ratios. It is observed that at high temperatures

the adsorption capacity of these catalysts decreases strongly. Therefore, high NH_3/NO_x ratio, i.e. high NH_3 dosing, might lead to significant NH_3 excursions affecting the overall efficiency of the process [102, 109].

This presents with a need to optimize the NH_3 dosing effectively during a driving cycle. Very few studies have been dedicated so far to optimize the NH_3 dosing for typical transient driving cycles. Firstly, a simple methodology to optimize the parameters of the NH_3 dosing controller is proposed by Schuler et al (2009). Faghihi and Shamekhi (2010) formulated a neural network model for the SCR catalyst and used a multi objective genetic algorithm to optimize ammonia dosing. The authors have used heuristic based methods (derivative free) like neural network to carry out the optimization. An open-loop control strategy that controls the amount of ammonia added at each discrete time instant for WHTC driving cycle is presented by Hauptmann et al (2011). Later, a control strategy which would optimize the parameters of a lookup table which in turn optimizes the NH_3 dosing for a WHTC driving cycle and ensures high conversion and lowers NH_3 slip is presented by Opitz et al (2015).

Most of the studies carried out in the literature considered 1D isothermal models to simulate the process [17, 43, 105]. In a typical 1D model, the diffusion effects are lumped into the kinetic parameters and radial variations are neglected. Metkar et al (2013, 2012a, 2012b, 2011) have used a more detailed 1D + 1D isothermal model which solves for reaction-diffusion in the radial direction across the washcoat to obtain the kinetics and reported that for Fe and Cu catalysts, diffusion limitations are observed at high temperatures. Even though the 1D + 1D model [40, 42] is a robust predictive tool, the total number of equations to be solved due to inclusion of the reaction-diffusion equation at each axial position of the channel makes it computationally demanding and not viable for optimization studies. Recently, strategies like internal mass transfer concept [34, 41, 112, 113] and asymptotic solution of washcoat diffusion [114] have been proposed, which are proved to be an effective substitute for the detailed reaction-diffusion equations in predicting washcoat diffusion for single and dual-layered catalysts. These methods require just the evaluation of a standard 1D model to account for washcoat diffusion effects. Since the objective of this work is not development of these methods but application of one of them, the readers are directed to the literature [34, 41, 112–114] for detailed understanding.

In this chapter, a model-based numerical optimization approach to find the optimal NH_3 dosing for a copper-chabazite (Cu-cha) SCR catalyst for an entire driving cycle. The key components

for this optimization framework apart from a computationally efficient reactor model include a descriptive mathematical optimization formulation and a robust numerical solution scheme.

In this work, a systematic methodology to optimize ammonia dosing for a typical transient driving cycle using numerical optimization algorithms. The **Section 4.1** describes the different reactor models and the kinetics used to simulate SCR process. The **Section 4.2** discusses the general optimization formulation and its solution strategy based on the OCFE method. The description of the strategy used in formulating the optimization problem to optimize the NH_3 dosing for the transient driving cycle is discussed in the next **Section 4.3**. Finally, the results of the optimization and the efficiency of the methodology are discussed.

4.1. Reactor modeling

4.1.1. 1D + 1D Reactor model

A two-dimensional two-phase 1D+1D model presented in **Section 2.1.1** is used in the present study. In the present chapter, only the isothermal model is considered which takes in to account only the equations (2.4) and (2.6). The boundary conditions (2.8) and (2.9) are considered.

The adsorbed ammonia is evaluated by

$$\frac{d\Theta_{\mathrm{NH_3}}}{dt} = \frac{S_{\mathrm{NH_3}}}{\Omega_{\mathrm{NH_3}}} \tag{4.1}$$

where $\Omega_{\mathrm{NH_3}}$ is the total adsorption capacity of the catalyst.

4.1.2. 1D reactor model

A two phase 1-D isothermal model of a single monolith channel presented **Section 2.1.2** with slight modification is used to simulate the process. The washcoat diffusion effects are not lumped in the kinetic parameters, instead the overall mass transfer coefficients are used which inherently consider these effects. The bulk gas species equation is given by

$$\frac{\partial \boldsymbol{X_f}}{\partial t} = -u\frac{\partial \boldsymbol{X_f}}{\partial z} - \frac{4\boldsymbol{k_{mo}}(\boldsymbol{X_s} - \boldsymbol{X_f})}{d_h} \tag{4.2}$$

The species conservation equations in the solid phase are listed below.

$$\varepsilon_{\mathrm{wc}} \frac{\partial \boldsymbol{X_s}}{\partial t} = \frac{\boldsymbol{k_{mo}}(\boldsymbol{X_s} - \boldsymbol{X_f})}{\delta_{\mathrm{wc}}} + \frac{\boldsymbol{S}}{c_{\mathrm{T}}} \tag{4.3}$$

Where δ_{wc} is the effective washcoat length for a given geometry.

The time evolution of adsorbed ammonia species is evaluated by

$$\frac{d\theta_{\mathrm{NH_3}}}{dt} = \frac{S_{\mathrm{NH_3}}}{\Omega_{\mathrm{NH_3}}} \tag{4.4}$$

The following boundary conditions were assumed

At the inlet at $z = 0$, Dirichlet boundary conditions were applied.

$$\boldsymbol{X_f}(t, z) = \boldsymbol{X_{f,0}} \quad \text{at } t = 0 \tag{4.5}$$

$$\boldsymbol{X_f}(t, 0) = \boldsymbol{X_{f,t}} \quad \forall \text{ t} \tag{4.6}$$

Evaluation of Internal Mass transfer coefficients

The effect of washcoat diffusion limitations becomes significant especially at higher temperatures due to large concentration gradients within the washcoat. The classical approach to account for these limitations is to evaluate the reaction-diffusion equation. Even though straight forward, it induces additional computational effort. The approach of internal mass transfer developed by Balakotaiah and co-workers [112, 113] provides a viable alternative within the framework of a 1D model. This approach approximates the effect of washcoat diffusion within the given reaction-diffusion problem with the assumption that rate follows first order kinetics.

The method proceeds by the evaluation of internal Sherwood number with respect to the value of the Thiele modulus by using a proposed correlation expression (4.7), followed by evaluation

of the internal mass transfer coefficients from the internal Sherwood number by equation (4.8). Thiele modulus (φ) is evaluated by (4.9)

$$Sh_{\text{int}} = Sh_{\text{int},\infty} + \frac{\Lambda\varphi^2}{1+\Lambda\varphi} \tag{4.7}$$

$$k_{\text{mi}} = \frac{Sh_{\text{int}} D_{\text{eff}}}{\delta_{\text{wc}}} \tag{4.8}$$

$$\varphi^2 = \frac{k_0 {\delta_{\text{wc}}}^2}{D_{\text{eff}}} \tag{4.9}$$

For the case of square channel with rounded square flow area, the internal asymptotic Sherwood value ($Sh_{\text{int},\infty}$) and the constant (Λ) used in this simulation are tabulated in **Table 4.3**. Once obtained the evaluated internal mass transfer coefficient and the external mass transfer coefficient are used to evaluate the overall mass transfer coefficient for each of the species according to (4.10) and is used in Equations (4.2) and (4.3).

$$\frac{1}{k_{\text{mo}}} = \frac{1}{k_{\text{me}}} + \frac{1}{k_{\text{mi}}} \tag{4.10}$$

4.1.3. Kinetic modeling

For the purpose of the current study, the global kinetic model for the NO_x reduction reactions occurring during NH_3-SCR on Cu-cha catalyst presented in [13–16] is used. The kinetic model has 8 global reaction steps taking into consideration all the major steps occurring in NH_3-SCR. The reactions considered are the NH_3 adsorption and desorption step with one surface species representing adsorbed NH_3. The other reactions considered are a global reaction for ammonia oxidation (R4.2), a global NO oxidation reaction (R4.3) between NO and O_2 is also included. The NO oxidation is a reversible reaction with the reverse reaction (NO_2 decomposition) becoming predominant at higher temperature (>350°C). The standard SCR reaction (R4.4) between adsorbed NH_3 and gas phase NO and O_2, the fast SCR reaction (R4.5) involves the reduction of equimolar amounts of gas phase NO and NO_2 by NH_3 adsorbed on the catalyst and the NO_2 SCR reaction (R4.6) is described by the reduction of gas phase NO_2 by adsorbed NH_3 species. In addition to the above 6 reactions, ammonium nitrate (NH_4NO_3) producing reaction

between equimolar NO_2 and adsorbed NH_3 (R4.7) and the ammonia decomposition in to N_2O reaction (R4.8) are considered. As stated above the kinetic parameters for the reaction mechanism are obtained from [13]. The rate expressions and the values of the kinetic parameters are tabulated in Table 4.1 and Table 4.2.

Table 4.1. Reactions and rate expressions used for Cu-cha catalyst

No	Reaction	Rate expression
R4.1	$NH_3 + S \leftrightarrow NH_3S$	$k_{1f}X_{NH_3}\theta_v - k_{1b}\theta_{NH_3}$
R4.2	$2\,NH_3S + 1.5\,O_2 \rightarrow N_2 + 3\,H_2O + 2\,S$	$k_{2f}X_{O_2}\theta_{NH_3}$
R4.3	$NO + 0.5\,O_2 \leftrightarrow NO_2$	$k_{3f}X_{O_2}^{0.5}X_{NO} - k_{3b}X_{NO_2}$
R4.4	$4\,NH_3S + 4\,NO + O_2 \rightarrow 4\,N_2 + 6\,H_2O + 4\,S$	$k_{4f}X_{NO}\theta_{NH_3}$
R4.5	$2\,NH_3S + NO + NO_2 \rightarrow 2\,N_2 + 3\,H_2O + 2\,S$	$k_{5f}X_{NO}X_{NO_2}\theta_{NH_3}$
R4.6	$4\,NH_3S + 3\,NO_2 \rightarrow 3.5\,N_2 + 6\,H_2O + 4\,S$	$k_{6f}X_{NO_2}\theta_{NH_3}$
R4.7	$2\,NH_3S + 2\,NO_2 \rightarrow N_2 + NH_4NO_3 + H_2O + 2\,S$	$k_{7f}X_{NO_2}\theta_{NH_3}$
R4.8	$NH_4NO_3 \rightarrow N_2O + 2\,H_2O$	$k_{8f}X_{NH_4NO_3}$

Here k_{if} and k_{ib} represent the forward and reverse rate constants of reaction step *i*, respectively and are defined using the Arrhenius expressions given by

$$k_{if} = A_{if} \cdot e^{\frac{-E_{if}}{RT}} \tag{4.11}$$

$$k_{ib} = A_{ib} \cdot e^{\frac{-E_{ib}}{RT}} \tag{4.12}$$

where A_{if} and A_{ib} are pre-exponential factors and E_{if} and E_{ib} are activation energies of the forward and reverse reaction step *i*, respectively.

Table 4.2. Values of the kinetic parameters for Cu-chabazite catalyst.

Parameter	Value	Parameter	Value
	$\boldsymbol{mol/m^3\,s}$		$\boldsymbol{kJ/mol}$
$\boldsymbol{A_{1f}}$	6.68×10^{7}	E_{1f}	0
$\boldsymbol{A_{1b}}$	4.0×10^{15}	E_{1b}	$145.9\left(1-0.97\theta_{NH_3}\right)$
$\boldsymbol{A_{2f}}$	5.56×10^{16}	E_{2f}	178.9
$\boldsymbol{A_{3f}}$	5.1×10^{7}	E_{3f}	56
$\boldsymbol{A_{4f}}$	7.08×10^{13}	E_{4f}	89.1
$\boldsymbol{A_{5f}}$	1×10^{18}	E_{5f}	77.1
$\boldsymbol{A_{6f}}$	1.96×10^{17}	E_{6f}	136.3
$\boldsymbol{A_{7f}}$	2.28×10^{8}	E_{7f}	43
$\boldsymbol{A_{8f}}$	1.25×10^{8}	E_{8f}	41.5

4.1.4. Grey-box model

The 1D reactor model with overall mass transfer coefficients presented in the previous section assists in significant model reduction from the detailed 1D+1D model without of loss of reasonable accuracy. This model reduction will reduce the computation effort significantly. This model can be used as a substitute to the 1D+1D model to perform parameter estimation and model optimization to optimize the design of the catalysts. Even though the model is simple with relatively small number of state variables the model can be further reduced by neglecting the accumulation terms ($\partial/\partial t$) in equations (4.2) and (4.3) to obtain

$$u\frac{\partial \boldsymbol{X_f}}{\partial z}+\frac{4\boldsymbol{k_{mo}}(\boldsymbol{X_s}-\boldsymbol{X_f})}{d_h}=0 \tag{4.13}$$

$$\frac{\boldsymbol{k_{mo}}(\boldsymbol{X_s}-\boldsymbol{X_f})}{\delta_{wc}}+\frac{\boldsymbol{S}}{c_T}=0 \tag{4.14}$$

$$\frac{d\theta_{NH_3}}{dt}=\frac{S_{NH_3}}{\Omega_{NH_3}} \tag{4.15}$$

The obtained equations can be solved in DAE mode assuming that the dynamics of all the species is much faster than that of the ammonia storage species, leading to a quasi steady-state approximation. Further expanding the rate of production or consumption term in equation (4.14)

in terms of rate constants, species concentration and stoichiometry, and solving the equations for NO, NO_2 and NH_3 leads to simple algebraic equations (4.16) to (4.21). These algebraic equations are decoupled from the solver and are simultaneously solved with the storage species with negligible computational effort [115]. In addition to the incoming species concentration, only the knowledge of the storage species present state is desired to solve the model. In order to capture axial gradients, CSTRs in series or cascading approach can be used, where *N* number of these blocks can be placed in series and the outlet from one block is introduced as inlet to the next block. For more information on the model the reader are diverted to Gundlapally et al [115]. This methodology to reduce the model has presented significant benefits in formulating the optimization problem as will be described in the upcoming sections. The step-by-step procedure to derive the grey-box model is described below. The gas phase NO species balance equation (4.13) can be written as equation (4.16) and (4.17)

$$\frac{u}{\Delta z}\left(X_{\mathrm{f,NO}} - X_{\mathrm{f,NO}}^{\mathrm{in}}\right) = \frac{-4k_{\mathrm{mo,NO}}}{\varepsilon_{\mathrm{g}}}\left(X_{\mathrm{f,NO}} - X_{\mathrm{s,NO}}\right) \tag{4.16}$$

$$P_{\mathrm{NO}}\left(X_{\mathrm{f,NO}} - X_{\mathrm{f,NO}}^{\mathrm{in}}\right) = -\left(X_{\mathrm{f,NO}} - X_{\mathrm{s,NO}}\right) \tag{4.17}$$

And upon further simplification, outlet composition of NO in gas phase can be written as a function of inlet NO composition and NO composition in the solid phase.

$$X_{\mathrm{f,NO}} = \frac{PP_{\mathrm{NO}} \cdot X_{\mathrm{f,NO}}^{\mathrm{in}} + X_{\mathrm{s,NO}}}{1 + PP_{\mathrm{NO}}} \tag{4.18}$$

Analogously similar equations (A.4) and (A.5) can be obtained for NO_2 and NH_3

$$X_{\mathrm{f,NO_2}} = \frac{PP_{\mathrm{NO_2}} \cdot X_{\mathrm{NO_2}}^{\mathrm{in}} + X_{\mathrm{s,NO_2}}}{1 + PP_{\mathrm{NO_2}}} \tag{4.19}$$

$$X_{\mathrm{f,NH_3}} = \frac{PP_{\mathrm{NH_3}} \cdot X_{\mathrm{NH_3}}^{\mathrm{in}} + X_{\mathrm{s,NH_3}}}{1 + PP_{\mathrm{NH_3}}} \tag{4.20}$$

From the species conservation equation (4.14) in the solid phase for NO, NO_2 and NH_3 can be expressed as equation (4.21), (4.22) and (4.23).

$$\frac{-c_{\mathrm{T}} \cdot k_{\mathrm{mo,NO}}}{\delta_{\mathrm{wc}}}\left(X_{\mathrm{f,NO}} - X_{\mathrm{s,NO}}\right) = -k_{3f} \cdot X_{\mathrm{s},O_2}^{0.5} \cdot X_{\mathrm{s,NO}} - 4k_{4f} \cdot X_{\mathrm{s,NO}} \cdot \theta$$

$$-k_{5f} \cdot X_{\mathrm{s,NO}} \cdot X_{\mathrm{s},NO_2} \cdot \theta + k_{3b} \cdot X_{\mathrm{s},NO_2} \quad (4.21)$$

$$\frac{-c_{\mathrm{T}} \cdot k_{\mathrm{mo},NO_2}}{\delta_{\mathrm{wc}}}\left(X_{\mathrm{f},NO_2} - X_{\mathrm{s},NO_2}\right) = k_{3f} \cdot X_{s,O_2}^{0.5} \cdot X_{\mathrm{s,NO}} - k_{3b} \cdot X_{\mathrm{s},NO_2}$$

$$-4k_{4f} \cdot X_{\mathrm{s,NO}} \cdot \theta - k_{5f} \cdot X_{\mathrm{s,NO}} \cdot X_{\mathrm{s},NO_2} \cdot \theta - 3k_{6f} \cdot X_{\mathrm{s},NO_2} \cdot \theta \quad (4.22)$$

$$\frac{-c_{\mathrm{T}} \cdot k_{\mathrm{mo},NH_3}}{\delta_{\mathrm{wc}}}\left(X_{\mathrm{f},NH_3} - X_{\mathrm{s},NH_3}\right) = -k_{1f} \cdot X_{\mathrm{s},NH_3} \cdot (1-\theta) + k_{1b} \cdot \theta \quad (4.23)$$

Substituting (4.18) in (4.21) and upon simplification we obtain equation (4.24), Similarly for NO_2 substituting (4.18) & (4.19) in (4.22) we obtain equation (4.25) and by following the same procedure and substituting (4.20) in (4.23) we obtain (4.26).

$$X_{\mathrm{s},NH_3} = \frac{SS_{NH_3} \cdot X_{\mathrm{f},NH_3}^{\mathrm{in}} + k_{\mathrm{b},1} \cdot \theta}{PP_{NH_3} + k_{\mathrm{b},1} \cdot (1-\theta)} \quad (4.24)$$

$$X_{\mathrm{s},NO_2} = \frac{-b + \sqrt{b^2 - 4ac}}{2a} \quad (4.25)$$

$$X_{\mathrm{s,NO}} = \frac{SS_{\mathrm{NO}} \cdot X_{\mathrm{f,NO}}^{\mathrm{in}} + k_{\mathrm{b},3} \cdot X_{\mathrm{s},NO_2}}{SS_{\mathrm{NO}} + k_{\mathrm{f},3} \cdot X_{\mathrm{s},O_2}^{0.5} + 4k_{\mathrm{f},4} \cdot \theta + k_{\mathrm{f},5} \cdot \theta \cdot X_{\mathrm{s},NO_2}} \quad (4.26)$$

$$\Omega_{NH_3} \frac{d\theta}{dt} = R_1 - 2R_2 - 4R_4 - 2R_5 - 4R_6 \quad (4.27)$$

where

$$PP_{\mathrm{NO}} = \frac{u \cdot d_{\mathrm{h}}}{4 \cdot \Delta z \cdot k_{\mathrm{mo,NO}}}, \qquad PP_{\mathrm{NO_2}} = \frac{u \cdot d_{\mathrm{h}}}{4 \cdot \Delta z \cdot k_{\mathrm{mo,NO_2}}}, \qquad PP_{\mathrm{NH_3}} = \frac{u \cdot d_{\mathrm{h}}}{4 \cdot \Delta z \cdot k_{\mathrm{mo,NH_3}}}$$

$$SS_{\mathrm{NO}} = \frac{C_{\mathrm{T}} \cdot k_{\mathrm{mo,NO}} \cdot PP_{\mathrm{NO}}}{\delta_{\mathrm{wc}}(1+PP_{\mathrm{NO}})}, \qquad SS_{\mathrm{NO_2}} = \frac{C_{\mathrm{T}} \cdot k_{\mathrm{mo,NO_2}} \cdot PP_{\mathrm{NO_2}}}{\delta_{\mathrm{wc}}(1+PP_{\mathrm{NO_2}})}, \qquad SS_{\mathrm{NH_3}} = \frac{C_{\mathrm{T}} \cdot k_{\mathrm{mo,NH_3}} \cdot PP_{\mathrm{NH_3}}}{\delta_{\mathrm{wc}}(1+PP_{\mathrm{NH_3}})}$$

$$a = SS_{\mathrm{NO_2}} \cdot k_{\mathrm{f},5} \cdot \theta + 2k_{\mathrm{b},3} \cdot k_{\mathrm{f},5} \cdot \theta + 3 \cdot k_{\mathrm{f},5} \cdot k_{\mathrm{f},6} \cdot \theta^2$$

$$b = k_{\mathrm{f},5} \cdot \theta \cdot \left(SS_{\mathrm{NO}} \cdot X_{\mathrm{f,NO}}^{\mathrm{in}} - SS_{\mathrm{NO_2}} \cdot X_{\mathrm{f,NO_2}}^{\mathrm{in}}\right) - k_{\mathrm{f},3} \cdot k_{\mathrm{b},3} \cdot X_{\mathrm{s,O_2}}^{0.5}$$

$$+\left(SS_{\mathrm{NO_2}} + k_{\mathrm{b},3} + 3k_{\mathrm{f},6} \cdot \theta\right)\left(SS_{\mathrm{NO}} + k_{\mathrm{f},3} \cdot X_{\mathrm{s,O_2}}^{0.5} + 4k_{\mathrm{f},4} \cdot \theta\right)$$

$$c = -SS_{\mathrm{NO_2}} \cdot X_{\mathrm{f,NO_2}}^{\mathrm{in}}\left(SS_{\mathrm{NO}} + k_{\mathrm{f},3} \cdot X_{\mathrm{s,O_2}}^{0.5} + 4k_{\mathrm{f},4} \cdot \theta\right) - SS_{\mathrm{NO}} \cdot k_{\mathrm{f},3} \cdot X_{\mathrm{s,O_2}}^{0.5} X_{\mathrm{f,NO}}^{\mathrm{in}}$$

Equations 4.18-4.20 and Equations 4.24-4.27 represent the reduced model and can be easily solved.

4.2. Results and discussion

4.2.1. Model validation

The 1D+1D model presented in **Section 2.1** is used along with SCR reaction kinetics presented in **Table 4.1 & 4.2** to simulate the experimental data presented in Metkar et al [13]. All the 8 reaction steps for Cu-cha catalyst were considered, which also include the side reactions (R4.7 & R4.8) for the formation of NH_4NO_3 and N_2O. The model parameters used for simulation are tabulated in **Table 4.3**.

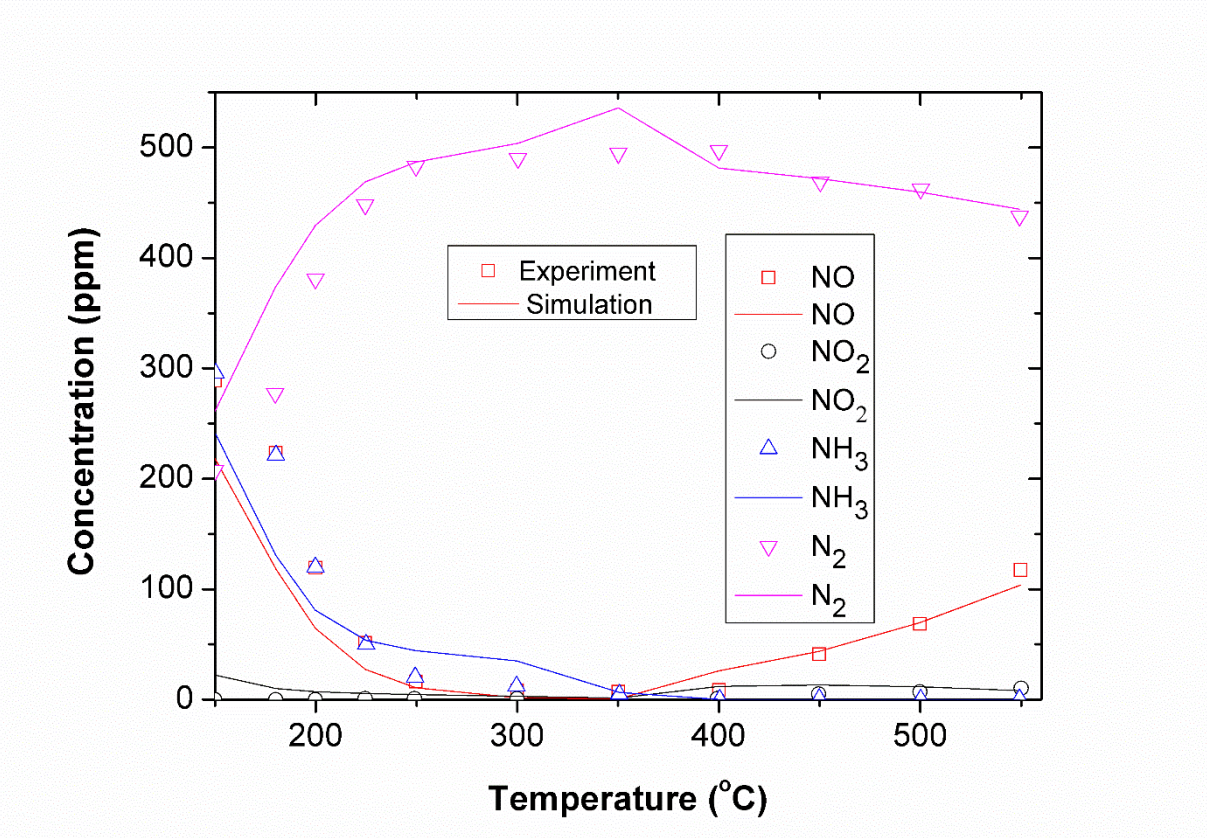

Figure 4.1. Comparison of experimental and 1D + 1D model predictions for steady state concentrations on Cu-Cha catalyst. Feed: 375 ppm NO, 125 ppm NO_2, 500 ppm NH_3, 5% O_2, 5% H_2O

The experiments are conducted at different temperatures for feed composition of 375 ppm NO, 125 ppm NO_2, 500 ppm NH_3, 5% O_2, 5% H_2O for a Cu-cha SCR catalyst. As can be seen from **Figure 4.1**, the model is able to predict the experimental data with the provided kinetic parameters with reasonable accuracy.

In the next step, the 1D model with internal mass transfer approach presented in **Section 2.2** is used to simulate the experiments. It can be seen from **Figure 4.2** that the results from the 1D model with the overall mass transfer coefficients where the reaction diffusion equation is replaced by first order rate approximation to evaluate the internal mass transfer coefficient is

quite comparable with 1D+1D model results and the experimental results.

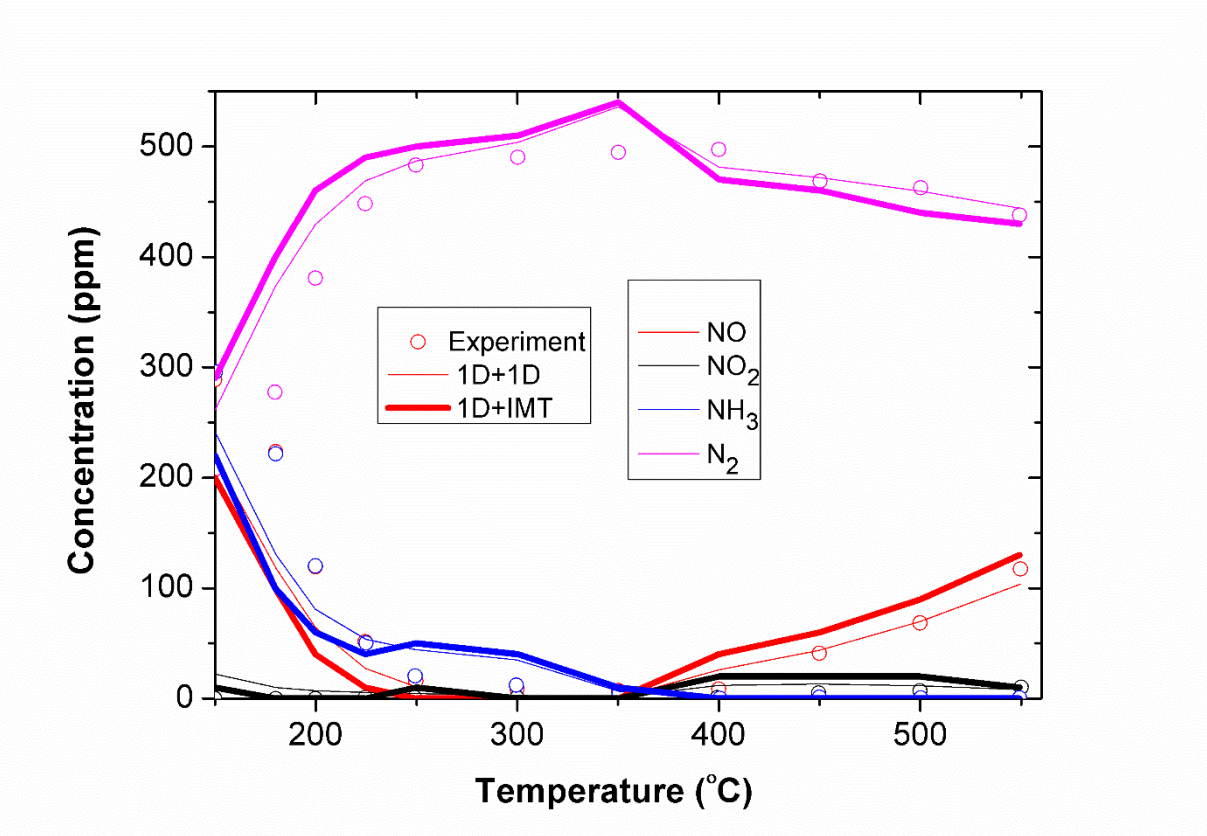

Figure 4.2. Comparison of experimental and 1D + 1D model and 1D model (internal mass transfer coefficient) predictions for steady state concentrations carried on Cu-Cha catalyst. Feed: 375 ppm NO, 125 ppm NO_2, 500 ppm NH_3, 5% O_2, 5% H_2O

Table 4.3. Model parameters used for the simulation of Cu-Cha experiments

Parameter	value	unit
$\boldsymbol{u}$	$0.45 \cdot T/300$	m/s
$\boldsymbol{L}$	0.02	m
$\boldsymbol{CPSI}$	400	[-]
$\boldsymbol{A_{geo}}$	2492	m^{-1}
$\boldsymbol{\delta_{wc}}$	60	μm
$\boldsymbol{\varepsilon_g}$	0.626	[-]
$\boldsymbol{\varepsilon_{wc}}$	0.4	[-]
$\boldsymbol{Sh_{int,\infty}}$	3	[-]
Λ	0.38	[-]

In the next step, side reactions (R4.7 & R4.8) accounting for the formation of NH_4NO_3 and N_2O are not considered. It is observed that the results of the simulations are not affected avoiding retuning of the parameters.

Table 4.4. Difference in runtime between the 1D model and the grey box model

Model	Time	Speedup
1D model	9s	-
Grey box model	0.3s	30

4.2.2. WHTC driving cycle simulations

Before carrying out the optimization, the 1D isothermal model is used to simulate the World Harmonized Transient cycle (WHTC). The ammonia dosing is carried out with a fixed NH_3/NO_x ratio of 1. In a 1D isothermal model it is assumed that catalyst temperature throughout the length of the catalyst is same as the inlet gas temperature.

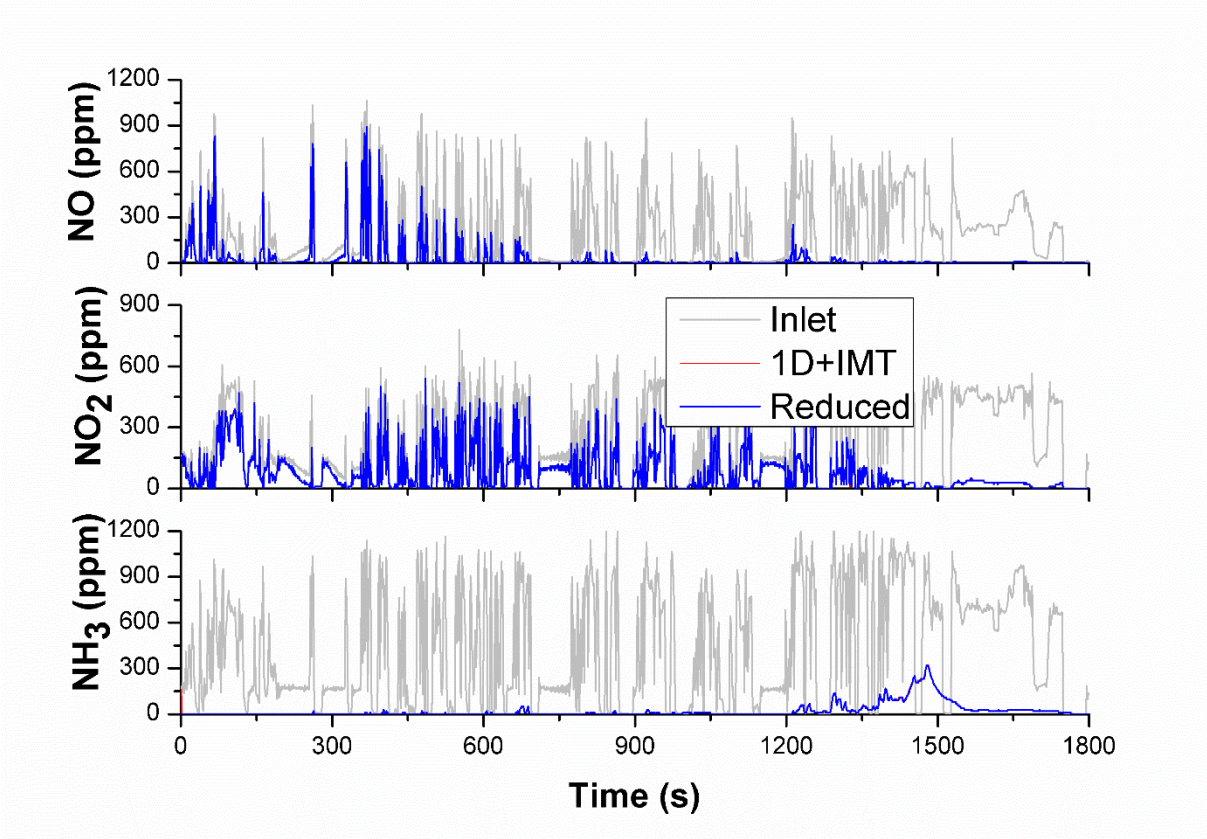

Figure 4.3. Comparison of 1D model (internal mass transfer coefficient) and reduced model for the transient WHTC driving cycle for Cu-cha catalyst with ammonia dosing ratio (NH_3/NO_x =1). (Red line not observed as the reduced model result is exactly the same as the 1D model result)

Even though this assumption is valid in case of steady-state simulations, in case of transient simulations where the inlet temperature varies quite frequently, the heat front moving forward might lead to sudden temperature rise resulting in additional NH_3 breakthrough because of NH_3 desorption. This phenomenon is neglected in the present study in order to minimize the size of the ODE model and in turn the size of the resulting NLP for optimization. The simulation was carried out with a monolith diameter of 8 inches and length 6 inches, washcoat thickness of 60 μm is considered. The results of the simulation are presented in **Figure 4.3**. With a constant ammonia dosing ratio (NH_3/NO_x =1) it was observed that the average conversion over the whole driving cycle is 61.3%. It can be also seen that large NH_3 excursions (> 190 ppm) occur especially at high temperatures towards the end of the cycle (1200s to 1800 s) when the adsorption capacity of NH_3 is reduced. From **Figure 4.3**, it can be observed that the simulation result from the grey-box model presented in **Section** 2.3 is similar to the result obtained with the 1D model. The runtime difference between the 1D model and the grey-box model to simulate 1800 s of the WHTC driving cycle is tabulated in **Table 4.4**. Both models are developed in FORTRAN and the implicit solver DASPK [116] based on Backward differentiation formula (BDF) methods is used as solver. It can be seen that the grey-box model is several orders of magnitude faster than the 1D model without loss of accuracy.

4.2.3. Optimization problem formulation for Ammonia dosing

The strategy adopted in the present study to optimize the ammonia dosing for a given WHTC driving cycle is as follows: In a typical driving cycle the inputs to the catalyst, i.e. concentrations, temperature and mass flow rates, are highly transient and change at every time instance. This drastic change in inlet conditions can result in instability due to non-convergence of the DAE solver and cause failure of the optimization, when sequential methods are used. Also simultaneous methods like multiple shooting and Direct collocation are better suited for inlet trajectory optimization problems [61, 117].

The grey-box model presented in **Section 2.3** is used in the optimization process along with the kinetics for NH_3-SCR on Cu-cha catalyst tabulated in **Table 4.1 & 4.2**. Maximization of NO_x conversion at any time instant is chosen as the objective function for this problem. Simultaneously, an additional condition of NH_3 slip of less than 10 ppm at any instant of time is imposed. To that end, additional path constraints are incorporated in to the NLP to ensure that this condition is satisfied.

First, in the 1D model it was observed that in the equations (4.2) and (4.3), ignoring the accumulation terms on the left hand side and solving model in DAE mode, i.e. assuming that the dynamics of the bulk gas and solid gas species (gas species in the washcoat) is faster than that of the adsorbed ammonia, did not have any influence on the simulation results. The 1D model can be formulated as a DAE system and can be used for the optimization, but this would mean that the number of decision variables to be optimized in the NLP will be large, thus slowing the optimization process. Therefore, the grey-box model with further model reduction as demonstrated in previous section is used, which would lead to a reduced NLP size. The optimization problem is formulated as an ODE problem rather than a DAE problem to minimize the number of NLP decision variables. The ODEs are structured in such a way that only the NH_3 adsorbed species are considered as state species meanwhile the bulk gas species and the solid gas species are not involved in the NLP. By this method, the number of variables in the NLP are greatly reduced. In this model, the ammonia dosing variable is chosen as piecewise constant in each time step rather than a polynomial. Also no algebraic equations ($\boldsymbol{y}$) and free parameters ($\boldsymbol{\beta}$) are considered in NLP. The state variables consist of the adsorbed NH_3 species and their number is dependent on the number of axial discretization points of the catalyst along its length. In addition to the adsorbed NH_3 species two more ODEs, cumulative NH_3 slip and cumulative NO_x conversion, are added to the state vector. The NLP transcription of the problem is given below:

$$\text{Objective}: \text{Max} \int_{t_0}^{t_f} f_3 \, dt \tag{4.23a}$$

$$h_i f_1\left(z_{i,j}, u_i\right) - \sum_{j=0}^{n_c} z_{i,j,1} \cdot \dot{l}_j\left(\tau_j\right) = 0 \,, i = 1,2, \dots, n_e, \quad j = 1,2, \dots, n_c, \tag{4.23b}$$

$$h_i f_2\left(z_{i,j}, u_i\right) - \sum_{j=0}^{n_c} z_{i,j,2} \cdot \dot{l}_j\left(\tau_j\right) = 0 \,, i = 1,2, \dots, n_e, \quad j = 1,2, \dots, n_c, \tag{4.23c}$$

$$h_i f_3\left(z_{i,j}, u_i\right) - \sum_{j=0}^{n_c} z_{i,j,3} \cdot \dot{l}_j\left(\tau_j\right) = 0 \,, i = 1,2, \dots, n_e, \quad j = 1,2, \dots, n_c, \tag{4.23d}$$

where $f_1(z_{i,j}, u_i) = \frac{d\theta_{NH_3}}{dt}$, (4.23e)

$$f_2(z_{i,j}, u_i) = \frac{dy_{\mathrm{NH_3}}}{dt} \ , \quad (4.23f)$$

$$f_3(z_{i,j}, u_i) = \frac{dy_{X_{\mathrm{NO_x}}}}{dt} \quad (4.23g)$$

$$z_{i+1,0,1} = z_{i,K,1} \ , \ \ i = 1,2, \dots, n_{\mathrm{e}} \quad (4.23h)$$

$$z_{i+1,0,2} = z_{i,K,2} \ , \ \ i = 1,2, \dots, n_{\mathrm{e}} \quad (4.23i)$$

$$z_{i+1,0,3} = z_{i,K,3} \ , \ \ i = 1,2, \dots, n_{\mathrm{e}} \quad (4.23j)$$

$$z_{i+1,0,2} - z_{i,0,2} \ \leq 10 \text{ ppm} \quad (4.23k)$$

$$u_{\mathrm{L}} \leq u_{i,j} \leq u_{\mathrm{U}} \quad (4.23l)$$

$$z_{\mathrm{L},1} \leq z_{i,j,1} \leq z_{\mathrm{U},1} \quad (4.23m)$$

$$z_{\mathrm{L},2} \leq z_{i,j,2} \leq z_{\mathrm{U},3} \quad (4.23n)$$

$$z_{\mathrm{L},3} \leq z_{i,j,3} \leq z_{\mathrm{U},3} \quad (4.23o)$$

Equations (4.23e)-(4.23g) represent the states (adsorbed ammonia, cumulative NH_3 slip and cumulative NO_x conversion) and (4.23b)-(4.23d) represent the formulation of each of those in terms of collocation polynomials. The continuity of these states between each element i is ensured by constraints (4.23h)-(4.23j). The main constraint of limiting the NH_3 slip at any time instant to less than 10 ppm is imposed by (4.23k) which states that the difference between the first collocation point of the element $i + 1$ and element i should be less than or equal to 10 ppm for the $z_{,2}$ variable, i.e. for the cumulative NH_3 slip variable. Finally, the objective function is

formulated as maximization of cumulative NO_x conversion at any time instant, which ensures that the NO_x conversion is maximized at each time step.

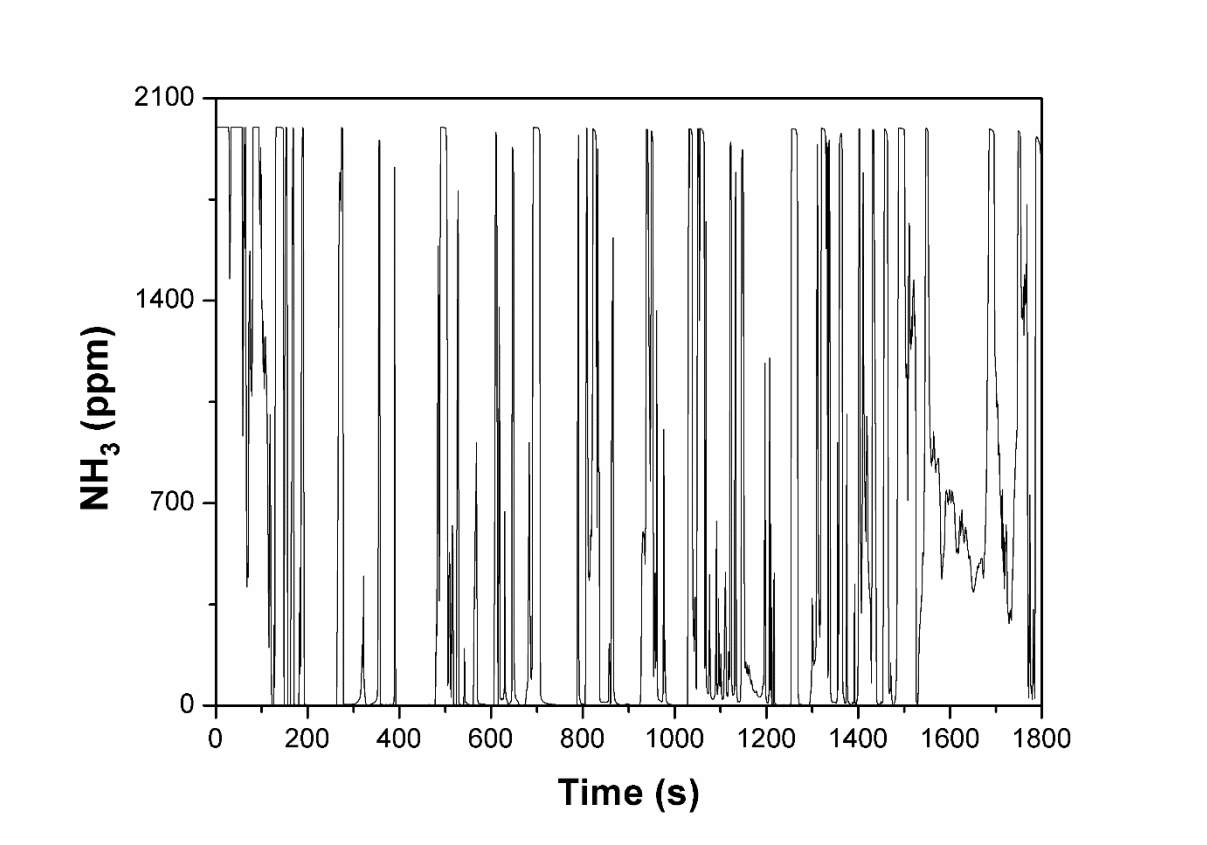

Figure 4.4. Optimized inlet ammonia dosing profile for the WHTC driving cycle.

The above described optimization problem is formulated in the software framework CasADi (Computer algebra system with Automatic Differentiation) [118]. To solve the NLP, the solver IPOPT [53], which can be accessed from CasADi, is used. IPOPT is based on interior point methods to find local optima to large scale NLPs.

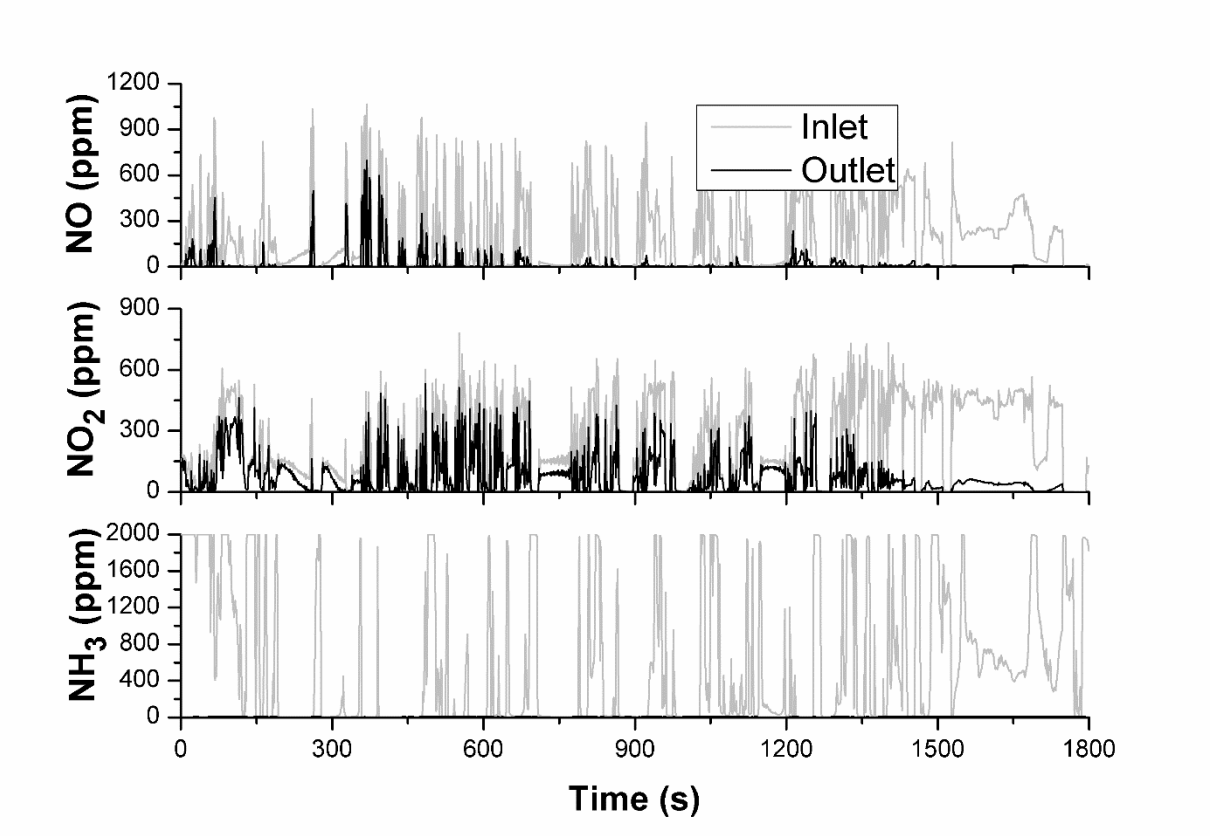

Figure 4.5. Simulation results for optimized ammonia dosing for the WHTC driving cycle.

Figure 4.4 presents the NH_3 dosing profile with respect to time for the WHTC driving cycle for the entire 1800 seconds obtained from the optimization. The catalyst is discretized into 5 axial grid points along the length of the catalyst, which resulted in 52178 control parameters to be optimized according to equation (2.39). The performance of the catalyst with the optimized ammonia dosing is presented in **Figure 4.5**. It was observed that the average conversion over the whole time horizon of the transient cycle is 65.45%. **Figure 4.6** presents the NH_3 slip at the end of the catalyst with respect to time over the entire driving cycle. It can be observed that the NH_3 slip at any time instant during the cycle is clearly less than 10 ppm as desired.

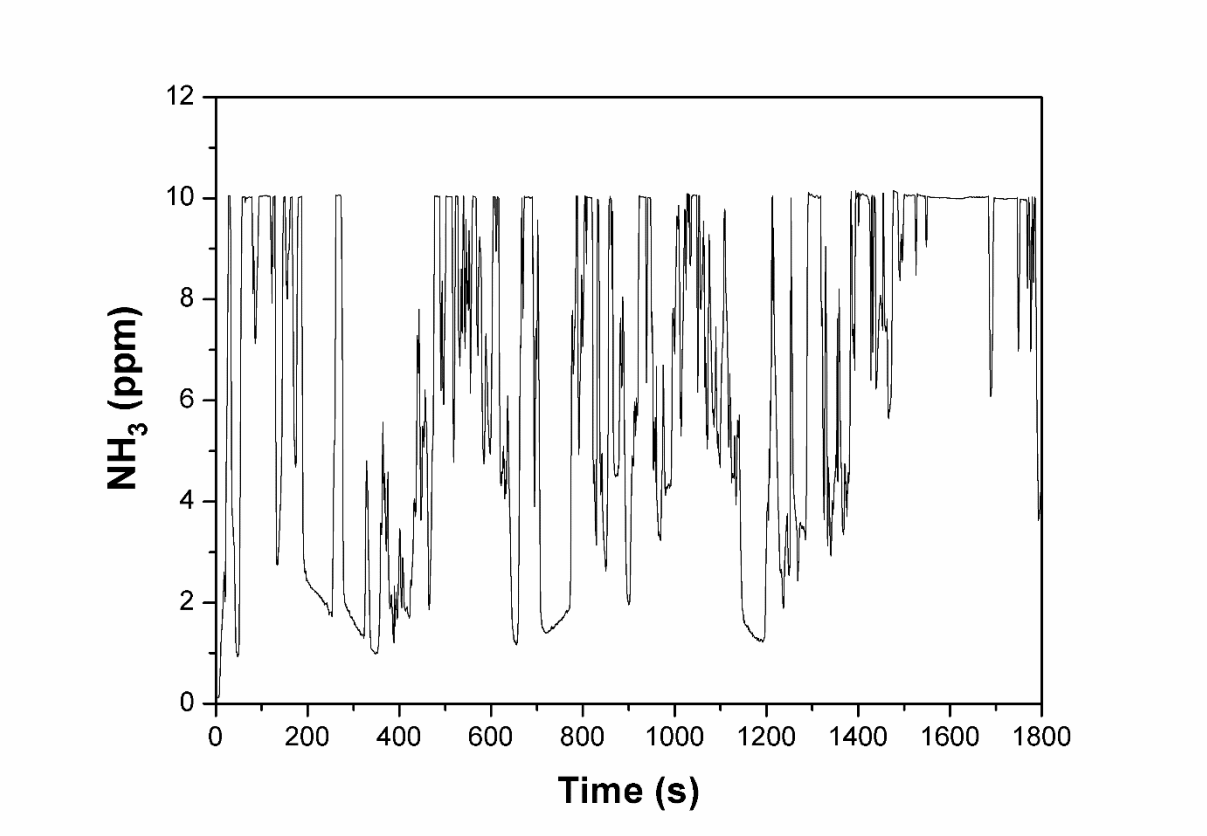

Figure 4.6. Ammonia excursion over the WHTC driving cycle for optimized dosing.

Figure 4.7 presents the comparison between the cumulative NH_3 slip between the uniform and optimum dosing profiles. The overall cumulative NH_3 slip over the whole cycle in case of the uniform dosing was about 175.6 mg whereas in case of the optimum dosing case it was observed to be 41.2 mg. The overall cumulative NH_3 slip over the whole cycle using the optimum dosing profile reduced by 76.5 % compared with the uniform dosing profile.

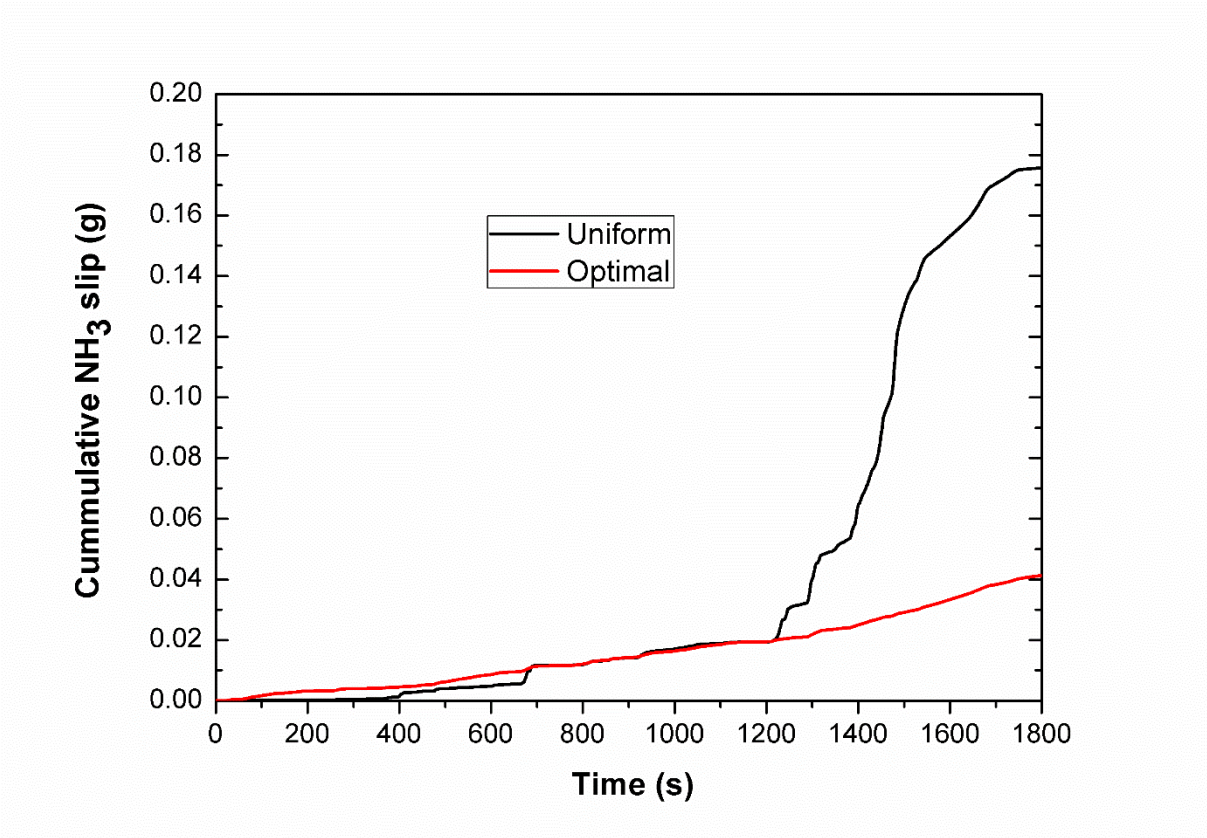

Figure 4.7. Cumulative NH3 slip comparison between uniform and optimum dosing.

5. Inlet lambda trajectory Optimization

A typical control unit in a gasoline car is equipped with two λ-sensors, a wide-range λ-sensor (LSU) that is placed directly after the engine and a switch-type λ-sensor (LSF) that is placed after the three-way catalyst (TWC). The LSF can only indicate the qualitative state of the catalyst i.e.; whether the catalyst is full or depleted without providing any exact values. In addition, two cascaded controllers to adjust the air-to-fuel ratio are also included. The complete control unit with the placement of the sensors is depicted in Figure 5.1. The control unit has an inner fast feedback loop, that controls the upstream λ exiting the engine and a much slower second control loop, that stabilizes the voltage of the switch-type λ-sensor placed after the first catalyst. The main function of the second controller called as the catalyst controller is to maintain the filling state of the catalyst at desired value. Usually a PI controller is used for this purpose with the goal to stabilize the voltage of the downstream switch-type λ-sensor at a value of around 650 mV. The exact value of the voltage is catalyst specific and is also dependent on the tuning of the controller. In order to avoid stability problems these controllers have to be applied very slowly [5, 119]. The downstream λ-sensor provides only limited information about the state of the catalyst, since the sensor voltage depends mainly on the oxygen filling level at the end of the catalyst. Using additional information provided by the λ-sensor placed upstream of the catalyst and an observer model of the catalyst's oxygen storage behavior, the actual filling state of the catalyst can be estimated more accurately [119, 120].

Another important aspect is the appearance of fuel cut-offs during deceleration of the vehicle. These occur frequently with a manual transmission. During a fuel cut-off the exhaust gas consists of only air, which causes the catalyst to get completely oxidized. In this situation an accidental lean excursion of the λ control will cause an immediate NOx breakthrough. Therefore the catalyst's oxygen storage must be depleted, when the fuel injection is enabled again. For a fast depletion after a fuel cut-off, the conventional PI controller setup is usually too slow. Therefore a feed forward strategy has to be used. Also as a first step obtaining an offline solution to such problems, which can be used as a reference solution to online calibration of the controls, is necessary. To obtain a solution for such kind of scenario it was showed [5, 119, 120] that physical based models are essential for the modeling effort to represent the system accurately. It was also shown that to model such scenarios it is not necessary to use detailed mechanisms and simple oxygen dynamics kinetics is sufficient. Also it is accepted that simple isothermal models are enough to model the observer TWC model. Most of the control models

presented in the literature are based on simple models which are unphysical [121]. Also the optimization methods used are often manual or non derivative based heuristic methods like Genetic algorithm, Neural networks etc. The objective of this chapter is to address this issue and propose an optimization methodology to efficiently obtain an optimal inlet lambda trajectory solution to typical fuel cut-off scenario. This chapter is organized in the following way. In **Section 5.1** the TWC kinetics used are presented. In **Section 5.2** the isothermal 1D reactor model used for modeling the three-way catalyst is presented along with the model discretization and validation of the model with experimental results. In the subsequent **Section 5.3** the optimization strategy adopted is described in detail along with the problem formulation are described followed by the optimization results obtained.

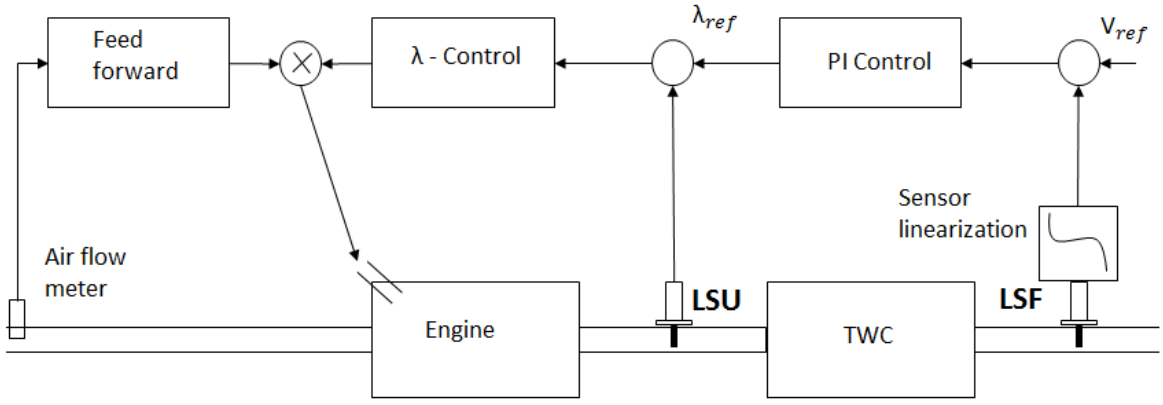

Figure 5.1. Three way catalyst control structure

5.1. TWC kinetics

Usually, the TWC reaction mechanism is quite complex with different reaction steps consisting of oxidizing (CO, HC, H_2) and reducing (NO_x) of species. It is demonstrated that for control applications especially at higher temperatures, the storage kinetics are the predominant reactions controlling the typical lambda behavior in a TWC and considering them alone is sufficient [5, 31]. The reaction kinetics for the present study are taken from the work of Möller [31, 119]. The mechanism consists of only the storage reactions which describe the dynamics of Ceria.

The reaction mechanism proposed is very simple, considering only 3 global reaction. The reactions considered in this model are given below

$$O_2 + 2Ce_2O_3 \leftrightarrow 2Ce_2O_4 \qquad \text{(R5.1)}$$

$$H_2 + Ce_2O_4 \leftrightarrow H_2O + Ce_2O_3 \quad \text{(R5.2)}$$

$$CO + Ce_2O_4 \leftrightarrow CO_2 + Ce_2O_3 \quad \text{(R5.3)}$$

Only O_2, CO, H_2, CO_2, H_2O, H_2, Ce_2O_3 and Ce_2O_4 are considered in the reaction mechanism. Additionally, other species like hydrocarbons (HC) and nitric oxides (NO, NO_2) are not considered and it is assumed, that their influence on the oxygen storage dynamics does not differ substantially from the one of oxidizing (CO and H_2) and reducing (O_2) species, respectively. Further, Möller et al. [31, 119] have demonstrated experimentally that the ceria reactions are in equilibrium. They have performed studies with only CO_2 and H_2O with reduced Ce and have shown the reverse production of CO and H_2. The results from their study have provided further evidence that the ceria is involved in the water gas-shift reaction [31, 122, 123]. They have shown that oxygen storage kinetics and the steady-state water-gas shift activity can be described by one set of kinetic parameters and that the water-gas shift reaction can be described by a combination of reactions 5.2 and 5.3. The rate of reactions for each of the reactions are expressed as

$$r_1^{\mathrm{f}} = k_1^{\mathrm{f}} C_{O_2} \left(1 - \theta_{\mathrm{Ce_3O_4}}\right)^2 \qquad r_1^{\mathrm{b}} = k_1^{\mathrm{b}} \theta_{\mathrm{Ce_3O_4}}^2 \quad (5.1)$$

$$r_2^{\mathrm{f}} = k_2^{\mathrm{f}} C_{H_2O} \left(1 - \theta_{\mathrm{Ce_3O_4}}\right) \qquad r_2^{\mathrm{b}} = k_2^{\mathrm{b}} C_{H_2} \theta_{\mathrm{Ce_3O_4}} \quad (5.2)$$

$$r_3^{\mathrm{f}} = k_3^{\mathrm{f}} C_{CO_2} \left(1 - \theta_{\mathrm{Ce_3O_4}}\right) \qquad r_3^{\mathrm{b}} = k_3^{\mathrm{b}} C_{CO} \theta_{\mathrm{Ce_3O_4}} \quad (5.3)$$

The forward reaction rates are evaluated by the Arrhenius equation

$$k_i^{\mathrm{f}} = E_{if} e^{-E_i/RT} \quad (5.4)$$

The reaction rate constant of the reverse reactions is then computed from chemical equilibrium:

$$k_i^{\mathrm{b}} = \frac{k_i^{\mathrm{f}}}{K_i} \quad (5.5)$$

In order to ensure thermodynamic consistency of the complete mechanism all reactions are simulated as reversible reactions. The equilibrium constant K_i is calculated based on the change of the Gibbs free energy over the reaction:

$$K_i = e^{-\Delta G_i/RT} \tag{5.6}$$

The Gibbs free energy is given by

$$\Delta G_i = \Delta H_i - T\Delta S_i \tag{5.7}$$

where ΔS_i and ΔH_i are the entropy change and enthalpy change of the reaction. The kinetic parameter values for the rate constants and the thermodynamic values for the entropy and enthalpy of the gas species and Ce are taken from Möller et al [31, 119].

5.2. Catalyst Model

In order to model the observer TWC which can accurately describe the oxygen storage level and dynamics of the TWC, a typical isothermal 1D model presented in **chapter 2 Section 2.1.2** is used in this study. Some of the major assumptions followed in modeling the reactor are:

1) The model solves for only the axial direction in the flow direction.
2) The model is assumed to be isothermal, i.e. the exothermicity of the reactions is insignificant at these temperatures resulting in identical gas phase and solid phase temperatures.
3) Axial dispersion is neglected as the axial Peclet number is found to be greater than 10.

The mathematical equations used to model the TWC are similar to the general 1D model presented in **Section 2.1.2** considering only the equation 2.4 & 2.11.

The Ceria dynamics is evaluated by

$$\frac{d\theta_{Ce_3O_3}}{dt} = S_{Ce_3O_3} \tag{5.8}$$

The boundary conditions assumed here are similar to the model in **Section 2.1.2**.

5.2.1. Model Discretization

The approach of method of lines using finite differences is used to discretize the partial differential equations in to ordinary differential equations. The channel is discretized in to N-1 equal parts along the length of the reactor. At the first point near the entrance, the Dirichlet boundary condition $X_{f,i,0} = X_{f,i,t}$ is employed in equation (2.4) resulting in (5.9)

$$\frac{dX_{\mathrm{f},i,j}}{dt} = -u\frac{X_{\mathrm{f},i,j} - X_{\mathrm{f},i,0}}{\Delta x/2} - \frac{4\boldsymbol{k_{me}}(X_{\boldsymbol{s,i,j}} - X_{\boldsymbol{f,i,j}})}{d_{\mathrm{h}}} \tag{5.9}$$

Where $X_{\mathrm{f},i,0}$ is the mole fraction of species *i*, at the entrance and $X_{\mathrm{f},i,t}$ is an independent variable which can vary with time.

At all the other interior points, the discretization of equation (5.10) resulted in

$$\frac{dX_{f,i,j}}{dt} = -u\frac{X_{f,i,j} - X_{f,i,j-1}}{\Delta x} - \frac{\boldsymbol{4k_{me}}(X_{\boldsymbol{s,i,j}} - X_{\boldsymbol{f,i,j}})}{d_h} \tag{5.10}$$

For all the points, the solid phase species balance discretization resulted in equation (5.11)

$$\frac{dX_{f,i,j}}{dt} = \frac{\boldsymbol{k_{me}}(X_{\boldsymbol{s,i,j}} - X_{\boldsymbol{f,i,j}})}{\delta_{wc}} + \frac{S_{cat}\boldsymbol{S}(X_{\boldsymbol{s,i,j}})}{c_T} \tag{5.11}$$

5.2.2. Model validation with experiments

In order to first validate the model and the reaction kinetics, the experiments used to parametrize the kinetics is taken from Möller et al. [31, 119]. Figure 4.2 from the thesis is chosen for this task. Here the experiments are modeled with transient input traces of O_2 and CO with different amplitudes and frequencies and with fixed amounts of CO_2 and H_2O. Additionally the temperature is ramped slowly from 600 °C to 200 °C. The resulting CO and H_2 outlet emissions of the measurement are shown in Figure 5.1. The 1D model presented in **Section 5.2** along with the reaction kinetics presented in **Section 5.1** is used. It can be seem from the **Figure 5.2** that the model is able to predict the experimental results with reasonable accuracy. The comparison between the experiments and the simulation are presented at 2 different times to demonstrate the robustness of the model.

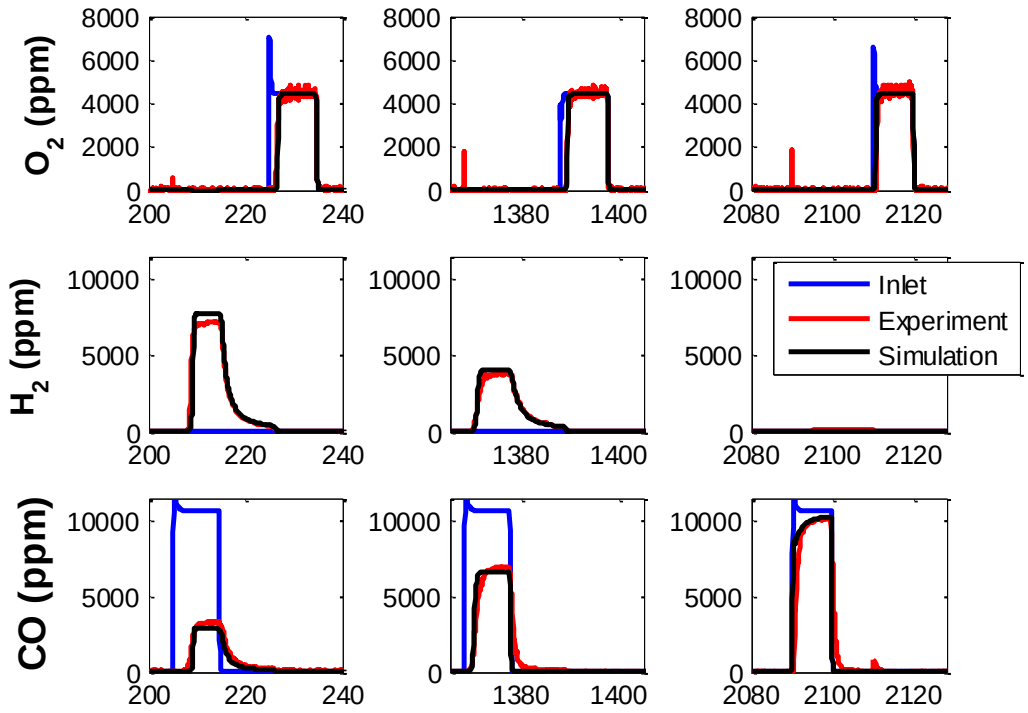

Figure 5.2. Zoomed O2, CO and H_2 concentration transients of the experiment shown in Fig. 3 [31] **at three different times. The inlet temperatures are approximately 580 °C (t = 220 s), 425 °C (t = 1380 s) and 330 °C (t = 2100 s)**

Another important effect that is captured by the model with the equilibrium oxygen storage kinetics is the production of H_2 at higher temperature due to the shift of chemical equilibrium of the water-gas shift reaction. The equilibrium constant of the reaction decreases with increasing temperature. The reaction is thermodynamically favored at low temperatures and kinetically favored at high temperatures. At higher temperatures, the amount of H_2 that is produced is limited by the chemical equilibrium of the water-gas shift reaction. Since the chemical equilibrium of the water-gas shift reaction shifts away from H_2 and CO_2 at lower temperatures, the H_2 first increases till approximately 490°C is reached. Beyond a temperature of approximately 490 °C (900 seconds), the chemical equilibrium is no longer reached and the water-gas shift reaction becomes kinetically limited resulting in complete breakthrough of CO at lower temperatures. This behavior is reproduced well with estimated rate parameters confirming that reactions (R5.3) & (-R5.2) are sufficient to represent the water gas shift reaction. [119]

5.3. Fuel cut-off scenario

The aim of the feed forward control after a fuel cut-off is to deplete the oxygen storage as quickly as possible to a reasonable value to avoid a NOx breakthrough caused by a lean disturbance which cannot be buffered by the oxidized catalyst. Often this is done by a rich pulse with a certain duration and amplitude. However, this solution is relatively slow and causes delayed rich emissions. These rich emissions are problematic in combination with a catalyst controller, which does not consider this effect. Since these rich emissions occurs during a relatively long period, the catalyst controller tries to compensate for them and shifts the λ to the lean side. This causes a reoxidation of the catalyst and can lead to a NOx breakthrough [5, 119].

In the following section, the catalyst model presented in **Section 5.2** is used for the optimization of a feed forward inlet λ trajectory. The optimization criterion is defined as follows: The objective of the optimization is to obtain an optimal inlet lambda trajectory that would quickly stabilize the voltage of the downstream switch-type λ sensor to 650 mV and then remain there.

5.3.1. Optimization problem formulation for λ trajectory

In the present study, the λ upstream and downstream are evaluated from the measured concentrations according to equation (5.12)

$$\lambda_{calc} = \frac{2C_{O_2} + C_{CO} + 2C_{CO_2} + C_{H_2O}}{2C_{CO} + 2C_{CO_2} + C_{H_2} + C_{H_2O}} \tag{5.12}$$

As discussed before, the first sensor which is located upstream of the catalyst is called LSU which can measure the air-fuel ratio (or equivalently, lambda) in a wide range (from λ=0.7 to 2.4). This linearized measurement is used as the feedback signal in engine lambda control. The downstream sensor located after the catalyst is called LSF which behaves in a binary manner depending on the air-fuel ratio of the exhaust gas. The output voltage of this nonlinear sensor is used for NO_x control and TWC monitoring [124]. **Figure 5.3** depicts a typical downstream lambda vs LSF sensor output voltage used in the present study to interpolate the voltage from a given lambda value. In the present study, the optimization is carried out by employing the method of Direct collocation with OCFE as described in **Section 2.1.3** of **chapter 2**. The reason for using this strategy instead of any other strategy to optimize the lambda trajectory is straightforward. Also in this problem, the transient inlet conditions can result in instability due to non-convergence of the DAE solver and cause failure of the optimization, when sequential

methods are used. Also the solution desired, inlet trajectory, is quite similar to that of the NH_3 dosing problem in Chapter 4 that Direct collocation yielded a very stable and quick solution. Additionally, the number of control parameters to be optimized can be very high similar to the NH_3 dosing case.

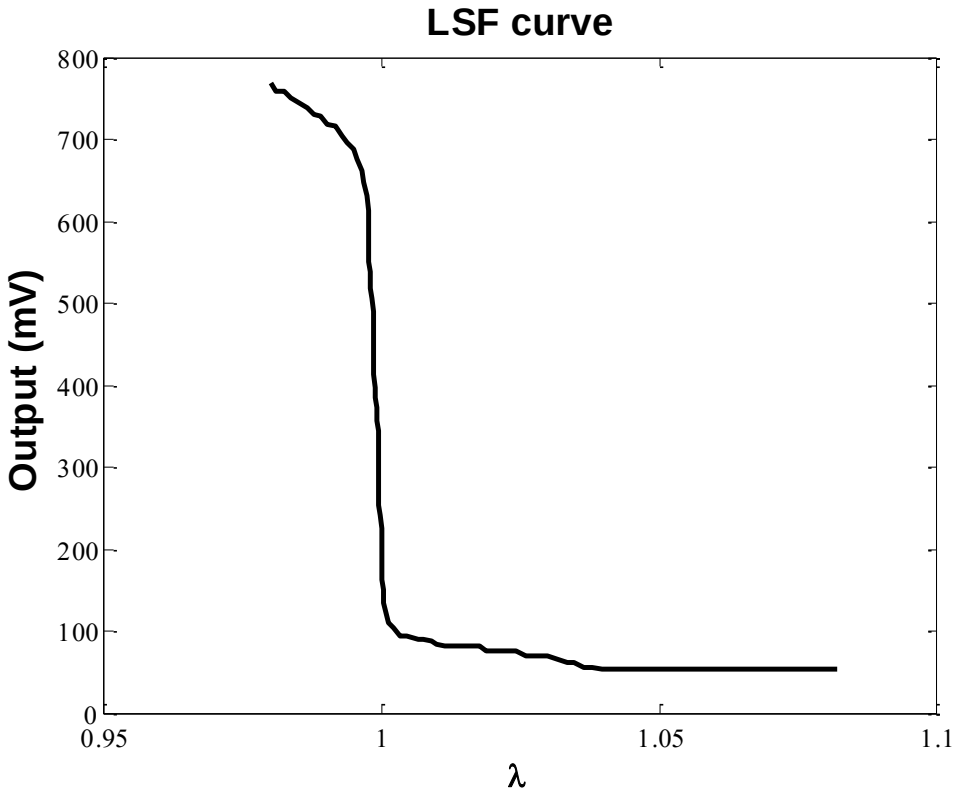

Figure 5.3. Typical output voltage of a LSF [124]**.**

Minimization of the square of the difference between the output lambda and the standard lambda corresponding to 650 mV LSF voltage over the entire time horizon is chosen as the objective function for this problem. Since in a TWC the concentration of H_2O and CO_2 are much higher compared to other species they are assumed to be constant. O_2 and CO are assumed to be the control parameters to be optimized at every time instant to minimize the objective function. The variation of the composition of these species is found to vary the value of the lambda evaluated using (5.12). Before formulating the optimization problem, some model reduction steps are undertaken to reduce the size of the NLP and ease the optimization.

Firstly in the 1D model it was observed that in the equations (5.10) and (5.11), ignoring the accumulation terms on the left hand side, i.e. assuming that the dynamics of the bulk gas and

solid gas species is faster than that of the ceria, did not have any influence on the simulation results. Therefore the 1D model can be modeled as a DAE system and can be used for the optimization. This model can be further reduced in to a grey-box model to reduce the number of state variables in turn reduce the number of NLP variables. Even though the grey-box model presents with this advantage, one limitation of the grey-box model is its non-applicability to systems with reaction mechanisms having inhibition factors. So in order to demonstrate the robustness of the optimization methodology and its applicability to wide range of problems, in this present study the optimization problem is formulated with the DAE model. This would result in large number of decision variables to be optimized in the NLP but the effect on the NLP size is minimal in this case because of the very short time horizon that will be employed here. Here the time horizon is chosen as 20 seconds unlike the huge time horizon (1800s) in the NH_3 dosing problem. The optimization problem is formulated as DAE problem which means that the differential equations, whose accumulation terms on the RHS are considered, are formulated as differential equations and the differential equations, whose accumulation terms on the RHS are not considered, are formulated as algebraic equations. (Note: In the NH_3 dosing problem the algebraic equations are not considered as part of the NLP). The species balance equation for the gas concentrations in the washcoat (5.11) is included in the NLP structure as algebraic equation. Whereas the species balance equation for the gas concentrations (5.10) in the gas phase is solved at each time instant as an algebraic equation but is not involved in the NLP. The equation (5.8) representing the relative oxygen storage level at each of the axial positions along the channel length is involved as the differential variables in the NLP.

Here in this problem, the O_2 and CO dosing variables are chosen as piecewise constant in each time step rather than a polynomial. Also no time independent free parameters ($\boldsymbol{\beta}$) are considered in NLP. The state variables consist of the Ce species (Ce_2O_3) and the 5 gas species (O_2, CO, H_2, CO_2, H_2O) in the solid phase formulated as algebraic variables. Their number is dependent on the number of axial discretization points of the catalyst along its length. In addition, one more differential equation, which gives the square of the difference between the standard and measured output lambda are added to the state vector. The NLP transcription of the problem is given below:

$$\text{Objective}: \text{Min} \quad f_2 \tag{5.10a}$$

$$h_i f_1(z_{i,j}, u_i) - \sum_{j=0}^{n_c} z_{i,j,1} \cdot \dot{l}_j(\tau_j) = 0\,, i = 1,2,\dots,n_e, \quad j = 1,2,\dots,n_c, \tag{5.10b}$$

where $f_1(z_{i,j}, u_i) = \frac{d\Theta_{Ce_3O_3}}{dt}$

$$f_2(z_{i,j}, u_i) = \quad (\lambda_{calc} - 0.9965)^2 \ , \tag{5.10c}$$

$$z_{i+1,0,1} = z_{i,K,1} \ , \ \ i = 1,2,\dots,n_e \tag{5.10d}$$

$$u_{\mathrm{CO,L}} \le u_{i,j} \le u_{\mathrm{CO,U}}\,, \qquad u_{O_2,\mathrm{L}} \le u_{i,j} \le u_{O_2,\mathrm{U}} \tag{5.10e}$$

$$0 \le z_{i,j,1} \le 1 \tag{5.10f}$$

Equations (5.10e)-(5.10f) represent the CO, O_2 bounds and the bounds on the relative storage level of ceria and (5.10b) represent the formulation of each of those in terms of collocation polynomials. The continuity of these states between each element i is ensured by constraints (5.10d). Finally, the objective function is formulated as minimization of square of the difference between the calculated λ_{calc} and the reference value at any time instant by (5.10c). The above described optimization problem is formulated in the software framework CasADi (Computer algebra system with Automatic Differentiation) [118]. CasADi is a very efficient tool for the evaluation of first order and second order derivatives of the objective and the constraints. To solve the NLP, the optimization software IPOPT [53], which can be accessed from CasADi, is used.

5.4. Result & discussion

The result of the optimization can be seen in **Figure 5.4**. The optimization problem is solved over a time horizon of 20 s and is divided into 60 finite elements. At the start of the simulation the relative oxygen level of the ceria is assumed to completely full. The upper plot shows the trajectory and the lower plot shows the corresponding sensor signal. It can be seen that the optimal inlet trajectory consists of a large rich pulse followed by a lean pulse.

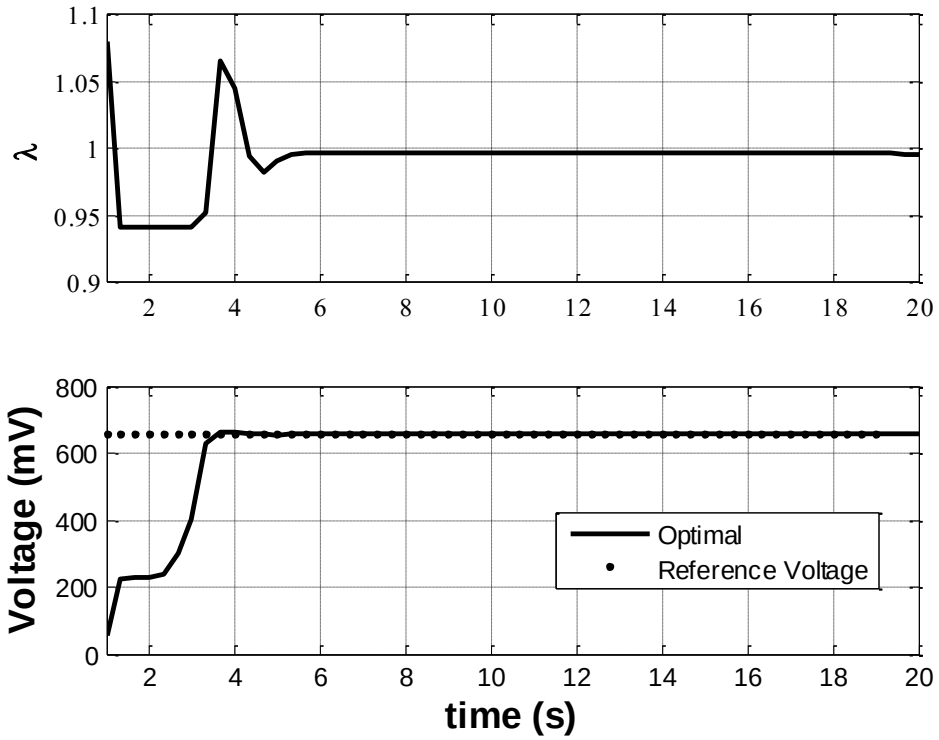

Figure 5.4. a) The optimal inlet lambda trajectory, b) The corresponding LSF voltage

The rich pulse drains the relative oxygen level and the following lean pulse fills the oxygen level and stabilizes the voltage. With this strategy the catalyst is emptied very quickly and the sensor voltage shows no overshoot and stabilizes very quickly. The corresponding optimized inlet CO and O_2 pulses are presented in **Figure 5.5**.

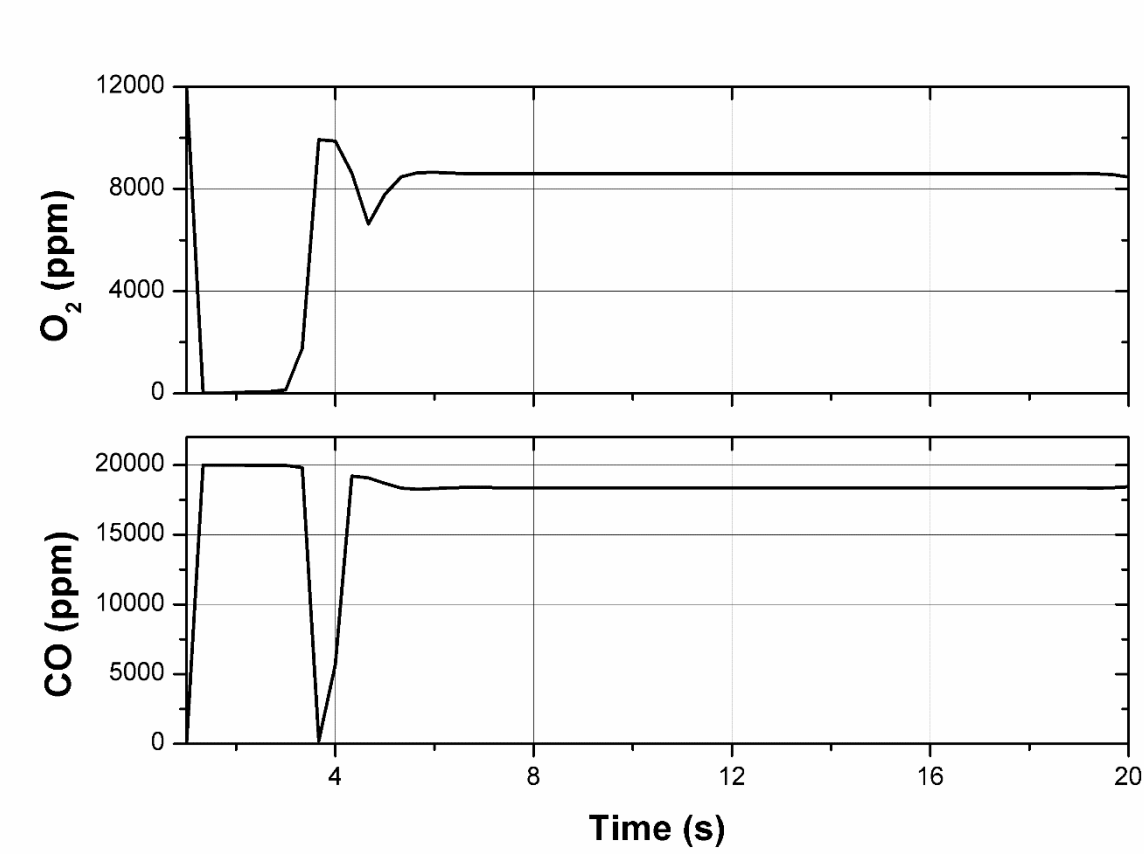

Figure 5.5. a) Optimal inlet O_2 pulsing solution b) Optimal inlet CO pulsing solution.

6. Conclusion and Outlook

In this work, a newly developed model for the optimization of axial precious metal loading in zone-structured catalysts to improve the conversion performance of the catalysts for automotive applications is presented. The 1D + 1D model together with the correlation between the PGM loading and washcoat thickness is able to predict diffusion limitations within the washcoat especially at higher PGM loading leading to high washcoat thickness. This effect is found to be important and ignoring this effect leads to trivial results. The most important outcome of this work is the demonstration of the methodology to incorporate a derivative based optimization scheme (IPOPT) to detailed models like 1D+1D and use of such models for automotive emission applications. The major challenge in setting up a model of this kind with such a large scale ODE system is the evaluation of derivatives of the objective function and constraints with respect to the control parameters to be optimized and provide them to the NLP solver. As explained in **Section 2.4**, to obtain the required derivatives the implicit DAE solver DASPKADJOINT is used along with the automatic differentiation tool TAPENADE in the reverse mode. Also the residual ODEs are solved in time using the coupled approach which includes solving of all the ODEs at once. The developed model is applied to two cases in order to demonstrate the usage of such robust methods. In the first application case, CO oxidation on Pd/Al_2O_3 based DOC catalyst, the model is applied for 3 subcases (2, 3 & 4 zones) to obtain an optimized loading profile to improve the conversion during cold start operation. In all the 3 subcases, it was observed that the profile had more activity in the zone near the entrance of the channel than in the other zones. It was also observed that presence of diffusion limitations has limited the loading in zone 1 to 303.5 g/ft^3, 286.6.5 g/ft^3 and 223.12 g/ft^3 respectively for the 3 subcases. In the second application case, CH_4 oxidation on Pd/Al_2O_3, the model is once again applied for 3 subcases (2, 3 & 4 zones) as in case 1 to obtain an optimized loading profile to enhance the performance of the catalyst. As the process suffered from deactivation, an aging model is also incorporated to simulate the behavior of such system. Similar to case 1, in all the 3 subcases the optimized profile had more PGM loading in zone 1 than in the other zones. Also not only the steady state conversion improved but also the effects of deactivation were not observed.

In the second part of this work, a systematic methodology to optimize NH_3 dosing in SCR catalysts for real world transient driving cycle using physics based models is presented. Firstly, an isothermal 1D +1D model was used to simulate the experiments from the literature and

which was later used as standard model to carry out the model reduction to 1D model. It was shown that the 1D model combined with the concept of internal mass transfer yielded comparable results with the 1D +1D model. In addition to this, the 1D model was further reduced to obtain the so called grey-box model which further reduced the computation effort and provided the same results. In this work, the Direct collocation method based on OCFE techniques was used to discretize the DAE constrained problem into a NLP to carry out the optimization. The obtained grey-box model was found to be well suited to carry out optimization studies with robust derivative based direct optimization methods like multiple shooting and direct collocation method. The optimized NH_3 dosing profile not only improved the overall efficiency of the process, but also ensured that the NH_3 slip is below 10 ppm throughout the cycle as desired. Such an optimized solution can be incorporated as a reference solution on an engine control unit to efficiently dose NH_3 to improve the efficiency and keep the NH_3 excursions under limit. The developed methodology can be applied to different after treatment systems to obtain optimal solutions with minimum effort. The developed methodology is presented as a proof of concept in this work to demonstrate the application of such robust optimization schemes to obtain solutions for after-treatment applications.

In the final part of this work, a systematic methodology to optimize the inlet lambda trajectory in TWC to avoid voltage overshoot and hence rich excursions using physics based models during a fuel cut-off scenario is presented. A simple isothermal 1D model is used as an observer model and the Direct collocation method based on OCFE techniques was applied to discretize the DAE constrained problem into a NLP to carry out the optimization. The optimal solution significantly reduces the recovery time of the downstream oxygen sensor and hence quickly stabilized the sensor voltage.

Outlook

The zone structured optimization methodology developed in the Chapter 3 can be applied effectively to other components of the exhaust aftertreatment system like TWC, SCR and LNT etc. to optimize their respective PGM loadings and improve their efficiencies. The grey box model presented in chapter 4 and 5 can be further improved by addition of the solid state energy balance equation to make it non-isothermal. Additionally, to work with reaction mechanisms having inhibition factors which is quite common in all types of exhaust aftertreatment catalysts. The improved grey box model with the optimization methodology presented can be very

effectively used not only to optimize inlet trajectory problems but also can be applied to parameter estimation problems for better kinetic parameters.

References

1. Faiz, A., Weaver, C.S., Walsh, M.P.: Air pollution from motor vehicles: Standards and technologies for controlling emissions. Advances in simultaneous strategies for dynamic process optimization. DC World Bank. (1996)

2. Deutschmann, O., Grunwaldt, J.-D.: Abgasnachbehandlung in mobilen Systemen: Stand der Technik, Herausforderungen und Perspektiven. Chemie Ingenieur Technik. 85, 595–617 (2013). doi:10.1002/cite.201200188

3. Silva, C., Ross, M., Farias, T.: Evaluation of energy consumption, emissions and cost of plug-in hybrid vehicles. Energy Conversion and Management. 50, 1635–1643 (2009). doi:10.1016/j.enconman.2009.03.036

4. Chaitanya S. Sampara: Global Reaction Kinetics for Oxidation and Storage in Diesel Oxidation Catalysts, University of Michigan. (2008)

5. Pascal Kiwic: Model-Based Control of Catalytic Converters. ETH Zurich. , Diss. ETH No. 20815, (2012)

6. Votsmeier, M., Kreuzer, T., Gieshoff, J., Lepperhoff, G.: Automobile Exhaust Control. In: Ullmann's Encyclopedia of Industrial Chemistry. Wiley-VCH Verlag GmbH & Co. KGaA (2000)

7. Dieselnet: Dieselnet : Diesel Emissions online (www.dieselnet.com)

8. Dubbe, H., Bühner, F., Eigenberger, G., Nieken, U.: Hysteresis Phenomena on Platinum and Palladium-based Diesel Oxidation Catalysts (DOCs). Emission Control Science and Technology. 2, 137–144 (2016). doi:10.1007/s40825-016-0038-y

9. Chatterjee, D., Burkhardt, T., Rappe, T., Güthenke, A., Weibel, M.: Numerical Simulation of DOC+DPF+SCR systems:DOC Influence on SCR Performance. SAE Int. J. Fuels Lubr. 1, 440–451 (2008). doi:10.4271/2008-01-0867

10. Birkhold, F., Meingast, U., Wassermann, P., Deutschmann, O.: Analysis of the Injection of Urea-Water-Solution for Automotive SCR DeNOx-Systems: Modeling of Two-Phase Flow and Spray/Wall-Interaction. SAE Technical Paper 2006–01–0643 (2006)

11. Brack, W., Heine, B., Birkhold, F., Kruse, M., Schoch, G., Tischer, S., Deutschmann, O.: Kinetic modeling of urea decomposition based on systematic thermogravimetric

analyses of urea and its most important by-products. Chemical Engineering Science. 106, 1–8 (2014). doi:10.1016/j.ces.2013.11.013

12. Ciardelli, C., Nova, I., Tronconi, E., Chatterjee, D., Burkhardt, T., Weibel, M.: SCR of for diesel exhausts aftertreatment: role of in catalytic mechanism, unsteady kinetics and monolith converter modelling. Chemical Engineering Science. 62, 5001–5006 (2007). doi:10.1016/j.ces.2006.11.031

13. Metkar, P.S., Harold, M.P., Balakotaiah, V.: Experimental and kinetic modeling study of NH3-SCR of NOx on Fe-ZSM-5, Cu-chabazite and combined Fe- and Cu-zeolite monolithic catalysts. Chemical Engineering Science. 87, 51–66 (2013). doi:10.1016/j.ces.2012.09.008

14. Metkar, P.S., Balakotaiah, V., Harold, M.P.: Experimental and kinetic modeling study of NO oxidation: Comparison of Fe and Cu-zeolite catalysts. Catalysis Today. 184, 115–128 (2012). doi:10.1016/j.cattod.2011.11.032

15. Metkar, P.S., Harold, M.P., Balakotaiah, V.: Selective catalytic reduction of NOx on combined Fe- and Cu-zeolite monolithic catalysts: Sequential and dual layer configurations. Applied Catalysis B: Environmental. 111–112, 67–80 (2012). doi:10.1016/j.apcatb.2011.09.019

16. Metkar, P.S., Balakotaiah, V., Harold, M.P.: Experimental study of mass transfer limitations in Fe- and Cu-zeolite-based NH3-SCR monolithic catalysts. Chemical Engineering Science. 66, 5192–5203 (2011). doi:10.1016/j.ces.2011.07.014

17. Schuler, A., Votsmeier, M., Kiwic, P., Gieshoff, J., Hautpmann, W., Drochner, A., Vogel, H.: NH3-SCR on Fe zeolite catalysts – From model setup to NH3 dosing. Chemical Engineering Journal. 154, 333–340 (2009). doi:10.1016/j.cej.2009.02.037

18. Sjövall, H., Blint, R.J., Olsson, L.: Detailed kinetic modeling of NH3 SCR over Cu-ZSM-5. Applied Catalysis B: Environmental. 92, 138–153 (2009). doi:10.1016/j.apcatb.2009.07.020

19. Sjövall, H., Blint, R.J., Olsson, L.: Detailed Kinetic Modeling of NH3 and H2O Adsorption, and NH3 Oxidation over Cu-ZSM-5. J. Phys. Chem. C. 113, 1393–1405 (2009). doi:10.1021/jp802449s

20. Tronconi, E., Nova, I., Ciardelli, C., Chatterjee, D., Bandl-Konrad, B., Burkhardt, T.: Modelling of an SCR catalytic converter for diesel exhaust after treatment: Dynamic

effects at low temperature. Catalysis Today. 105, 529–536 (2005). doi:10.1016/j.cattod.2005.06.043

21. Koop, J., Deutschmann, O.: Modeling and Simulation of NOx Abatement with Storage/Reduction Catalysts for Lean Burn and Diesel Engines. Presented at the (2007)

22. Nova, I., Lietti, L., Forzatti, P., Prinetto, F., Ghiotti, G.: Experimental investigation of the reduction of NOx species by CO and H2 over Pt–Ba/Al2O3 lean NOx trap systems. Catalysis Today. 151, 330–337 (2010). doi:10.1016/j.cattod.2010.02.075

23. Olsson, L., Blint, R.J., Fridell, E.: Global Kinetic Model for Lean NOx Traps. Ind. Eng. Chem. Res. 44, 3021–3032 (2005). doi:10.1021/ie0494059

24. Xu, J., Harold, M.P., Balakotaiah, V.: Modeling the effects of Pt loading on NOx storage on Pt/BaO/Al2O3 catalysts. Applied Catalysis B: Environmental. 104, 305–315 (2011). doi:10.1016/j.apcatb.2011.03.014

25. Schejbal, M., Kočí, P., Marek, M., Kubíček, M.: Modelling of wall-flow filters for diesel particulate removal. Computer Aided Chemical Engineering. 26, 803–808 (2009). doi:10.1016/S1570-7946(09)70134-8

26. Koltsakis, G.C., Stamatelos, A.M.: Modeling thermal regeneration of wall-flow diesel particulate traps. AIChE J. 42, 1662–1672 (1996). doi:10.1002/aic.690420618

27. Kandylas, I.P., Koltsakis, G.C.: NO2-Assisted Regeneration of Diesel Particulate Filters: A Modeling Study. Ind. Eng. Chem. Res. 41, 2115–2123 (2002). doi:10.1021/ie010842m

28. Foley, R., Johnson, J., Naber, J., Rogoski, L.: Experimental Measurements of Particulate Matter Distribution in a Catalyzed Particulate Filter. Emission Control Science and Technology. 1, 32–48 (2015). doi:10.1007/s40825-014-0005-4

29. Mahadevan, B.S., Johnson, J.H., Shahbakhti, M.: Development of a Catalyzed Diesel Particulate Filter Multi-zone Model for Simulation of Axial and Radial Substrate Temperature and Particulate Matter Distribution. Emission Control Science and Technology. 1, 183–202 (2015). doi:10.1007/s40825-015-0015-x

30. Koltsakis, G.C., Konstantinidis, P.A., Stamatelos, A.M.: Development and application range of mathematical models for 3-way catalytic converters. Applied Catalysis B: Environmental. 12, 161–191 (1997). doi:10.1016/S0926-3373(96)00073-2

31. Möller, R., Votsmeier, M., Onder, C., Guzzella, L., Gieshoff, J.: Is oxygen storage in three-way catalysts an equilibrium controlled process? Applied Catalysis B: Environmental. 91, 30–38 (2009). doi:10.1016/j.apcatb.2009.05.003

32. Rao, S.K., Imam, R., Ramanathan, K., Pushpavanam, S.: Sensitivity Analysis and Kinetic Parameter Estimation in a Three Way Catalytic Converter. Ind. Eng. Chem. Res. 48, 3779–3790 (2009). doi:10.1021/ie801244w

33. Kiwitz, P., Onder, C., Guzzella, L.: Control-oriented modeling of a three-way catalytic converter with observation of the relative oxygen level profile. Journal of Process Control. 22, 984–994 (2012). doi:10.1016/j.jprocont.2012.04.014

34. Kumar, P., Makki, I., Kerns, J., Grigoriadis, K., Franchek, M., Balakotaiah, V.: A low-dimensional model for describing the oxygen storage capacity and transient behavior of a three-way catalytic converter. Chemical Engineering Science. 73, 373–387 (2012). doi:10.1016/j.ces.2011.12.001

35. Rodríguez-Fernández, J., Lapuerta, M., Sánchez-Valdepeñas, J.: Regeneration of diesel particulate filters: Effect of renewable fuels. Renewable Energy. 104, 30–39 (2017). doi:10.1016/j.renene.2016.11.059

36. Groppi, G., Belloli, A., Tronconi, E., Forzatti, P.: A comparison of lumped and distributed models of monolith catalytic combustors. Chemical Engineering Science. 50, 2705–2715 (1995). doi:10.1016/0009-2509(95)00099-Q

37. Hayes, R.E., Kolaczkowski, S.T.: Mass and heat transfer effects in catalytic monolith reactors. Chemical Engineering Science. 49, 3587–3599 (1994). doi:10.1016/0009-2509(94)00164-2

38. Young, L.C., Finlayson, B.A.: Mathematical models of the monolith catalytic converter: Part I. Development of model and application of orthogonal collocation. AIChE J. 22, 331–343 (1976). doi:10.1002/aic.690220216

39. Young, L.C., Finlayson, B.A.: Mathematical models of the monolith catalytic converter: Part II. Application to automobile exhaust. AIChE J. 22, 343–353 (1976). doi:10.1002/aic.690220217

40. Depcik, C., Srinivasan, A.: One + One-Dimensional Modeling of Monolithic Catalytic Converters. Chem. Eng. Technol. 34, 1949–1965 (2011). doi:10.1002/ceat.201100144

41. Joshi, S.Y., Harold, M.P., Balakotaiah, V.: Low-dimensional models for real time simulations of catalytic monoliths. AIChE J. 55, 1771–1783 (2009). doi:10.1002/aic.11794

42. Kočí, P., Kubíček, M., Marek, M.: Modeling of Three-Way-Catalyst Monolith Converters with Microkinetics and Diffusion in the Washcoat. Ind. Eng. Chem. Res. 43, 4503–4510 (2004). doi:10.1021/ie034137k

43. Depcik, C., Assanis, D.: One-dimensional automotive catalyst modeling. Progress in Energy and Combustion Science. 31, 308–369 (2005). doi:10.1016/j.pecs.2005.08.001

44. Sharma, R.K., Cresswell, D.L., Newson, E.J.: Effective diffusion coefficients and tortuosity factors for commercial catalysts. Ind. Eng. Chem. Res. 30, 1428–1433 (1991). doi:10.1021/ie00055a004

45. Perry, T.H.E., Green, D.W.: Perry's chemical engineers' handbook. 7th edition,1997.

46. Stotz, H., Maier, L., Deutschmann, O.: Methane Oxidation over Palladium: On the Mechanism in Fuel-Rich Mixtures at High Temperatures. Top Catal. 1–27 (2016). doi:10.1007/s11244-016-0717-5

47. Holder R..A.M.: A Global Reaction Mechanism for Transient Simulations of Three-Way Catalytic Converters, (2008)

48. Depcik, C.D., Hausmann, A.J.: Review and a Methodology to Investigate the Effects of Monolithic Channel Geometry. J. Eng. Gas Turbines Power. 135, 032301-032301-16 (2013). doi:10.1115/1.4007848

49. Magnusson, F., Åkesson, J.: Collocation Methods for Optimization in a Modelica Environment. Presented at the Proceedings of the 9th International MODELICA Conference; September 3-5; 2012; Munich; Germany November 19 (2012)

50. Cesari, L.: Optimization Theory and Applications, Springer, New York (1983)

51. Benson, H.Y., Vanderbei, R.J., Shanno, D.F.: Interior-Point Methods for Nonconvex Nonlinear Programming: Filter Methods and Merit Functions. Computational Optimization and Applications. 23, 257–272 (2002). doi:10.1023/A:1020533003783

52. Byrd, R.H., Nocedal, J., Waltz, R.A.: Knitro: An Integrated Package for Nonlinear Optimization. In: Di Pillo, G. and Roma, M. (eds.) Large-Scale Nonlinear Optimization. pp. 35–59. Springer US, Boston, MA (2006)

53. Wächter, A., Biegler, L.T.: On the implementation of an interior-point filter line-search algorithm for large-scale nonlinear programming. Math. Program. 106, 25–57 (2006). doi:10.1007/s10107-004-0559-y

54. Minh, H.D., Bock, H.G., Tischer, S., Deutschmann, O.: Optimization of two-dimensional flows with homogeneous and heterogeneously catalyzed gas-phase reactions. AIChE J. 54, 2432–2440 (2008). doi:10.1002/aic.11563

55. Bock, H.G., Karl-Josef, P.: A multiple shooting algorithm for direct solution of optimal control problems. IFAC Proceedings Volumes.17, (2), 1603–1608 (1984). doi:10.1016/S1474-6670(17)61205-9

56. Leineweber, D.B., Bauer, I., Bock, H.G., Schlöder, J.P.: An efficient multiple shooting based reduced SQP strategy for large-scale dynamic process optimization. Part 1: theoretical aspects. Computers & Chemical Engineering. 27, 157–166 (2003). doi:10.1016/S0098-1354(02)00158-8

57. Leineweber, D.B., Schäfer, A., Bock, H.G., Schlöder, J.P.: An efficient multiple shooting based reduced SQP strategy for large-scale dynamic process optimization: Part II: Software aspects and applications. Computers & Chemical Engineering. 27, 167–174 (2003). doi:10.1016/S0098-1354(02)00195-3

58. Kameswaran, S., Biegler, L.T.: Simultaneous dynamic optimization strategies: Recent advances and challenges. Computers & Chemical Engineering. 30, 1560–1575 (2006). doi:10.1016/j.compchemeng.2006.05.034

59. Biegler, L.T.: An overview of simultaneous strategies for dynamic optimization. Chemical Engineering and Processing: Process Intensification. 46, 1043–1053 (2007). doi:10.1016/j.cep.2006.06.021

60. Biegler, L.T.: Nonlinear Programming: Concepts, Algorithms, and Applications to Chemical Processes. SIAM-Society for Industrial and Applied Mathematics, Philadelphia, Pa. (2010)

61. Rao, A.V.: A Survey of Numerical Methods for Optimal Control. Advances in the Astronautical Sciences 135 (1), 497-528.

62. Cao, Y., Li, S., Petzold, L.: Adjoint sensitivity analysis for differential-algebraic equations: algorithms and software. Journal of Computational and Applied Mathematics. 149, 171–191 (2002). doi:10.1016/S0377-0427(02)00528-9

63. Gill P.E., Murray W., Wright M.H.: Practical Optimization. Academic Press, London. (1981)

64. Li, S., Petzold, L.: Software and algorithms for sensitivity analysis of large-scale differential algebraic systems. Journal of Computational and Applied Mathematics. 125, 131–145 (2000). doi:10.1016/S0377-0427(00)00464-7

65. Griewank, A., Walther, A.: Introduction to Automatic Differentiation. Proc. Appl. Math. Mech. 2, 45–49 (2003). doi:10.1002/pamm.200310012

66. Kim, Y.-D., Jeong, S.-J., Kim, W.-S.: Optimal design of axial noble metal distribution for improving dual monolithic catalytic converter performance. Chemical Engineering Science. 64, 1373–1383 (2009). doi:10.1016/j.ces.2008.11.020

67. Kirchner, T., Eigenberger, G.: Optimization of the cold-start behaviour of automotive catalysts using an electrically heated pre-catalyst. Chemical Engineering Science. 51, 2409–2418 (1996). doi:10.1016/0009-2509(96)00097-8

68. Tronci, S., Baratti, R., Gavrillidis, A.: Catalytic Converter Design for Minimisation of Cold-Start Emissions. Chemical Engineering Communications. 173, 53–77 (1999). doi:10.1080/00986449908912776

69. Oh, S.H., Bissett, E.J., Battiston, P.A.: Mathematical modeling of electrically heated monolith converters: model formulation, numerical methods, and experimental verification. Ind. Eng. Chem. Res. 32, 1560–1567 (1993). doi:10.1021/ie00020a005

70. Oh, S.H., Bissett, E.J.: Mathematical Modeling of Electrically Heated Monolith Converters: Analysis of Design Aspects and Heating Strategy. Ind. Eng. Chem. Res. 33, 3086–3093 (1994). doi:10.1021/ie00036a025

71. Bissett, E.J., Oh, S.H.: Electrically heated converters for automotive emission control: determination of the best size regime for the heated element. Chemical Engineering Science. 54, 3957–3966 (1999). doi:10.1016/S0009-2509(99)00110-4

72. Ramanathan, K., Oh, S.H., Bissett, E.J.: Electrically Heated Catalysts for Hybrid Applications: Mathematical Modeling and Analysis. Ind. Eng. Chem. Res. 50, 8444–8467 (2011). doi:10.1021/ie200044w

73. Litto, R., Mmbaga, J.P., Hayes, R.E., Plati, S., Blagojevic, V., Subject, P.: Exhaust emissions and fuel economy improvements through thermal performance control in a

novel three-way catalytic converter. Can. J. Chem. Eng. 94, 905–912 (2016). doi:10.1002/cjce.22449

74. Al-Adwani, S.M., Soares, J., Epling, W.S.: Evaluating the Effects of Precious Metal Distribution along a Monolith-Supported Catalyst for CO oxidation. Ind. Eng. Chem. Res. 51, 6672–6679 (2012). doi:10.1021/ie202969u

75. Khanaev, V.M., Borisova, E.S., Noskov, A.S.: Optimization of the active component distribution through the catalyst bed for the case of adiabatic reactor. Chemical Engineering Science. 60, 5792–5802 (2005). doi:10.1016/j.ces.2005.05.034

76. Khanaev, V.M., Borisova, E.S., Galkina, L.I., Noskov, A.S.: Improvement of the catalytic monoliths efficiency for CO oxidation using non-uniform active component distribution along the monolith length. Chemical Engineering Journal. 102, 35–44 (2004). doi:10.1016/j.cej.2004.02.003

77. Khanaev, V.M., Borisova, E.S., Noskov, A.S.: Optimization of the active component distribution through the catalyst bed. Chemical Engineering Science. 59, 1213–1220 (2004). doi:10.1016/j.ces.2003.12.005

78. Kim, Y.D., Kim, W.S.: Optimum Design of an Automotive Catalytic Converter for minimization of Cold start emissions using micro genetic algorithm. Int J Automot Technol. 8, 563–573 (2007)

79. Psyllos, A., Philippopoulos, C.: Performance of a monolithic catalytic converter used in automotive emission control: the effect of a longitudinal parabolic active metal distribution. Ind. Eng. Chem. Res. 32, 1555–1559 (1993). doi:10.1021/ie00020a004

80. Oh, S.H., Cavendish, J.C.: Transients of monolithic catalytic converters. Response to step changes in feedstream temperature as related to controlling automobile emissions. Ind. Eng. Chem. Prod. Res. Dev. 21, 29–37 (1982). doi:10.1021/i300005a006

81. Kim, Y.D., Kim, W.S.: Optimum design of an automotive catalytic converter for minimization of cold-start emissions using a micro genetic algorithm. International Journal of Automotive Technology, International Journal of Automotive Technology. 8, 563–573

82. Abedi, A., Luo, J.-Y., Epling, W.S.: Improved CO, hydrocarbon and NO oxidation performance using zone-coated Pt-based catalysts. Catalysis Today. 207, 220–226 (2013). doi:10.1016/j.cattod.2012.04.012

83. Siemund, S., Schweich, D., Leclerc, J.P., Villermaux, J.: Modelling three-way monolithic catalytic converter: Comparison between simulation and experimental data. In: Bastin, A.F. and J.-M. (ed.) Studies in Surface Science and Catalysis. pp. 887–895. Elsevier (1995)

84. Depcik, C., Assanis, D.: One-dimensional automotive catalyst modeling. Progress in Energy and Combustion Science. 31, 308–369 (2005). doi:10.1016/j.pecs.2005.08.001

85. Holder, R., Bollig, M., Anderson, D.R., Hochmuth, J.K.: A discussion on transport phenomena and three-way kinetics of monolithic converters. Chemical Engineering Science. 61, 8010–8027 (2006). doi:10.1016/j.ces.2006.09.030

86. Santos, H., Costa, M.: Modelling transport phenomena and chemical reactions in automotive three-way catalytic converters. Chemical Engineering Journal. 148, 173–183 (2009). doi:10.1016/j.cej.2008.11.047

87. Canu, P., Vecchi, S.: CFD simulation of reactive flows: Catalytic combustion in a monolith. AIChE J. 48, 2921–2935 (2002). doi:10.1002/aic.690481219

88. Tsinoglou, D.N., Koltsakis, G.C.: Effect of perturbations in the exhaust gas composition on three-way catalyst light off. Chemical Engineering Science. 58, 179–192 (2003). doi:10.1016/S0009-2509(02)00472-4

89. Mladenov, N., Koop, J., Tischer, S., Deutschmann, O.: Modeling of transport and chemistry in channel flows of automotive catalytic converters. Chemical Engineering Science. 65, 812–826 (2010). doi:10.1016/j.ces.2009.09.034

90. Scheuer, A., Hauptmann, W., Drochner, A., Gieshoff, J., Vogel, H., Votsmeier, M.: Dual layer automotive ammonia oxidation catalysts: Experiments and computer simulation. Applied Catalysis B: Environmental. 111–112, 445–455 (2012). doi:10.1016/j.apcatb.2011.10.032

91. von Schwerin, M., Deutschmann, O., Schulz, V.: Process optimization of reactives systems by partially reduced SQP methods. Computers & Chemical Engineering. 24, 89–97 (2000). doi:10.1016/S0098-1354(00)00305-7

92. Raja, L.L., Kee, R.J., Serban, R., Petzold, L.R.: Computational Algorithm for Dynamic Optimization of Chemical Vapor Deposition Processes in Stagnation Flow Reactors. J. Electrochem. Soc. 147, 2718–2726 (2000). doi:10.1149/1.1393595

93. Hascoet, L., Pascual, V.: The Tapenade Automatic Differentiation Tool: Principles, Model, and Specification. ACM Trans. Math. Softw. 39, 20:1–20:43 (2013). doi:10.1145/2450153.2450158

94. Chan, D., Tischer, S., Heck, J., Diehm, C., Deutschmann, O.: Correlation between catalytic activity and catalytic surface area of a Pt/Al2O3 DOC: An experimental and microkinetic modeling study. Applied Catalysis B: Environmental. 156–157, 153–165 (2014). doi:10.1016/j.apcatb.2014.03.009

95. Leung, D., Hayes, R.E., Kolaczkowski, S.T.: Diffusion limitation effects in the washcoat of a catalytic monolith reactor. Can. J. Chem. Eng. 74, 94–103 (1996). doi:10.1002/cjce.5450740112

96. Voltz, S.E., Morgan, C.R., Liederman, D., Jacob, S.M.: Kinetic Study of Carbon Monoxide and Propylene Oxidation on Platinum Catalysts. Product R&D. 12, 294–301 (1973). doi:10.1021/i360048a006

97. Ramanathan, K., West, D.H., Balakotaiah, V.: Optimal design of catalytic converters for minimizing cold-start emissions. Catalysis Today. 98, 357–373 (2004). doi:10.1016/j.cattod.2004.08.003

98. McClure, S.M., Goodman, D.W.: New insights into catalytic CO oxidation on Pt-group metals at elevated pressures. Chemical Physics Letters. 469, 1–13 (2009). doi:10.1016/j.cplett.2008.12.066

99. Gremminger, A.T., Pereira de Carvalho, H.W., Popescu, R., Grunwaldt, J.-D., Deutschmann, O.: Influence of gas composition on activity and durability of bimetallic Pd-Pt/Al2O3 catalysts for total oxidation of methane. Catalysis Today. 258, Part 2, 470–480 (2015). doi:10.1016/j.cattod.2015.01.034

100. Burch, R., Urbano, F.J., Loader, P.K.: Methane combustion over palladium catalysts: The effect of carbon dioxide and water on activity. Applied Catalysis A: General. 123, 173–184 (1995). doi:10.1016/0926-860X(94)00251-7

101. Hayes, R.E., Kolaczkowski, S.T., Li, P.K.C., Awdry, S.: The palladium catalysed oxidation of methane: reaction kinetics and the effect of diffusion barriers. Chemical Engineering Science. 56, 4815–4835 (2001). doi:10.1016/S0009-2509(01)00131-2

102. Koebel, M., Elsener, M., Kleemann, M.: Urea-SCR: a promising technique to reduce NOx emissions from automotive diesel engines. Catalysis Today. 59, 335–345 (2000). doi:10.1016/S0920-5861(00)00299-6

103. Birkhold, F., Meingast, U., Wassermann, P., Deutschmann, O.: Modeling and simulation of the injection of urea-water-solution for automotive SCR DeNOx-systems. Applied Catalysis B: Environmental. 70, 119–127 (2007). doi:10.1016/j.apcatb.2005.12.035

104. Song, X., Parker, G., Johnson, J.H., Naber, J., Pihl, J.: A Modeling Study of SCR Reaction Kinetics from Reactor Experiments. SAE Technical Paper 2013–01–1576 (2013)

105. Chatterjee, D., Burkhardt, T., Weibel, M., Nova, I., Grossale, A., Tronconi, E.: Numerical Simulation of Zeolite- and V-Based SCR Catalytic Converters. SAE Technical Paper 2007–01–1136 (2007)

106. Olsson, L., Sjövall, H., Blint, R.J.: A kinetic model for ammonia selective catalytic reduction over Cu-ZSM-5. Applied Catalysis B: Environmental. 81, 203–217 (2008). doi:10.1016/j.apcatb.2007.12.011

107. Ciardelli, C., Nova, I., Tronconi, E., Chatterjee, D., Burkhardt, T., Weibel, M.: NH3 SCR of NOx for diesel exhausts aftertreatment: role of in catalytic mechanism, unsteady kinetics and monolith converter modelling. Chemical Engineering Science. 62, 5001–5006 (2007). doi:10.1016/j.ces.2006.11.031

108. Colombo, M., Nova, I., Tronconi, E.: Detailed kinetic modeling of the NH3–NO/NO2 SCR reactions over a commercial Cu-zeolite catalyst for Diesel exhausts after treatment. Catalysis Today. 197, 243–255 (2012). doi:10.1016/j.cattod.2012.09.002

109. Opitz, B., Bendrich, M., Drochner, A., Vogel, H., Hayes, R.E., Forbes, J.F., Votsmeier, M.: Simulation study of SCR catalysts with individually adjusted ammonia dosing strategies. Chemical Engineering Journal. 264, 936–944 (2015). doi:10.1016/j.cej.2014.11.114

110. Faghihi, E.M., Shamekhi, A.H.: Development of a neural network model for selective catalytic reduction (SCR) catalytic converter and ammonia dosing optimization using multi objective genetic algorithm. Chemical Engineering Journal. 165, 508–516 (2010). doi:10.1016/j.cej.2010.09.055

111. Hauptmann, W., Schuler, A., Gieshoff, J., Votsmeier, M.: Modellbasierte Optimierung der Harnstoffdosierung für SCR-Katalysatoren. Chemie Ingenieur Technik. 83, 1681–1687 (2011). doi:10.1002/cite.201100125

112. Balakotaiah, V.: On the relationship between Aris and Sherwood numbers and friction and effectiveness factors. Chemical Engineering Science. 63, 5802–5812 (2008). doi:10.1016/j.ces.2008.08.025

113. Joshi, S.Y., Harold, M.P., Balakotaiah, V.: On the use of internal mass transfer coefficients in modeling of diffusion and reaction in catalytic monoliths. Chemical Engineering Science. 64, 4976–4991 (2009). doi:10.1016/j.ces.2009.08.008

114. Bissett, E.J.: An Asymptotic Solution for Washcoat Pore Diffusion in Catalytic Monoliths. Emiss. Control Sci. Technol. 1, 3–16 (2015). doi:10.1007/s40825-015-0010-2

115. Gundlapally, S.R., Papadimitriou, I., Wahiduzzaman, S., Gu, T.: Development of ECU Capable Grey-Box Models from Detailed Models—Application to a SCR Reactor. Emission Control Science and Technology. 2, 124–136 (2016). doi:10.1007/s40825-016-0039-x

116. Li, S., Petzold, L.: Design of New Daspk for Sensitivity Analysis. University of California at Santa Barbara, Santa Barbara, CA, USA (1999)

117. Betts, J.T.: Survey of Numerical Methods for Trajectory Optimization. Journal of Guidance, Control, and Dynamics. 21, 193–207 (1998). doi:10.2514/2.4231

118. Andersson, J., Åkesson, J., Diehl, M.: CasADi: A Symbolic Package for Automatic Differentiation and Optimal Control. In: Recent Advances in Algorithmic Differentiation. pp. 297–307. Springer, Berlin, Heidelberg (2012)

119. Roman Jörg Möller: Modeling and Control of Three-way catalysts, ETH Zurich. (2009)

120. Auckenthaler T. S.: Modelling and Control of Three-Way Catalytic Converters, Diss. ETH No. 16018, (2005)

121. Soumelidis, M.I., Stobart, R.K., Jackson, R.A.: A Nonlinear Dynamic Model for Three-Way Catalyst Control and Diagnosis. SAE 2004 Transactions, Vol. 4, Fuels and Lubricants, 2004, SAE paper 2004-01-1831, pp. 764–775 (Society of Automotive Engineers, New York).

122. Bickel, J., Odendall, B., Eigenberger, G., Nieken, U.: Oxygen storage dominated three-way catalyst modeling for fresh catalysts. Chemical Engineering Science. 160, 34–53 (2017). doi:10.1016/j.ces.2016.11.016

123. Rink, J., Meister, N., Herbst, F., Votsmeier, M.: Oxygen storage in three-way-catalysts is an equilibrium controlled process: Experimental investigation of the redox thermodynamics. Applied Catalysis B: Environmental. 206, 104–114 (2017). doi:10.1016/j.apcatb.2016.12.052

124. Salehi, R., Alasti, A., Vossoughi, G., Boroushaki, M.: Nonlinear Oxygen Sensor Output Voltage Estimation in a Gasoline Engine Using NARX Model. JER. 22, 13–20 (2011)

List of Publications

Publications:

Kannepalli, S., Gremminger, A., Tischer,S., Deutschmann, O. : Optimization of axial catalyst loading in transient-operated zone-structured monoliths: Reduction of cumulative emissions in automotive oxidation catalysts, Chemical Engineering Science (2017)

Kannepalli, S., Bürger, A., Tischer,S., Deutschmann, O. : Model-Based Optimization of Ammonia Dosing in NH_3-SCR of NO_x for Transient Driving Cycle: Model Development and Simulation, Emission Control Science and Technology (2017)

Poster presentations:

Kannepalli, S., Bürger, A., Tischer,S., Deutschmann, O. : Development of Simulation Tools for Zone-structured catalysts, MODEGAT III, Bad Herrenalb, 8-10 september 2013

Kannepalli, S., Bürger, A., Tischer,S., Deutschmann, O. : Model-Based Optimization of Ammonia Dosing in NH3-SCR of NOx for Transient Driving Cycle: Model Development and Simulation, MODEGAT V, Bad Herrenalb, 3-5 september 2017